Air Ingress in HTGRs:

The process, effects, and experimental methods relating to its investigation and consequences

by

Daniel W. Gould

B.S., University of Colorado - Colorado Springs, 2012

M.S., University of Colorado - Colorado Springs, 2013

AN ABSTRACT OF A DISSERTATION

submitted in partial fulfillment of the
requirements for the degree

DOCTOR OF PHILOSOPHY

Department of Mechanical and Nuclear Engineering
College of Engineering

KANSAS STATE UNIVERSITY
Manhattan, Kansas

2018

Abstract

Helium-cooled, graphite moderated reactors have been considered for a future fleet of high temperature and high efficiency nuclear power plants. Nuclear-grade graphite is used in these reactors for structural strength, neutron moderation, heat transfer and, within a helium environment, has demonstrated stability at temperatures well above HTGR operating conditions. However, in the case of an air ingress accident, the oxygen introduced into the core can affect the integrity of the fuel graphite matrix. In this work a combination of computational models and mixed effects experiments were used to better understand the air ingress process and its potential effects on the heat removal capabilities of an HTGR design following an air-ingress accident. Contributions were made in the understanding of the air-ingress phenomenon, its potential effects on graphite, and in experimental and computational techniques.

The first section of this thesis focuses on experimental and computational studies that were undertaken to further the understanding of the Onset of Natural Convection (ONC) phenomenon expected to occur inside of an HTGR following an air ingress accident. The effects of two newly identified factors on ONC – i.e., the existence of the large volume of stagnate helium in a reactor's upper plenum, and the possibility of an upper head leak – were investigated.

Mixed-effects experimental studies were performed to determine the changes induced in nuclear grade graphite exposed to high-temperature, oxidizing flow of varying flow rates. Under all scenarios, the thermal diffusivity of the graphite test samples was shown to increase. Thermal conductivity changes due to oxidation were found to be minor in the tested graphite samples – especially compared to the large drop in thermal conductivity the graphite is expected to experience due to irradiation. Oxidation was also found to increase the graphite's surface roughness and create a thin outer layer of decreased density.

The effects of thermal contacts on the passive cooling ability of an HTGR were experimentally investigated. Conduction cool down experiments were performed on assemblies consisting of a number of rods packed into a cylindrical tube. Experimental conditions were then modeled using several different methodologies, including a novel graph laplacian approach, and their results compared to the experimentally obtained temperature data. Al-

though the graph laplacian technique shows great promise, the 2–D Finite Element Model (FEM) provided the best results

Finally, a case study was constructed in which a section of a pebble bed reactor consisting of a number of randomly packed, spherical fuel particles was modeled using the validated FEM technique. Using a discrete elements model, a stable, randomly packed geometry was created to represent the pebble bed. A conduction cool down scenario was modeled and the results from the FEM model were compared to best possible results obtainable from a more traditional, homogeneous 1–D approximation. When the graphite in the bed was modeled as both oxided and irradiated, the homogeneous method mispredicted the maximum temperature given by the 3–D, FEM model by more than 100 °C.

Air Ingress in HTGRs:

The process, effects, and experimental methods relating to its investigation and consequences

by

Daniel W. Gould

B.S., University of Colorado - Colorado Springs, 2012

M.S., University of Colorado - Colorado Springs, 2013

A DISSERTATION

submitted in partial fulfillment of the
requirements for the degree

DOCTOR OF PHILOSOPHY

Department of Mechanical and Nuclear Engineering
College of Engineering

KANSAS STATE UNIVERSITY
Manhattan, Kansas

2018

Approved by:

Major Professor
Dr. Hitesh Bindra

Copyright

Abstract

Helium-cooled, graphite moderated reactors have been considered for a future fleet of high temperature and high efficiency nuclear power plants. Nuclear-grade graphite is used in these reactors for structural strength, neutron moderation, heat transfer and, within a helium environment, has demonstrated stability at temperatures well above HTGR operating conditions. However, in the case of an air ingress accident, the oxygen introduced into the core can affect the integrity of the fuel graphite matrix. In this work a combination of computational models and mixed effects experiments were used to better understand the air ingress process and its potential effects on the heat removal capabilities of an HTGR design following an air-ingress accident. Contributions were made in the understanding of the air-ingress phenomenon, its potential effects on graphite, and in experimental and computational techniques.

The first section of this thesis focuses on experimental and computational studies that were undertaken to further the understanding of the Onset of Natural Convection (ONC) phenomenon expected to occur inside of an HTGR following an air ingress accident. The effects of two newly identified factors on ONC – i.e., the existence of the large volume of stagnate helium in a reactor's upper plenum, and the possibility of an upper head leak – were investigated.

Mixed-effects experimental studies were performed to determine the changes induced in nuclear grade graphite exposed to high-temperature, oxidizing flow of varying flow rates. Under all scenarios, the thermal diffusivity of the graphite test samples was shown to increase. Thermal conductivity changes due to oxidation were found to be minor in the tested graphite samples – especially compared to the large drop in thermal conductivity the graphite is expected to experience due to irradiation. Oxidation was also found to increase the graphite's surface roughness and create a thin outer layer of decreased density.

The effects of thermal contacts on the passive cooling ability of an HTGR were experimentally investigated. Conduction cool down experiments were performed on assemblies consisting of a number of rods packed into a cylindrical tube. Experimental conditions were then modeled using several different methodologies, including a novel graph laplacian approach, and their results compared to the experimentally obtained temperature data. Al-

though the graph laplacian technique shows great promise, the 2–D Finite Element Model (FEM) provided the best results

Finally, a case study was constructed in which a section of a pebble bed reactor consisting of a number of randomly packed, spherical fuel particles was modeled using the validated FEM technique. Using a discrete elements model, a stable, randomly packed geometry was created to represent the pebble bed. A conduction cool down scenario was modeled and the results from the FEM model were compared to best possible results obtainable from a more traditional, homogeneous 1–D approximation. When the graphite in the bed was modeled as both oxided and irradiated, the homogeneous method mispredicted the maximum temperature given by the 3–D, FEM model by more than 100 °C.

Contents

List of Figures

List of Tables

Acknowledgments

The author would like to acknowledge the NRC for funding this work.

First and foremost, the author would like to thank Dr. Hitesh Bindra. Throughout my time working under him – and in addition to showing extra-human levels of patience – Dr. Bindra provided me with wise counsel and much needed direction. This work would not, and could not, have been completed without his assistance and guidance.

The assistance of Dr. Sanjoy Das was instrumental in the creation of the graph-theory based point contact heat transfer model.

The author is also especially gratefull for all the work done by Ardalan Chaichi and Dr. Manas Gartia at Louisiana State University performing tests on the oxidized graphite samples.

Several other individuals were of great help in completing this work and deserve mentioning:

Mark Shattuck for providing the initial code upon which my DEM code was built.

Daniel Franken for his work performing the computational studies.

Richard Reed, Abhinav Gairola, Brennan Ward, and Daniel Franken for their motivational assistance and willingness endure the author's bouts of frustration and general orneriness.

Lazăr Edeleanu for his invaluable invention.

Molly Ross for both obtaining GTMHR geometric information and providing regular reminders of the many advantages of heat engines in naval propulsion.

The author would also like to thank the many undergraduate students – and especially those who provided assistance in the months during which the author possessed only one functioning arm – who helped out in the lab. Additionally, their constant and stubborn

unwillingness to put tools back in their proper places provided additional motivation to finish this work.

Finally, the author would like to thank Dr. Placidus Amama, Dr. Terry Beck, Dr. Bill Dunn, Dr. William Hsu, and Dr. Ajay Sharda for agreeing to be on my committee and all of the time and effort that required.

Dedication

This work is dedicated to the 4 people who have provided the greatest amount advice, assistance, and support throughout my academic career:

My parents, Bob and Linda Gould;
and my advisers, Dr. Rebecca Webb and Dr. Hitesh Bindra.

It is because of these individuals that I am receiving a PhD rather than a GED.

And to my sister, who's kindness and support has never wavered.

Nomenclature

A_t	transfer area	t	Time
b	Hyperplane bias	t	time
I	Inner rods	V	volume
D	diffusion coefficient	v	velocity
d	diameter	$\mathbf{w}$	Directional vector
f	darcy friction factor	$\bar{X}$	system average helium molar fraction
g	gravitational acceleration	X	mole fraction
h	head loss	$_b$	bottom of system
H_{tot}	Total Enthalpy	$_D$	diffusion
i, j	Node or rod indices	$_h$	hole
j	molar concentration flux	$_i$	region number
$\mathbf{K}$	Diffusion kernel matrix	$_L$	lower region
k	Thermal Conductivity	$_U$	upper region
K	head loss coefficient	z	verticle position
$\mathbf{L}$	Laplacian matrix	ϵ	Insensitive loss function
$ł_0$	Weight of the ghost node	λ	Lagrange multiplier
L	length	ρ	Density
NC	Natural Convection	σ	Spatial constant
O	Outer rods	τ	Temporal constant
R	specific gas constant	τ	time scale
SLM	Standard Liters per Minute	θ	Temperature (Non-Dimensional)
T_0	Initialization time	θ_0	θ for ghost node

Chapter 1

Introduction

1.1 Background

Helium-cooled, graphite moderated reactors have been considered for a future fleet of high temperature and efficiency nuclear power plants. In addition to it's very high thermal conductivity, a prime advantage of helium is its inability to sustain any chemical or nuclear interactions. The choice of helium as coolant aids in the passively safe design of these high-temperature gas-cooled reactors (HTGRs). HTGRs are designed for their graphite moderator to operate at higher temperatures above 900 °C Therefore, were an air ingress into an HTGR occur, the exposure of high temperature graphite to oxygen could lead to undesirable consequences triggered by the graphite oxidation.

Although the next generation of nuclear power plants, including HTGRs, have passive safety design features for use during off-normal operation, it is unproven whether their safety systems will perform as advertised. The unproven nature of these passive systems is especially worrisome if an air ingress were to occur. The graphite-fuel matrix in HTGRs can come in direct contact with air at high temperature if an air ingress were to result from a sever accident – negatively affecting their passive heat removal capabilities. Even nuclear grade graphite has been shown to undergo oxidation when subjected to an air ingress at high temperatures, potentially resulting in density changes near the surface. The oxidation process is thought to have a substantially negative impact on the thermal properties of graphite such as thermal conductivity, density, and emissivity, which in turn can eventually lead to higher core temperatures.

The optimal approach to gain understanding in this matter is to computationally model relevant phenomena using either system level or detailed 3D multiphysics codes, and then conduct HTGR related separate effects experiments using scaled models. These models can provide validation data and complement computational efforts to identify critical issues related to passive safety design. Several Phenomena Identification and Ranking Tables (PIRT) for HTGRs show that under normal steady-state, transient, and accident scenarios, the key phenomena leading to localized hot spots in the reactor core include air ingress, water-steam ingress, natural convection, degraded heat transfer in coolant channels, flow laminarization,

effects of bypass flow, and non-uniform heat generation across the core [1–4]. Some of these phenomena have been understood in-depth in recent years but air-ingress is one of the less understood topics till now.

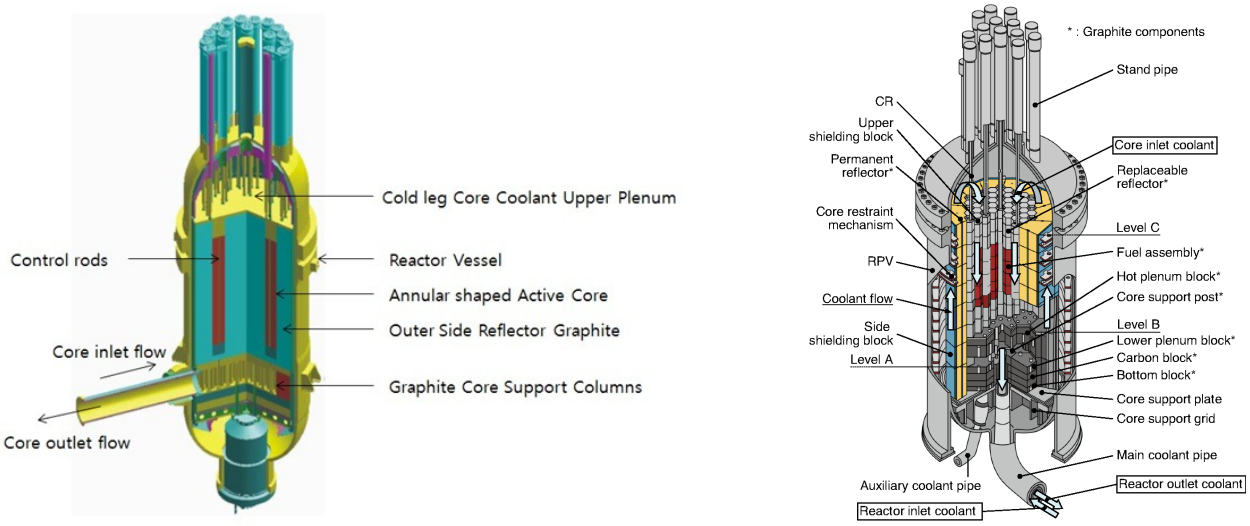

(a) *GT-MHR* **(b)** *HTTR*

Figure 1.1: *Two gas-cooled graphite moderated reactor designs: GT-MHR and HTTR*

A common feature of HTGRs with a passive safety design is that under certain accident conditions the decay heat is dissipated passively from the core by radiation–conduction–convection heat transport to the surrounding environment. Conduction and radiation heat transfer are expected to provide long-term heat removal. However, during a Depressurized Loss of Forced Coolant (DLOFC) accident, a break in the coolant system will allow air ingress into the high temperature reactor and can lead to graphite oxidation, which will negatively impact the core thermal behavior. Air ingress in the HTGR plena and core regions is a complex process and highly dependent upon the specific geometry of both the reactor and the break. While there have been several analytical or computational studies to estimate air ingress rates in HTGRs, most previous studies have been based on hypothetical scenarios of break-size and orientation.

The High Temperature Test Facility (HTTF)[5] at Oregon Sate University is a 1/3 scale model of Gas turbine Modular Helium Reactor (GT-MHR) – the American HTGR design – and will be used in the future to perform air-ingress experimental studies [6]. Additionally,

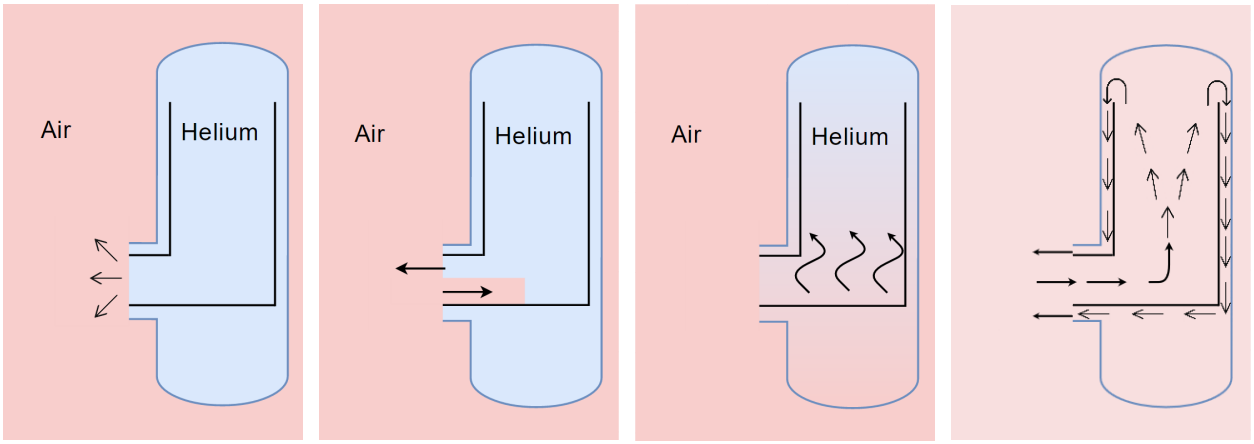

(a) *Depressurization* **(b)** *Stratified Flow* **(c)** *Diffusion* **(d)** *Natural Convection*

Figure 1.2: *Air ingress scenario with helium-air stratification and diffusion [9]*

a 1/8th scaled model for lower plenum has been designed at Ohio State University to study air ingress experiments[7, 8]. Experimental data, however, is not yet available from either of these two facilities.

One of the goals of the proposed experiments in each of these facilities is to investigate mechanisms for air ingress from the containment or reactor cavity into the lower plenum and core after a double-guillotine break of the main inlet-outlet co-axial header of GT-MHRs. There are three different possible modes of air-ingress: molecular diffusion due to a concentration gradient of helium-air, convective transport of air, and natural convection due to a thermally driven upward draft in the core. If the dominating mechanism is molecular diffusion, the rate of air-ingress is quite slow, whereas if the driving mode is convective transport, air circulation can start within few minutes. The analytical or computational studies performed on these hypothetical accidents in GT-MHRs suggest that due to gravity currents (lock-exchange) the convective air-ingress mode is reached instantaneously [10, 11]. This air flow into the lower plenum and core with high temperature graphite can lead to adverse consequences such as oxidation of graphite and can negatively impact the passive heat removal capabilities of the reactor. Therefore, it is highly desired to know accurately when this natural convection would begin. It has been suggested by Oh and others[9, 12, 13] that the sequence of events during an air ingress accident involve : (1) depressurization, (2) density-driven stratified flow, (3) diffusion into the reactor core, and (4) global natural circu-

lation (Fig. 1.2). The potential formation and effect of stratified flow is highly dependent on a given reactor design. The nature of this stratified flow after depressurization determines the initiation time and rate of air ingress into the reactor vessel. At some point after the development of the stratification regime and the filling of the lower plenum with air global natural circulation will begin. However, there are conflicting reports in the literature on the onset of natural convection time.

According to simulation results obtained by Oh et al.Oh and Kim [10] using a CFD code, FLUENT, showed that the onset of natural convection time is expected within 100 secs of depressurization. However, simulations performed using the previously validated, 2D Gamma code[14, 15] reveal that the onset of natural circulation within an HTGR is anticipated to occur several hours – rather than several seconds – after the depressurization event. Unfortunately, there is currently a very limited amount of experimental data in the established literature that can be used to understand this transition from diffusion to natural circulation and validate numerical models. In a separate-effects experimental study on isothermal air ingress through horizontal ports in a helium filled scaled-vessel[16], it was found that it would take several minutes to fill the entire test chamber with air – a result that differs from the numerical predictions by Oh et al. [10, 11].

The predictive modeling of this process is quite challenging because the CFD codes don't have appropriate models for properties such as molecular diffusion in binary mixtures. The thermophysical properties such as thermal conductivity, viscosity and specific heat capacity of helium-air mixtures strongly vary with the air concentration or with the presence of any heavier gas [17, 18], and are difficult to model. At intermediate concentrations, the Prandtl number of these binary mixtures reduces to values well below those of common gasses. This reduction increases the uncertainty in the applicability of the conventional heat transfer correlations and turbulence models. The uncertainty would be even greater at low Reynolds numbers and for natural convection flows. Therefore, despite the large volume of work that has been done on this subject, the computational models may require further improvements before they can be reliably used for design basis studies.

The remainder of this work is divided up into 5 chapters. Chapter 2 focuses on experi-

mental and computational studies that were undertaken to further the understanding of the Onset of Natural Convection phenomenon expected to occur inside of an HTGR following an air ingress accident. The effects of each of two newly identified factors on ONC – i.e., the existence of the large volume of stagnate helium in a reactor's upper plenum and the possibility of an upper head leak – were quantified in terms of previous research and reactor designs. In Chapter 3, mixed-effects experimental studies were performed to determine the changes induced in nuclear grade graphite exposed to high-temperature, oxidizing flow of varying flow rates. Continuous, in-situ measurements of the environmental conditions surrounding the tested annular graphite cylinders were combined with post experiment analysis of samples taken from the oxidized test pieces to obtain information on the changes in thermal diffusivity, thermal conductivity, density, and surface roughness. The effects of line thermal contacts on the passive cooling ability of an HTGR were experimentally investigated in Chapter 4 in which conduction cool down experiments were performed on assemblies consisting of a number of rods packed into a cylindrical tube. Experimental conditions were then modeled using several different methodologies – including a novel Support Vector Regression approach – and their results compared to the experimentally obtained temperature data. The results of the 3 previous chapters were then used to create a 3–D, FEM model of a number of spherical fuel particles contained within a cylinder. This effort is detailed in Chapter 5. A conduction cool down scenario was modeled and the results from the FEM model were compared to best possible results obtainable from a more traditional, homogeneous 1–D approximation. Finally, Chapter 6 presents the major conclusions from this work alongside suggestions for future study.

1.2 Contribution

This work provides several contributions to both the current understanding of the effects of an air ingress into an HTGR as well as state-of-the-art experimental methods for modeling and studying such scenarios.

First, mixed-effects experiments involving the onset of natural convection within an

HTGR were conducted separately from those conducted to investigate the effect of high temperature, oxidizing flow on nuclear grade graphite. In this work, combined effects experiments were performed to examine the combined effects of these two related, but previously separately studied, phenomenons. Following these mixed experiments, graphite samples used in said experiments were tested to determine changes the combined high temperatures and varying air flow rates had on the graphite's thermal properties, such as its:

- Thermal Diffusivity
- Thermal Conductivity
- Density
- Emissivity

Secondly, several in-situ experimental and analytical techniques for high temperature experiments were also developed including:

- The use of thermal imaging to simply and precisely determine the onset of natural convection within an experimental system.
- A novel graph-theory based approach to the modeling of thermal dispersion and the prediction of temperature profiles within a packed bed of discrete elements using a semi-supervised machine learning method.

Finally, the understanding of the Onset of Natural Convection (ONC) phenomenon in HTGRs was furthered by the identification of two additional factors that would affect the time of ONC following an air ingress within an HTGR:

- The existence of the large reservoir of helium within the upper plenum of the reactor.
- The occurrence of a leak in the reactor's upper head.

The effects of each of these newly identified factors on ONC was quantified in terms of previous research and reactor designs.

Bibliography

[1] Won Jae Lee, Thomas YC Wei, and Richard R Schultz. Generation of a preliminary PIRT (phenomena identification and ranking table) for very high temperature gas-cooled reactors. Technical report, Korea Atomic Energy Research Institute, 2005.

[2] Hugh M McIlroy, Donald M McEligot, and Robert J Pink. Measurement of turbulent flow phenomena for the lower plenum of a prismatic gas-cooled reactor. *Nuclear Engineering and Design*, 240(2):416–428, 2010.

[3] Ibrahim A Said, Mahmoud M Taha, Shoaib Usman, Brian G Woods, and Muthanna H Al-Dahhan. Investigation of natural convection heat transfer in a unique scaled-down dual-channel facility. *AIChE Journal*, 63(1):387–396, 2017.

[4] Francisco Valentin. Study of Abnormal Heat Transfer During Forced and Natural Convection Scenarios in a Prismatic Core of a Vhtr : Numerical and Experimental Results. (October), 2015.

[5] Richard R Schult, Paul D Bayless, Richard W Johnson, James R Wolf, and Brian Woods. Scaling Studies for High Temperature Test Facility and Modular High Temperature Gas-Cooled Reactor. Technical report, Idaho National Laboratory (INL), 2012.

[6] Richard R Schultz, Paul D Bayless, Richard W Johnson, William T Taitano, James R Wolf, and Glenn E McCreery. Studies Related to the Oregon State University High Temperature Test Facility: Scaling, the Validation Matrix, and Similarities to the Modular High Temperature Gas-Cooled Reactor. Technical report, Idaho National Laboratory (INL), 2010.

[7] Xiaodong Sun, Richard Christensen, and Chang Oh. Investigation of Countercurrent Helium-air Flows in Air-ingress Accidents for VHTRs. Technical report, Battelle Energy ALliance, LLC, 2013.

[8] David J. Arcilesi. *Developmental Analysis and Design of a Scaled-down Test Facility for a VHTR Air-ingress Accident*. PhD thesis, Ohio State University, 2012.

[9] Chang H Oh, Cliff Davis, Larry Siefken, Richard Moore, Hee Cheon NO, Jong Kim, Goon C Park, John C Lee, and William R Martin. Development Of Safety Analysis Codes And Experimental Validation For A Very High Temperature Gas-Cooled Reactor. Technical report INL/EXT-06-01362, Idaho National Labratory, Idaho Falls, 2006.

[10] Chang H Oh and Eung S Kim. Air-ingress analysis: Part 1. Theoretical approach. *Nucl. Eng. Des.*, 241(1):203–212, 2011. ISSN: 00295493. DOI: 10.1016/j.nucengdes.2010.05.064.

[11] Chang H Oh, Hyung S Kang, and Eung S Kim. Air-ingress analysis: Part 2 Computational fluid dynamic models. *Nuclear Engineering and Design*, 241(1):213–225, 2011. ISSN: 0029-5493. DOI: 10.1016/j.nucengdes.2010.05.065. URL: http://www.sciencedirect.com/science/article/pii/S0029549310004127.

[12] David J. Arcilesi, Tae Kyu Ham, In Hun Kim, Xiaodong Sun, Richard N. Christensen, and Chang H. Oh. Scaling and design analyses of a scaled-down, high-temperature test facility for experimental investigation of the initial stages of a VHTR air-ingress accident. *Nuclear Engineering and Design*, 288:141–162, 2015. ISSN: 00295493. DOI: 10.1016/j.nucengdes.2015.03.007.

[13] Tae K Ham, David J Arcilesi, In H Kim, Xiaodong Sun, Richard N Christensen, Chang H Oh, and Eung S Kim. Computational fluid dynamics analysis of the initial stages of a vhtr air-ingress accident using a scaled-down model. *Nuclear Engineering and Design*, 300:517–529, 2016.

[14] Hyung Gon Jin, Hee Cheon No, and Hyeon Il Kim. Stratified flow-induced air-ingress accident assessment of the gamma code in htgrs. *Nuclear Engineering and Design*, 241(8):3216–3223, 2011.

[15] Hyung Gon Jin, Hee Cheon No, and Byung Ha Park. Effects of the onset time of natural circulation on safety in an air ingress accident involving a htgr. *Nuclear Engineering and Design*, 250:626–632, 2012.

[16] Seungjin Kim, Mohan S Yadav, Justin D Talley, Andrew Ireland, and Stephen M Bajorek. Separate effects experiments for air-ingress in helium filled vessel. *Experimental Thermal and Fluid Science*, 49:1–13, 2013.

[17] Antonio Campo, Mohammad M Papari, and Eiyad Abu-Nada. Estimation of the minimum prandtl number for binary gas mixtures formed with light helium and certain heavier gases: application to thermoacoustic refrigerators. *Applied Thermal Engineering*, 31(16):3142–3146, 2011.

[18] Jun Liu and Guenter Ahlers. Rayleigh-benard convection in binary-gas mixtures: thermophysical properties and the onset of convection. *Physical Review E*, 55(6):6950, 1997.

Chapter 2

Onset of Natural Convection

2.1 Introduction

The underlying physics for the transition from molecular diffusion to natural circulation is highly dependent upon the concentration of Helium within the core. If the overall Helium concentration is high, the difference in average fluid density between the hot core region and gap region (the space between core barrel and vessel wall) is insufficient to initiate natural circulation. Only when the air concentration in the core reaches a certain value will the density difference between the hot and cold legs be sufficient for the natural circulation of cavity air through the core to begin. Most of the experimental high temperature studies on understanding this transition were conducted by JAERI[1–3] with an 'inverted U' shaped experimental facility based on the HTTR. Although there are coolant inlet-outlet process design differences between HTTR and GT-MHR, the central physics of depressurization and air-ingress are expected to be governed by similar fundamental mechanisms. These experimental results were also later modeled using the CFD code, FLUENT, by Zhai et al. [4, 5]. While the experimental studies from JAERI do indeed help in understanding the transition, the 'inverted U' design does not take into account the possible effect of the upper plenum on molecular diffusion and air ingress rate.

As one can see in Figure 1.1a, the upper plenum of the proposed GT-MHR reactor design resides directly above the entrance to the coolant inlet channel. After a break, the helium contained within the upper plenum of the reactor will diffuse downward. This process will have the effect of slowing the rise in air concentration in the upper part of the reactor and thus potentially changing the time at which ONC would occur. Thus, a new 'h' shaped experimental facility designed to represent the effect of unmixed helium in the upper plenum was developed and used for the experimental studies presented in this work.

The experimental studies presented here have two goals: a) Experimentally study diffusion to natural circulation transition process with air-ingress into the helium filled chamber. b) Examine the effect of helium filled, upper plenum on ONC. The remainder of this chapter is organized into 4 sections respectively detailing: an experimental study on the effects of the upper plenum on ONC, the modeling of the aforementioned experiemnts using CFD, an

experimental study into how the occurrence of a leak in the upper head of a modular HTGR could affect the baseline ONC trends, and all conclusions reached.

2.2 Effect of Upper Plenum on Onset of Natural Convection

2.2.1 Experimental Setup and Procedure

To experimentally determine the effect that helium diffusion from the upper plenum might have on the ONC time, a new experimental setup was designed, based on the 'inverted U' design of experimental setups from literature [1, 3]. The 'h' shaped experimental setup developed for this study is made of quartz tubing welded together as shown in Figure 2.1a. Tube diameters for all the legs in the set-up were selected to be similar to those in the 'inverted U' shaped setup used in previous studies [3]. While visually very similar to setups developed by JAERI, such as the example shown in Figure 2.1b, the additional vertical tube seen on the upper left side of the apparatus provides several advantages.

First, the extended upper leg of the "h" allows a mass of helium to be present above the 'inverted U' flow loop, modeling the effect that the helium within the upper plenum of the GT-MHR would have on the time duration experienced from the initial coolant pipe rupture and depressurization until ONC. Secondly, the extended upper leg allows for the insertion of instrumentation and test specimens into the left leg of the assembly. In future studies, this upper leg and the flange will be used to create a scenario of 'control drive nozzle break' postulated accident listed as one of the tests in the matrix provided by Schulz et al. [6].

As presented in Figure 2.1a, the three legs in the apparatus were made of 46mm ID by 50mm OD quartz tube. It should be noted here that 'inverted U' facility at JAERI had ID of all the tube legs about 40.5mm, but this small variation in the tube area is not expected to play any major in the governing physics. The length of each legs was designed based on the geometric scaling with GT-MHR, i.e., the ratio of upper unheated leg to the heated

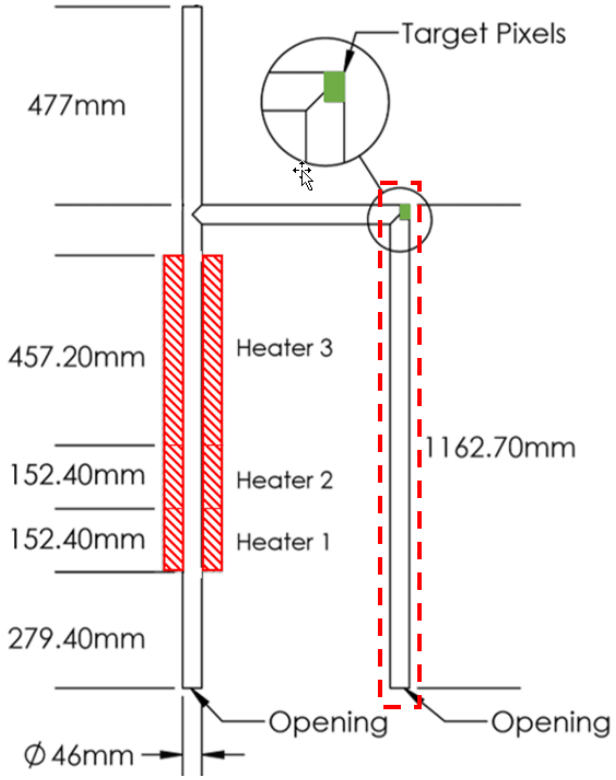

(a) *Diagram of 'h' shaped experimental apparatus developed for this study. Dashed red box highlights the observation window for ONC detection.*

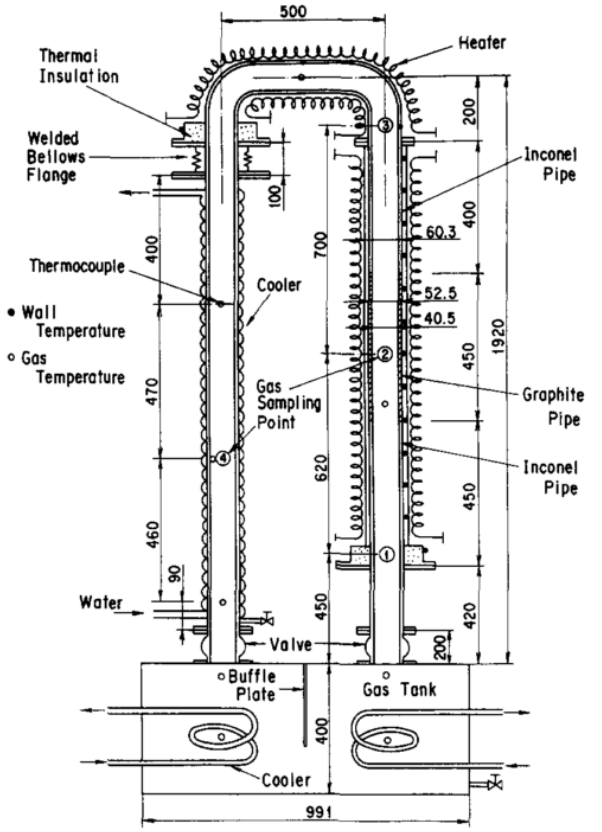

(b) *Diagram of 'inverse U' shaped experimental apparatus from JAERI. shown dimensions in mm. [3]*

Figure 2.1: *Experimental Setups for studying transition or Onset to Natural Circulation*

leg was designed to be 1.5 which is close to the ratio of height of upper plenum to core in the GT-MHR. The heights of GT-MHR core and upper plenum regions were obtained from literature [7, 8]. Low thermal conductivity of quartz eliminated the need for a cooling system on the cold leg of the assembly. Radiative tube furnaces were used to heat the lower portion of the left leg of the 'h' shaped test section.

The manufactured quartz 'h' is originally open to atmosphere at each of its three ends. Before initiating the experiments, all three openings were sealed using KF50 flange connections. For this ONC study, the two lower fittings were opened to simulate a sudden double guillotine break of the main coolant pipe. The third, upper opening remained sealed throughout the experiments performed for this work.

A FLIR A655sc LWIR camera was used to monitor the temperature of the setup before

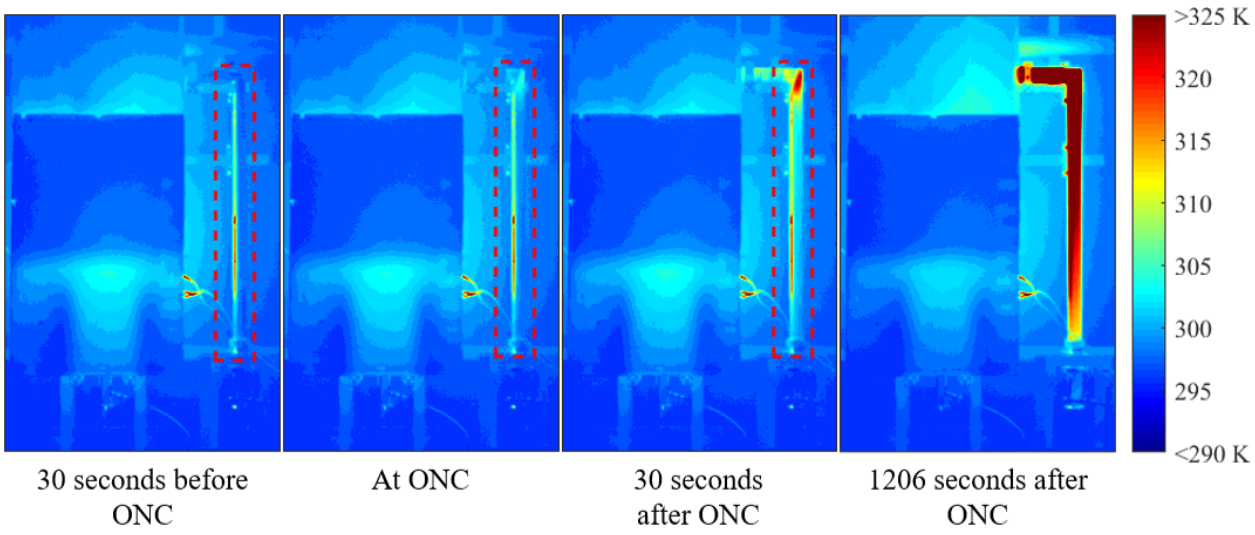

Figure 2.2: *Images from FLIR camera before and after ONC. Observation window is identified by dashed red box.*

and during experiments. Before each experimental run, the LWIR camera was used to determine when the apparatus had reached steady state conditions. In Figure 2.1a, the portion of the apparatus that can be directly observed with the LWIR camera is marked with a red dashed box.

During each experimental run, the LWIR camera was also used to detect the precise moment that the ONC occurred. This was done by continuously monitoring the values of the pixels making up the upper right corner of the quartz assembly. The approximate location of these pixels is also shown in Figure 2.1a. It was found that, after ONC, the upper-right corner of the quartz 'h' would be the first area to experience any measurable temperature change as shown in Figure 2.2. By tracking the average value of 40 pixels in this area denoted as "Target Pixels" in Figure 2.1a), ONC could be identified within seconds of it occurring. For example, the histories of the average temperatures in the targeted pixels plotted in Figure 2.3 clearly show the ONC during the experimental runs performed with a hot leg temperature of 375 degreeCelsius.

The measurement of ONC by the LWIR camera was also confirmed using a TSI 8475 flow transducer that was placed directly under the lower left opening of the assembly. Both of these measurement methods generally agreed on the ONC time to within 10 seconds of

one another.

The following steps were followed for each run of the ONC experiments.

1. Air is evacuated from the chamber with the help of vacuum pump and a rough vacuum is achieved.
2. Helium is filled into the chamber until pressure inside the chamber is almost equal to atmospheric pressure.
3. The left leg of the chamber is heated to the desired temperature.
4. Any excess helium is removed to ensure chamber pressure equal to atmospheric pressure.
5. Both of the lower ends of the chamber are opened simultaneously.
6. The flow measurement probe is moved into place under the left hand side chamber opening.
7. Chamber wall temperature and system flow rate are monitored to determine ONC.

2.2.1.1 Results and Analysis

As described in the previous section, ONC was detected when the instantaneous average value of the pixels identified in Figure 2.1a underwent a sudden, very steep change. This "steep change" can be seen in Figure 2.3. The time histories of the three test runs at the same hot leg temperature also show the consistency of the experimental results.

The ONC times experienced by the setup were measured for five different hot-leg temperatures. For each tested hot-leg temperature, several experimental runs were performed both to ensure experimental repeatability and to obtain data with uncertainties. The particular hot-leg temperatures used in this work were picked to closely match the hot-leg temperatures used in previous work reported by JAERI[3]. Experimentally measured ONC times from both the present work and JAERI's previous study[3] are plotted in Figure 2.4. Results from both studies show that as the temperature of the hot-leg is increased, the ONC time is

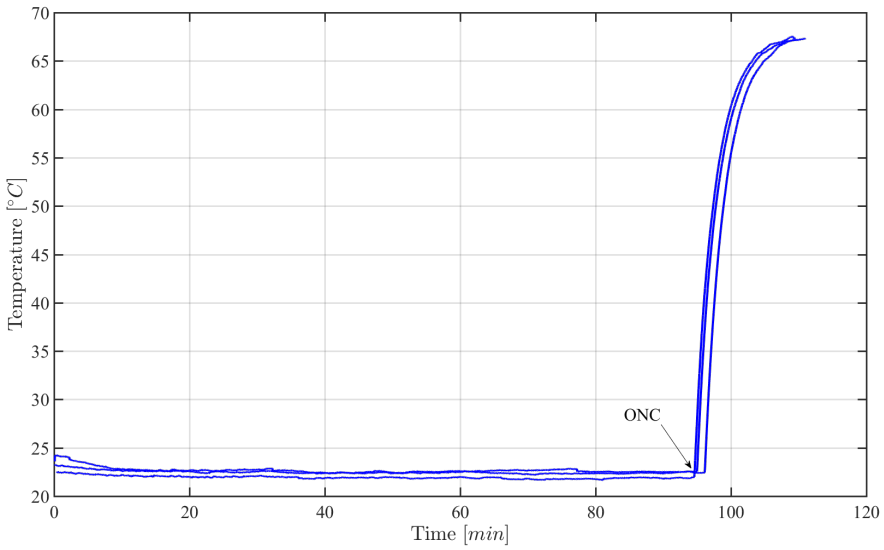

Figure 2.3: *Average temperatures of target pixels over several trials. Figure from Ref. [9]*

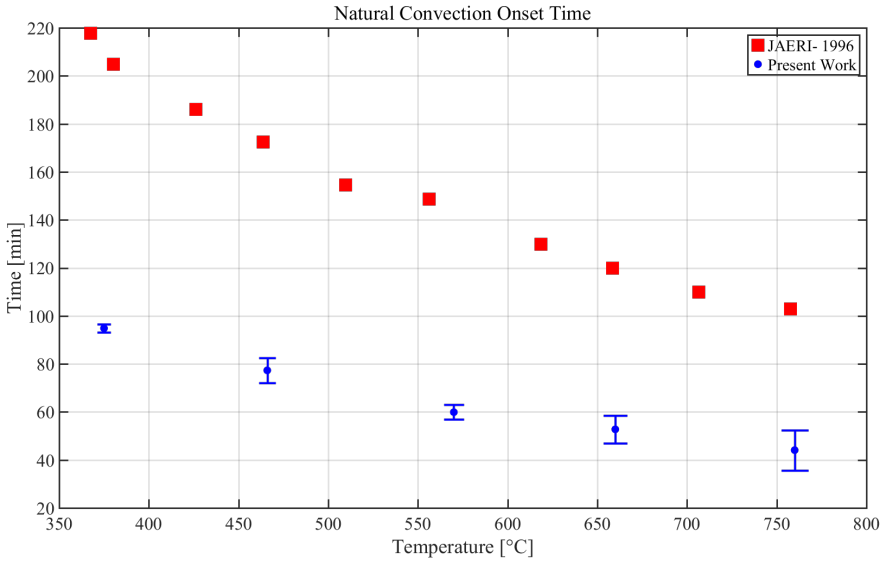

Figure 2.4: *ONC time (t) vs hot leg Temperature*

reduced. This behavior is expected and can be explained by increase in molecular diffusion and increased density difference driven convection currents with increase in temperature of the hot-leg.

2.2.1.2 Calculation of Diffusion Coefficient and Experimental Time Constant

In order for valid comparisons to be made between the results of the present work with those of JAERI, several small differences between the two setups had to be accounted for (see Table

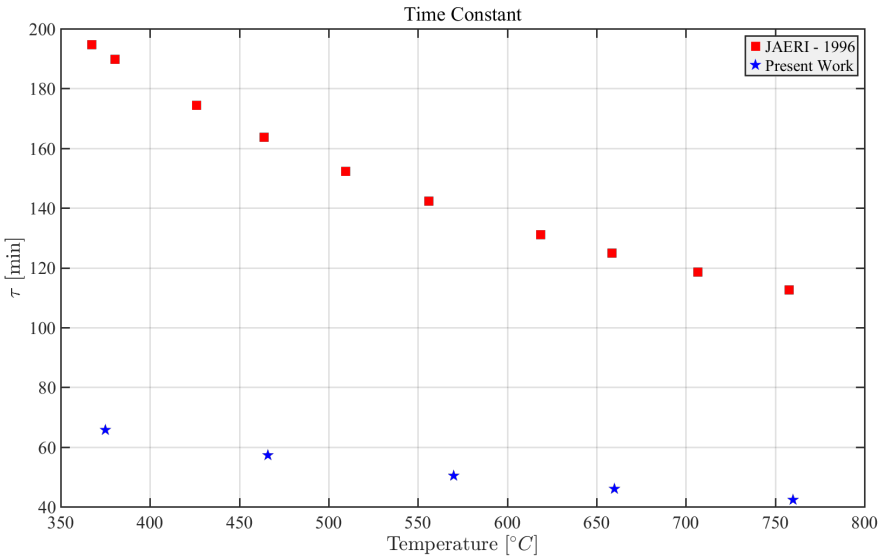

Figure 2.5: *Diffusion time constant (τ) vs hot leg Temperature*

2.1). First, and most significantly, while the horizontal tube connecting the two long legs of both experimental setups are identical in length, the vertical legs used in the 'inverted U' setup are longer than the lower portions – that is, the portions of the legs below the horizontal connecting tube – of the vertical legs that were used in the experiments described here. Additionally, slightly different fractions of the hot legs were actually heated to the specified temperature. Additionally, some of the most relevant or comparable results from JAERI [1, 2], were obtained using helium and nitrogen rather than helium and air.

Therefore, to take into account these variations, the time constant τ was defined to better understand and scale the processes in the two different facilities. This time constant was derived based on the assumption that, prior to ONC, molecular diffusion is the dominating mechanism for increasing the air concentration within the test chambers.

When calculating τ, the hot vertical leg – i.e. the lower portion of the left vertical leg in the current work, (see Figure 2.1a) and the right vertical leg in the previous work by JAERI (see Figure 2.1b) – were, for analytical purposes, split into a number of segments. Each segment was defined in such a way as to approximate that, under steady-state conditions prior to ONC, the temperature – and therefore diffusion coefficient – of each segment was constant over its length. This constraint resulted in dividing the hot leg of the JAERI setup into two segments. The hot leg of 'h' shaped setup, developed and used in this present study,

	Present Work	JAERI -1996[3]
Leg Length [m]	1.216	1.92
Heated Length [m]	0.82	1.50
Interior Diameter [mm]	46	40.5
Exterior Fluid	Air	N_2

Table 2.1: *Experimental Setup Comparison*

was divided into three segments.

The total time constant of the entire hot leg was then defined as the sum of the individual time constants of the individual segments within the analyzed leg. In Equation 2.1, L_j is defined as the length of segment j and D_j as the diffusion coefficient in segment j.

$$\tau = \sum_j \left[\frac{L_j^2}{D_j}\right] \tag{2.1}$$

Equation 2.2 is used to calculate the diffusion coefficient for gas pairs (D_i)of non-polar, non-reacting molecules [10] within a segment of the hot leg. Subscript i denotes a particular gas pair such as Helium-Nitrogen. In case of Helium-Air, the diffusion coefficient was modeled with Helium-Nitrogen and Helium-Oxygen pairs. Wilke's approximation (Equation 2.3) was used to calculate the overall diffusion coefficient of helium into air (D_j) from the diffusion coefficients of binary mixtures of its major components [11].

$$D_i = \frac{.001858\, T^{3/2}\left[\frac{1}{M_A}+\frac{1}{M_B}\right]^{1/2}}{P\sigma_{A-B}^2\Omega_D} \tag{2.2}$$

$$D_j = \left[\sum_i \frac{y_i}{D_i}\right]^{-1} \tag{2.3}$$

In Figure 2.5, the values of τ calculated for the experimental conditions reported by JAERI [3] and the present study are plotted as a function of the temperature of the heated segment of the hot leg. The large variation in *tau* values as a function of temperature is expected as higher temperature leads to higher diffusion coefficient which implies the diffusion process is expected to be faster. The differences in the τ values for the two facilities is attributed to the differences in the length of the heated segments which strongly govern

the diffusion process.

2.2.1.3 Effect of Extended Leg

The effect of the extended leg on the ONC transition phenomenon is illustrated by the ratio of $\frac{\tau}{t}$ as calculated for each specific test temperature. This ratio is plotted in Figure 2.6. It can be clearly seen from the plots that for all hot-leg temperatures tested, the ratio of $\frac{\tau}{t}$ calculated using the data generated in this work is lower than that calculated using the data from equivalent temperatures reported by JAERI[3]. This observation can be explained by the extra helium in the upper, extended portion of the left leg in the present setup. During the experiment, the helium initially present in the portion of the left leg above the horizontal cross diffuses downward into the lower portion of the apparatus – reducing the average air concentration in the lower leg and thus delaying ONC.

In both studies, the value of the ratio $\frac{\tau}{t}$ is directly proportional to the temperature. This behavior is due to the reduced dominance of molecular diffusion as the cause of increasing air concentration at higher temperatures. At higher temperatures, intra-leg natural convection also begins to play a role as predicted in the literature [1, 2]. It should be noted that although the value of the ratio $\frac{\tau}{t}$ seen in the present work is uniformly lower than than respective values generated from the JAERI experiments, the difference between the two respective ratios is not constant for all tested temperatures. Rather, the magnitude of the overall difference between the respective ratios plotted in Figure 2.6 appears to decrease with the hot leg temperature. This result can be partly attributed to 'natural convection' [1] that occurs within each leg of the experimental apparatus before ONC. As the temperature of the hot leg will be directly proportional to the flow rate of the intra-leg convection currents, at higher temperatures these currents will be much more effective at introducing air into the hot leg of the setup. Correspondingly, the relative importance of diffusion in determining the air concentration within the hot leg will decrease as the temperature of the hot leg is increased. Thus, at higher temperatures the relative effect of the downward-diffusing helium on the ONC time decreases and the ratio of $\frac{\tau}{t}$ for the 'h' shaped experimental setup will

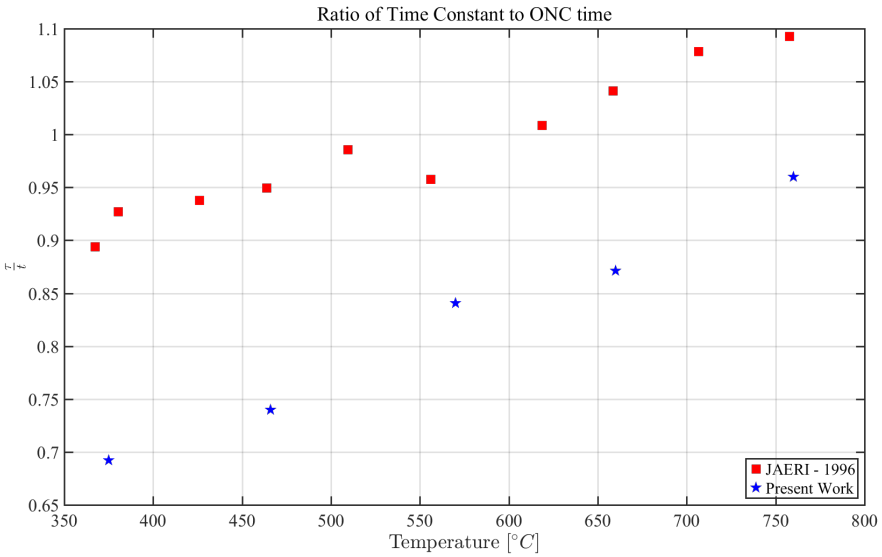

Figure 2.6: *Ratio ($\frac{\tau}{t}$) vs hot leg Temperature*

approach the respective values obtained from the 'inverted U' shaped apparatus.

2.2.1.4 Flow Velocity

A flow transducer, described in experimental section, was placed under the lower opening of the left leg of the "h" shaped apparatus to provide corroboration of the ONC times identified by the LWIR camera. This flow instrument additionally helped in obtaining measurements of the average flow velocities at the tube entrance post-ONC. Due to both the extremely low flow rates and the close proximity of the heater to the flow transducer, flow rate measurements were associated with a high degree of uncertainties and were not sufficient to obtain a meaningful correlation between flow rates and the hot leg temperature. However, the flow velocity measurements that were obtained do agree very well with the approximate 0.2 $^{m}/_{s}$ value reported in earlier reports [2]. The obtained velocity measurements are plotted in Figure 2.7 with error bars showing ± 2 SD of the measured values for each hot leg temperature. The accuracy level of the velocity probe was not sufficient to measure velocities prior to ONC or to quantify the role of intra-leg natural convection currents – an unsurprising fact given that these currents are expected to be on the order of 1E-6 $^{m}/_{s}$ to 1E-4 $^{m}/_{s}$.d

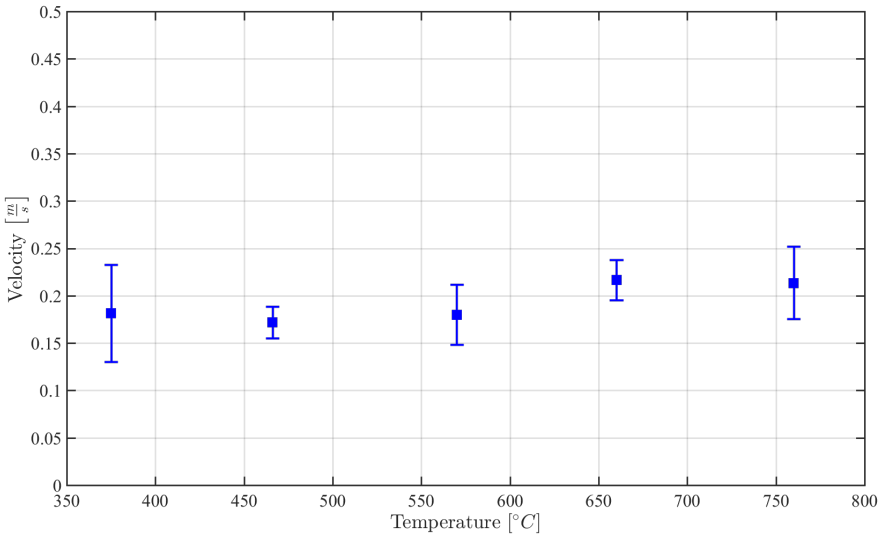

Figure 2.7: *Flow velocity at hot leg inlet after ONC*

2.3 CFD Study

2.3.1 Model Description

The geometry for the numerical model was based on the dimensions of the experimental setup described in Section 2.2.1. To reduce computation requirements, symmetry boundary conditions were used where possible. The resulting computational geometry is shown in Figure 2.8. The computational model is divided into three major domains or regions: the heated section, the unheated section, and the open section. The *heated section* is the region where the external heaters were located in the experimental setup. The *unheated section* refers to the domain representing the unheated regions of the experimental test section. The *open section* is the domain used to simulate the relevant region of air underneath the openings of the experimental test setup.

Since the experiment occurs at atmospheric pressure, no initial depressurization of helium is considered. As there are no known significant flow perturbations, flow is expected to be low speed and laminar. The unsteady Navier-Stokes equations and continuity equation for the flow were solved using ANSYS CFX commercial code. The energy transport and helium-air concentration fields are computed using the multi-physics coupling of the Navier-Stokes equations with the energy equation and the scalar transport equation, respectively. The

mathematical form of the equations used in the model are described below.

The continuity equation is

$$\frac{\partial \rho}{\partial t} + \nabla \cdot (\rho \mathbf{U}) = 0, \tag{2.4}$$

and the Navier-Stokes equation(s) is

$$\frac{\partial (\rho \mathbf{U})}{\partial t} + \nabla \cdot (\rho \mathbf{U} \otimes \mathbf{U}) = -\nabla p + \nabla \cdot \tau, \tag{2.5}$$

where,

$$\tau = \mu \left(\nabla \mathbf{U} + (\nabla \mathbf{U})^T - \frac{2}{3} \nabla \cdot \mathbf{U} \right)$$

.

The energy equation is

$$\frac{\partial (\rho H_{tot})}{\partial t} - \frac{\partial p}{\partial t} + \nabla \cdot (\rho \mathbf{U} H_{tot}) = \nabla \cdot (k \nabla T) + \nabla \cdot (\mathbf{U} \cdot \tau) \tag{2.6}$$

$\nabla \cdot (\mathbf{U} \cdot \tau)$ = work due to viscous stresses.

The scalar transport (convection-diffusion) equation is

$$\frac{\partial (C)}{\partial t} + \nabla \cdot (\mathbf{U} C) = \nabla \cdot (D_{AB} \nabla C), \tag{2.7}$$

The thermo-physical properties of helium and air used in this model were determined through the ideal gas law and vary with temperature and pressure. Remaining thermophysical properties such as viscosity were obtained from the National Institute of Standards and Technology (NIST) web book.

Molecular diffusivity was again modeled with Equation 2.2 as a function of the local fluid

temperature and pressure. The mesh created for the experimental geometry diagrammed in Figure 2.1a is shown in Figure 2.8b.

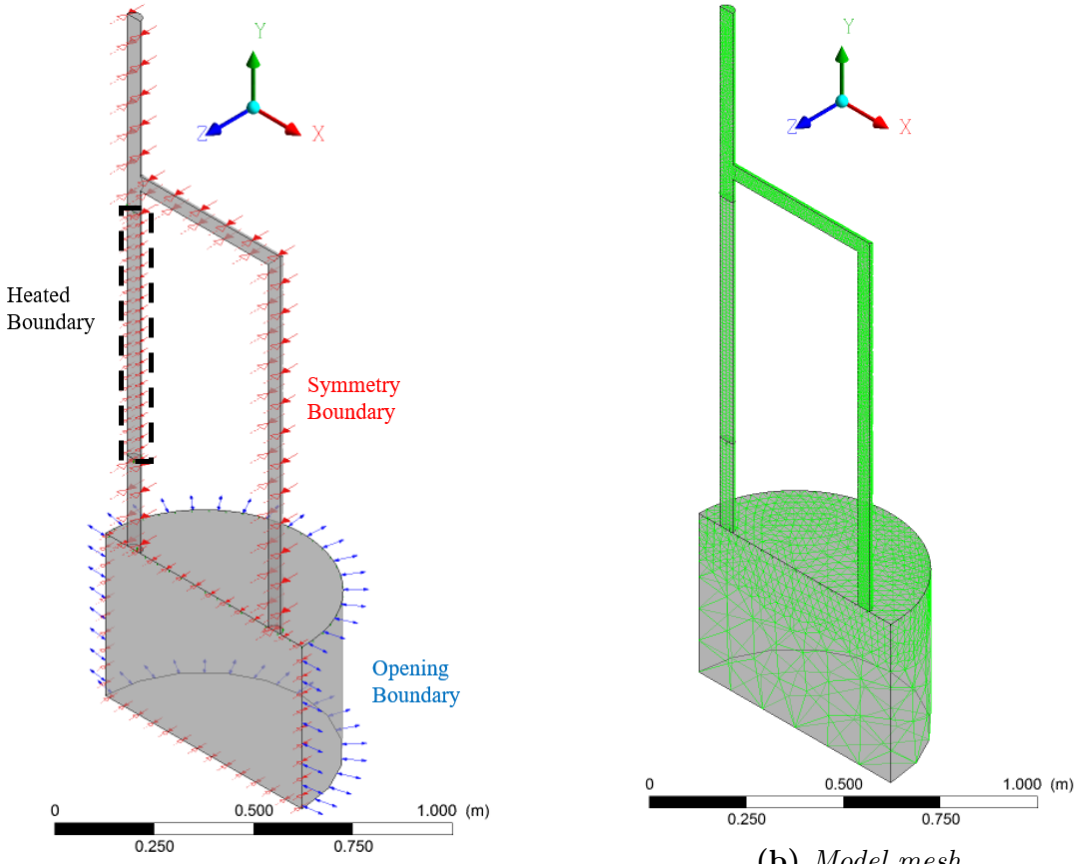

(a) *Model boundary conditions*

(b) *Model mesh*

Figure 2.8: *Model boundary conditions and mesh*

2.3.1.1 Boundary and Initial Conditions

The model was divided into three different regions, each with different initial and boundary conditions. The initial conditions for the transient CFD model were established by first running steady state simulations with a closed helium environment in the experimental setup. The steady state simulations conducted gave an accurate initial temperature profile of the helium within the pipes. The steady state temperature profile was generated using a fixed temperature boundary condition on the cylindrical surface of heated section. This closely models the experimental conditions, in which a constant temperature was maintained near

the surface of the cylindrical tube with radiative heaters. Due to the still air outside the apparatus, the heat transfer between the wall and the outside environment can be approximated as having a heat transfer coefficient of $h = 1\frac{W}{m^2K}$ and an external temperature of 20°C [12]. This heat transfer coefficient was calculated by assuming that a laminar natural convection condition was present on the outer surface of experimental setup.

For the initial steady state simulation, the boundary between the h-section and the open section remained closed and adiabatic. The open section remained at standard atmospheric pressure and was at a temperature of 295K during steady state simulations. Steady state simulation results with a helium-filled test setup under closed conditions are shown in Figure 2.9. These simulation results are used as input for the transient cases. The transient simulation started with the opening of the previously closed boundary between h-section (or test setup) and the open section. The total time for the transient simulations was determined based on the time taken to achieve a new steady state, when the total volume of the test setup is filled with air and constant natural circulation is established.

The numerical scheme selected for these simulations was the second order backward Euler. A multi-grid (MG) accelerated, incomplete lower-upper (ILU) factorization technique is used for solving the discrete system of linearized equations. Each simulation was started with an initial time step of 0.001s and had a maximum time step of 0.1s. A maximum RMS residual value of 10^{-3} was used as the convergence criterion for each time step. The time step was adaptively adjusted based on the number of coefficient loops needed to meet the convergence criterion. If the convergence criterion was met in under 6 coefficient loops, the time step was increased by 5%, and if the number of loops was over 8, then the time step was decreased by 20%.

Table 2.2: *Mesh Sensitivity Study Results*

	Mesh 1	Mesh 2	Mesh 3
Number of Elements	27,027	37,324	53,004
Mean U before ONC [$\mathrm{m\,s^{-1}}$]	1.63E-3	1.51E-3	1.50E-3
Mean T before ONC [°C]	760.02	760.01	760.02

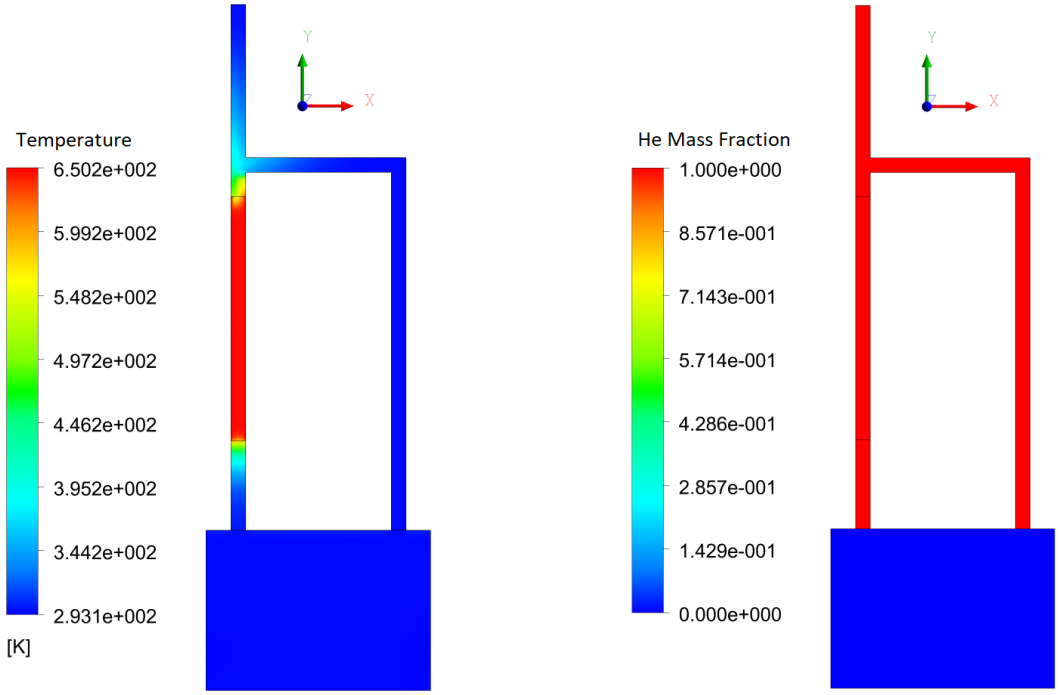

Figure 2.9: *Initial temperature and mass fraction distributions before transient simulation.*

2.3.1.2 Mesh details and convergence

Different meshes were generated for the model described above in ANSYS Workbench. Mesh dependency was studied through the use of meshes of varying densities. The lowest resolution mesh had a total of 8,095 nodes and 27,027 elements; even this mesh density proved to be sufficient in predicting ONC time.

2.3.2 Results

Different numerical simulations were conducted with external heater temperatures varying from 375-760°C, corresponding to the experimental cases described in Section 2.2.1. Example simulation results of the temporal progression of air entering the test chamber from the open section are shown in Fig. 2.10. These contour plots show a clear difference in the rate of air ingress between hot and cold legs. This difference can be partly attributed to a higher diffusion constant at a higher temperature in the hot leg. In Fig. 2.10, the final two contour plots corresponding to time stamps 5,460 secs and 5,520 secs show that within 60

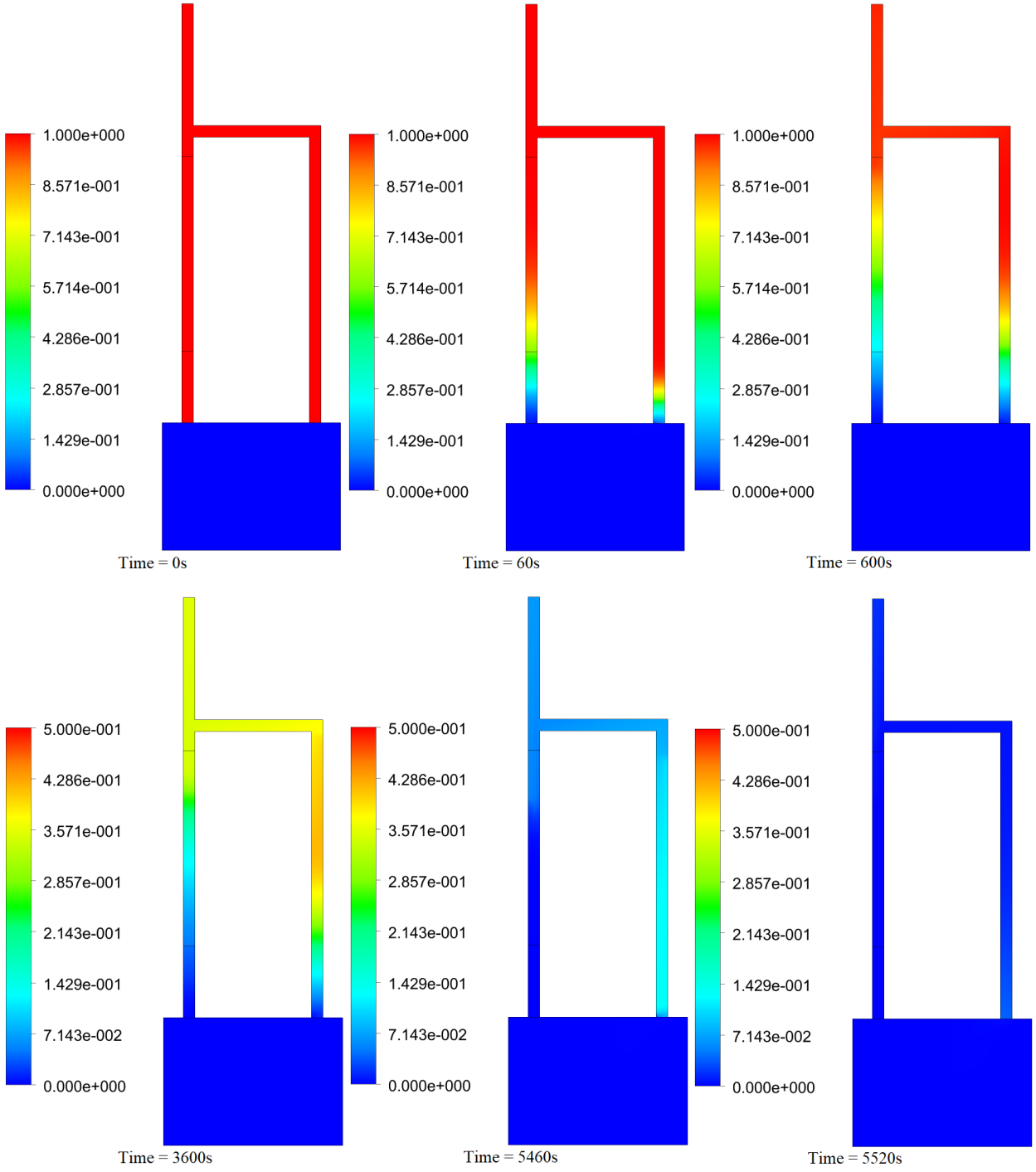

Figure 2.10: *Helium mass fraction vs time at 375° C.*

seconds or a 1-minute interval, there is a very large variation in helium concentration or mass fraction. This shows the transition point from diffusion-driven to natural circulation driven air ingress. Temperature pseudocolor plots are shown in Fig. 2.11. These plots show

the fluid temperature within the system also making a sudden jump during the last two data points obtained before ONC.

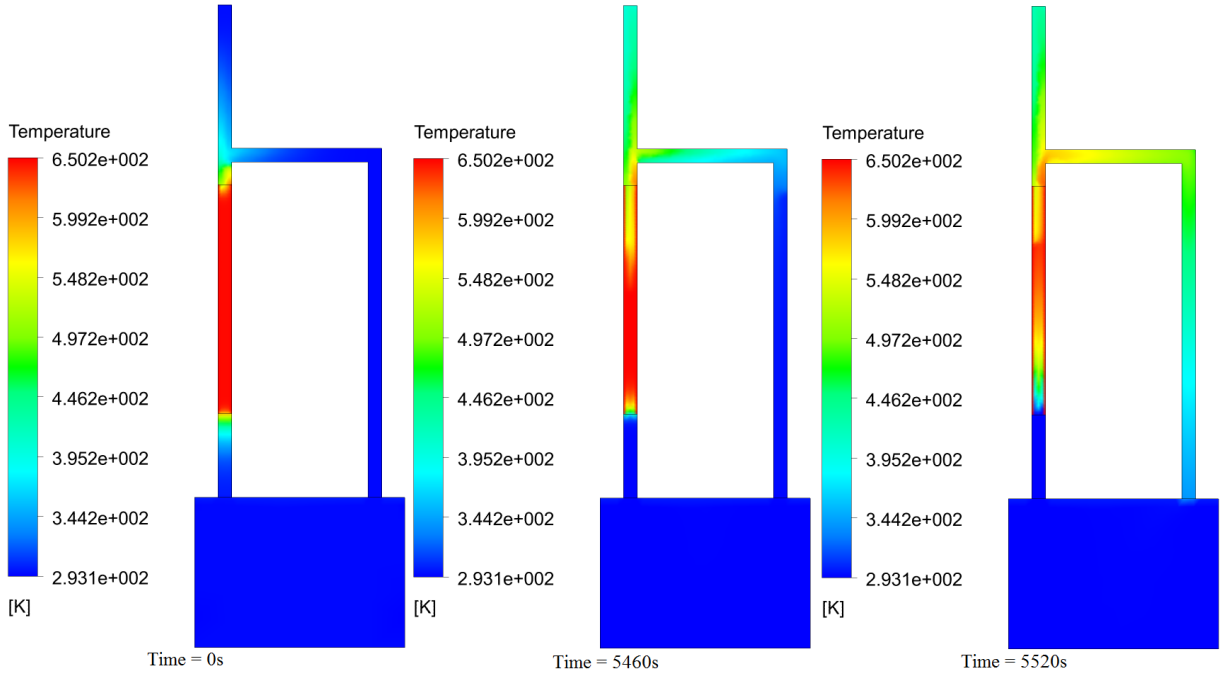

Figure 2.11: *Temperature profile before and after ONC.*

To quantitatively understand the influence of the extended leg in an h-shaped test setup, the spatial average air concentration versus time in different legs (colds leg, hot leg and extended leg) are plotted together in Fig. 2.12. The air concentration in the extended leg is lowest as compared to the other two legs, which implies that the extended leg has a higher average helium concentration than the rest of the setup for the most amount of time during the experiment. Therefore, the extended leg acts as an additional helium reservoir, which supplies additional helium to the inverse U-tube via diffusion.

The exact ONC time in these simulations is quantitatively defined, with a sudden inflection in temperature and velocity in the middle of the heated section. Example velocity versus time and temperature versus time plots for the middle transverse plane in the heated section are shown in Fig. 2.13. The sudden inflection in the temperature or velocity is observed throughout the test section.

The most important result of these simulations is the prediction of ONC times, as de-

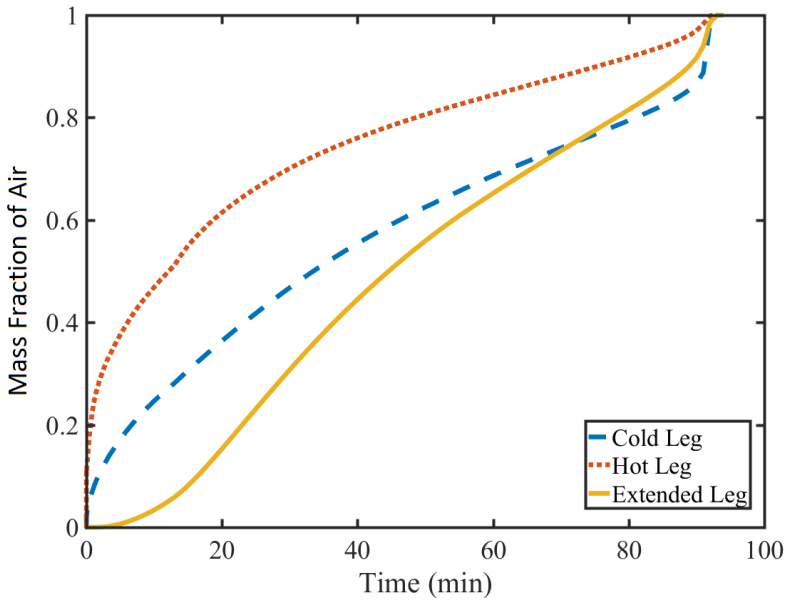

Figure 2.12: *Mass fraction of air in each leg during the 375° C run.*

scribed in the previous sections. The comparison between computational model predictions and experimental data can be seen in Fig. 2.14, which shows that the CFD models correctly predict ONC times in the experiment to within about 4%.

These numerical simulations show that the pre-ONC velocity magnitudes are very low ($O \sim 10^{-3} - 10^{-4}$ m/s), and as discussed in previous works, it is difficult to obtain the velocity measurements of such magnitude with high accuracy. Thus only post-ONC velocity data are available for validation purposes. The post-ONC velocity predictions computed from the numerical models are presented in Fig. 2.15 where they are plotted alongside the velocity data from Figure 2.7. These velocity predictions are close to the actual velocity measurements obtained for each of the different cases.

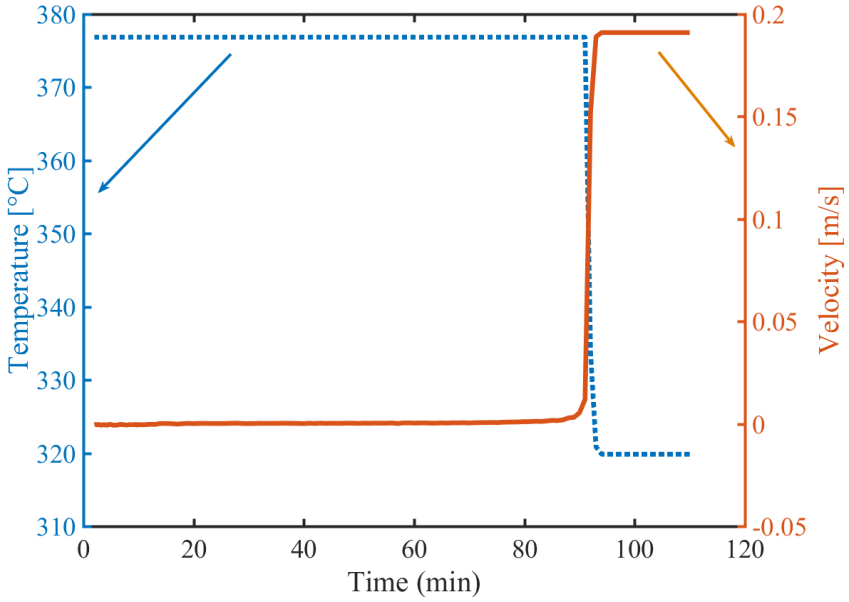

Figure 2.13: *Temperature and velocity in the middle of the heated section vs time at* 375 °C.

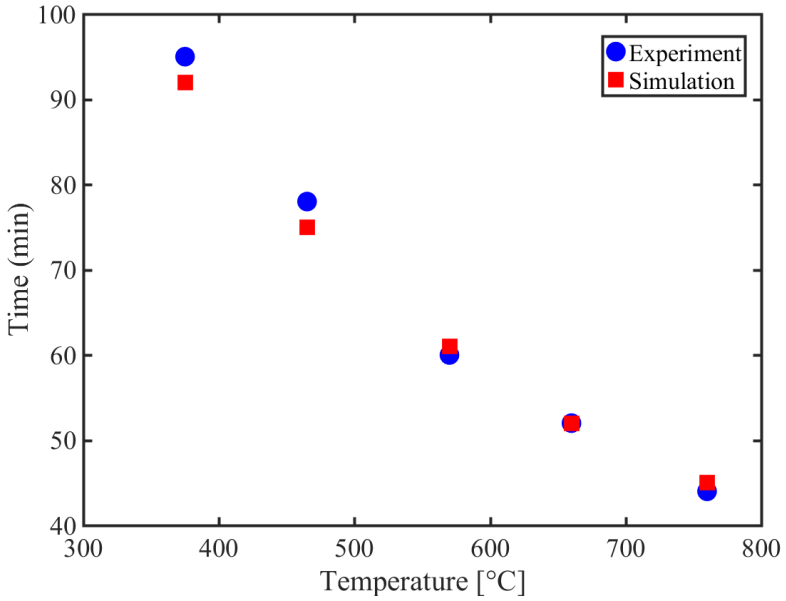

Figure 2.14: *ONC time vs hot leg temperature*

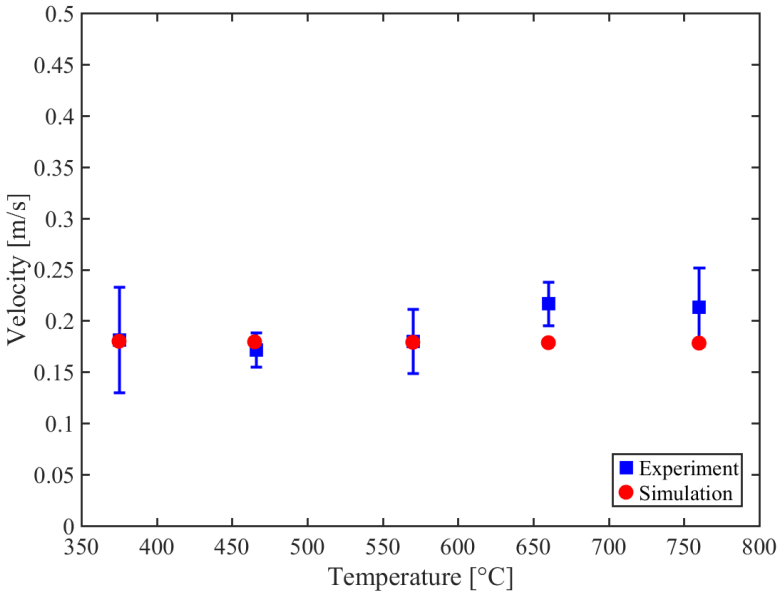

Figure 2.15: *Experiment vs predicted air ingress velocity during natural circulation at inlet of the setup.*

2.4 Effect of an Upper Head Leak

One of the geometric design features adopted in most HTGR designs is the location of the main inlet/outlet near the lower head of the reactor. In these designs, a major break in the main coolant pipe will lead to a sudden depressurization of the reactor vessel. After depressurization, although it has been shown that the lower plenum would likely be quickly filled with air from a stratified, density-driven flow , the remainder of the reactor would be filled with air much more slowly . This delay in air ingress into the core region is due to the slow nature of the helium-air diffusion process. It is anticipated that having the coolant inlet-outlet headers located near the lower head will be able to prevent any instantaneous air ingress into the core upon a break of the coolant headers. However, if, after the break of the main coolant pipe, a break or leak from the upper head were to occur as well, there is a possibility of instantaneous air ingress into the core as the then buoyancy driven, lighter Helium would rise upwards and exit the core through upper region leak or break location – thereby facilitating the ingress of air into the core region.

Two potential sources have been suggested for such a leak: breaks in either the reactor's control rod drive nozzles or in their instrumentation ports. For the MHTGR, the break of a .32 cm^2 instrumentation penetration in the reactor's upper head is specifically defined as an example of a design basis accident [13]. At the Fort St. Vrain HTGR, the control rod drive assemblies at the top of the reactor are recorded to have had significant fitting and reliability problems - including helium leaks [14]. Given that these difficulties were encountered under normal operating conditions, it is certainly not difficult to imagine that an external event could also induce a seal failure in such as system. However, these two examples are by no means the only potential areas of the upper head at which a leak could develop. The MHTGR upper head features numerous penetrations of sizes up to 1 m^2. Additionally, generic leaks from holes up to 6.5 cm^2 are specified as anticipated operational occurrences for the reactor.

While experimental work to characterize the effects of such a leak have been proposed before [15], less attention has been given to the possibility of an HTGR suffering a break in both an upper-head penetration and its main coolant pipe at the same time due to some

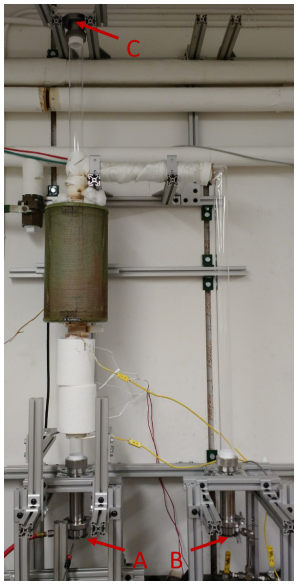

(a) *Picture of facility*

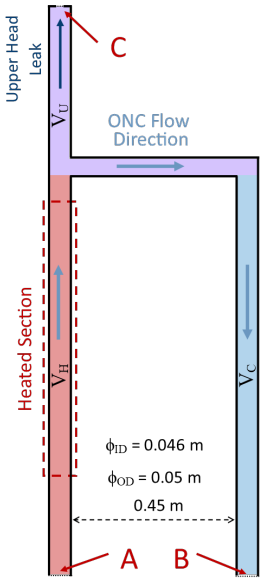

(b) *Diagram of experimental apparatus.*

Figure 2.16: *Experimental Setup.*

externally-initiated event. If this were to occur, it is possible that the Onset of Natural Circulation (ONC) time would be a function of both the amount of helium lost from the reactor due to diffusion and the amount lost due to the postulated leak in the upper head. Most worrisome, if the size of the upper head leak is large enough, the period of time prior to the ONC that would available for remediation efforts following a main coolant pipe break under a diffusion dominate scenario could be significantly reduced.

The goal of this work was thus to find the minimum size of an upper head hole that would result in the effects of the helium loss through the hole being the dominant factor in the determination of the onset of natural convection time following a loss of coolant accident due to a double guillotine break of the main coolant pipe. Towards this end, the experiments previously described in Section 2.2.1 were modified to also simulate the effect of an upper head leak (at the location marked 'C' in Figure 2.16) within the GT-MHR reactor and a model was created to apply the experimental results to the geometry of the proposed GT-MHR design.

2.4.1 Experimental Setup and Procedure

The 'h' shaped experimental setup used in this study is the same as previously used by Gould [9], based on the previous work of JAERI [1]. Figure 2.16a shows the experimental facility. The apparatus is made up of lengths of 46mm ID x 50mm OD quartz tubing. The length of each of the legs was selected based on geometric scaling with the GT-MHR, i.e., the ratio of upper unheated leg to the heated leg was set to be 1.5 – close to the ratio of height of upper plenum to core in the GT-MHR. The left leg of the assembly was heated using a combination of three tube furnaces. A diagram of the setup is also provided as Figure 2.16b, in which the openings A, B, and C are again identified along with the flow direction.

The following steps were followed for each run of the ONC experiments involving the potential effect of an upper head leak.

1. The left leg of the chamber is heated to the desired temperature.
2. Air is evacuated from the chamber until a rough vacuum is achieved.
3. The chamber is backfilled with helium to slightly above atmospheric pressure.
4. Excess helium is removed to bring chamber pressure equal to atmospheric pressure.
5. Helium is given approximately four minutes to reach a steady state temperature.
6. Both of the lower ends of the chamber (i.e. openings A and B) are opened simultaneously.
7. The adhesive seal is removed from top hole (i.e. opening C)
8. Chamber wall temperature is monitored with FLIR to determine ONC time.

To reiterate, the goal of this work was to find the minimum size of an upper head hole that would result in the effects of the helium loss through the hole to be the dominant factor in the determination of the onset of natural convection time following a loss of coolant accident due to a double guillotine break of the main coolant pipe. In this work, the effect of a leak in the upper head of an HTGR reactor occurring during such an accident was experimentally

modeled and an analytical model was created to scale the results from the experiments to the GT-MHR geometry. To compensate for the inability to precisely predict the amount internal mixing that would take place in the complex geometry of an HTGR after the main coolant pipe break, two lumped parameter models (the 'Plug Flow' and 'Mixed Flow' models described in Section 2.4.2.3) were created to analyse the limiting cases of either perfect, or negligible, molecular mixing withing the geometries of interest.

Experimentally, the addition of the simulated upper reactor head breach was shown to significantly reduce the amount of time from the simulated main coolant pipe break to the onset of natural convection. Using the τ_D/τ_h ratio to scale the effects of the hole from the experiment to the reactor indicates that not only would a upper head hole of the benchmark AOO-5 hole size likely significantly decrease ONC time, but that under certain circumstances, so also would the break of an instrumentation penetration. If the amount of mixing is minimal, the hole size required to dominate – much less match – the effects of diffusion falls far below the AOO-5 benchmark. Given that the reactor is expected to, at some point within its operational life, incur an AOO-5 size hole *without* an external event, it seems highly prudent to plan for such a hole being created or enlarged by the same external event that caused the double guillotine rupture of the main coolant channel.

2.4.2 Scaling

In order for the results given by the current experimental apparatus to be relevant to actual reactor designs, scaling analysis is necessary. Previously, a thorough scaling analysis was performed by Reyes et al. [16] on JAERI's experimental setup. For this work, a simplified scaling analysis was done with the goal of finding the relative effect of the potential upper head leak to that of the molecular diffusion as a function of temperature and leak size.

2.4.2.1 Geometric Considerations and Assumptions

Relevant geometric dimensions and ratios are provided in Table 2.3. The lower volume, V_L, is equal to the sum of the hot volume, V_{hot}, and the cold volume, V_{cold}.

	Experiment	GT-MHR
Flow Height [m]	1.22	9.88
System Height [m]	1.72	16.1
Hole Length [mm]	5	156
V_L $[m^3]$	4.06 E-3	31.3
V_U $[m^3]$	1.66 E-3	133
V_{hot}/V_{cold} $[m^3]$	1	1.24

Table 2.3: *Prototype and model physical dimensions*

As was previously done by Oh[17] in his analysis, in this study it was also assumed that the wall between the core region of the reactor – hereafter referred to as the hot leg – and the cold gas annular region – hereafter referred to as the cold leg – was perfectly thermally insulated. It was further assumed that the temperature of the fluid in the upper head region was simply the mean of the temperatures of the hot and cold legs.

Given the small size of the holes considered in this work as the source of the upper head leak, it was assumed that the pressure drops through the hot and cold legs of the reactor were negligible compared to that of the pressure drop imposed by the upper head hole. Although this assumption would become invalid if upper head holes of large enough size were considered, any hole size large enough to invalidate this assumption would also significantly alter the natural convection currents existing in the system following ONC and thus the effects of such holes are beyond the scope of this work.

It was also assumed that the pressure drop through the hot and cold legs of the system are approximately equal. Due to the identical shape and size of the hot and cold legs within the experimental setup, this assumption is valid for the experimental apparatus. However, for the actual reactor, this is not necessarily the case. If the pressure drop through the core of the reactor varies significantly from that of the cold leg, it is possible that the cyclic flow behavior predicted by Reyes et al. [16] might occur as the gradually-created imbalances in helium concentration between the two legs suddenly equalize as buoyancy forces become sufficient to initiate a sudden burst of natural convection. However, even if this behavior does occur, due to the approximately equal fluid volumes in the reactor hot and cold legs (see Table 2.3), few cycles are likely to occur before continuous, global natural convection is

achieved and the maximum difference in ONC time due to the cyclic flow will be equal to one period of the cycle.

2.4.2.2 Diffusion Scaling

In the full scaling analysis performed by Reyes et al, the diffusion time scale was defined as

$$\tau_D = \frac{L^2}{\bar{D}} \tag{2.8}$$

in which L is the vertical length of the hot and cold legs of the experiment or reactor. It should be noted that this time scale, at least as calculated by Equation 2.8, is solely describing the time scale of the diffusion of air from the bottom of each leg to the top of each leg. Previously, Gould et at. examined what additional effect the downward diffusion of the helium contained in the reactor's upper head region could have on its ONC time [9]. Although the authors did find that the downward diffusion of helium from a region above the hot and cold legs of the experimental apparatus did measurably affect ONC times, the simplified diffusion time scale calculated by Equation 2.8 was still found to be broadly applicable to the overall process as a whole. Thus, in this work the diffusion time scale was defined using Equation 2.8 and averaging the diffusion constants for the hot and cold legs.

2.4.2.3 Hole Scaling

Using the methodology described by Zuber et al. [18] for determining characteristic temporal scales, the temporal scale associated with the helium flux leaving from the upper head hole was defined as a ratio of capacity to transfer intensity. This time scale is given as Equation 2.9. The transfer intensity used in Equation 2.9 is calculated as the mean helium flux through the hole multiplied by the hole's cross-sectional area.

$$\tau_h = \frac{CV}{jA} \tag{2.9}$$

$$j\left(t\right)A_h = v_h\left(t\right)A_h C_h X_h\left(t\right) \tag{2.10}$$

From Equation 2.10, obtaining the molar flux of helium leaving out of the upper hole requires knowledge of flow velocity, hole area, total molar concentration at the hole, and the molar fraction of helium at the hole location over time. Of these quantities, the time dependent function the molar fraction of helium at the hole, $X_h\left(t\right)$, is the most difficult to obtain.

For any non-negligible upper hole size, the shape of the function $X_h\left(t\right)$will be determined by the amount of internal fluid mixing present in the system. Although previous work by JAERI has demonstrated very weak global natural convection to exist before ONC [1], the magnitude of the mixing effect of the weak natural convection seen in their experiments was on the same order as that of helium-air diffusion. Unfortunately, precise estimation of the magnitude and fluid volume affected by local natural convection ettys would require, at a minimum, specific details regarding the interior geometry and temperature distributions within the reactor core and upper head. Additionally, even armed with such information, obtaining usefully accurate and precise answers would require 3D CFD simulations featuring high mesh densities and taking massive amounts of computational power [19].

Thus, instead of attempting to calculate the precise amount of mixing present in the system, a partially lumped model of the system was created and two limiting cases of local mixing were defined. In the first case, referred to here as mixed flow, all helium and air within the system are perfectly mixed at all times. Thus, for this case, the helium molar fraction at the upper hole is equal to the system average helium molar fraction for all times (Equation 2.11a). The second limiting scenario, plug flow, simply assumes the opposite – no mixing of helium and air takes place within the system prior to ONC. This assumption results in $X_h = 1$ for all times (Equation 2.11b).

$$X_h\left(t\right) = \bar{X}\left(t\right) \tag{2.11a}$$

$$X_h(t) = 1 \tag{2.11b}$$

The approximate velocity of the flow emanating from the postulated upper head hole was calculated by the simple application of a mechanical energy balance to a streamline proceeding through the center of the hole. In Equation 2.12, the original equation is shown expanded and solved for v_h^2. In Equation 2.12c, the loss constant K was assumed to be 0.5 for the reservoir entrance.

$$\cancel{\frac{\bar{\rho}v_b^2}{2}}^{0} + \cancel{\bar{\rho}gz_b}^{0} + P_b = \frac{\bar{\rho}v_h^2}{2} + \bar{\rho}gz_h + P_h + \Delta h \tag{2.12a}$$

$$P_h = P_b - \rho_{atm}gz_h = P_{atm} - \rho_{atm}gH \tag{2.12b}$$

$$\Delta h = \frac{v^2}{2g}\left(\frac{fL}{d} + K\right) \tag{2.12c}$$

$$v_h^2 = 2\left(\frac{\rho_{atm}}{\bar{\rho}} - 1\right)gH - \Delta h \tag{2.12d}$$

The ideal gas law was used as the equation of state. It was assumed that the physics of the system could be adequately represented by treating temperature and density as lumped parameters. However, as the temperature – and therefore density – of the fluid within the system is significantly different, the geometry was broken up into three separate lumped sections: the hot leg, the cold leg, and the upper region.

The location of each of the three sections within both the experimental and reactor geometries are shown in Figures 2.17a and 2.17b, respectively. The composite "lower region", consisting of the combined volumes of the hot (V_H) and cold (V_C) legs, is also identified. Each section was assumed to have a uniform temperature and fluid density. The volume-weighted average density was then then calculated and used for the mean system density.

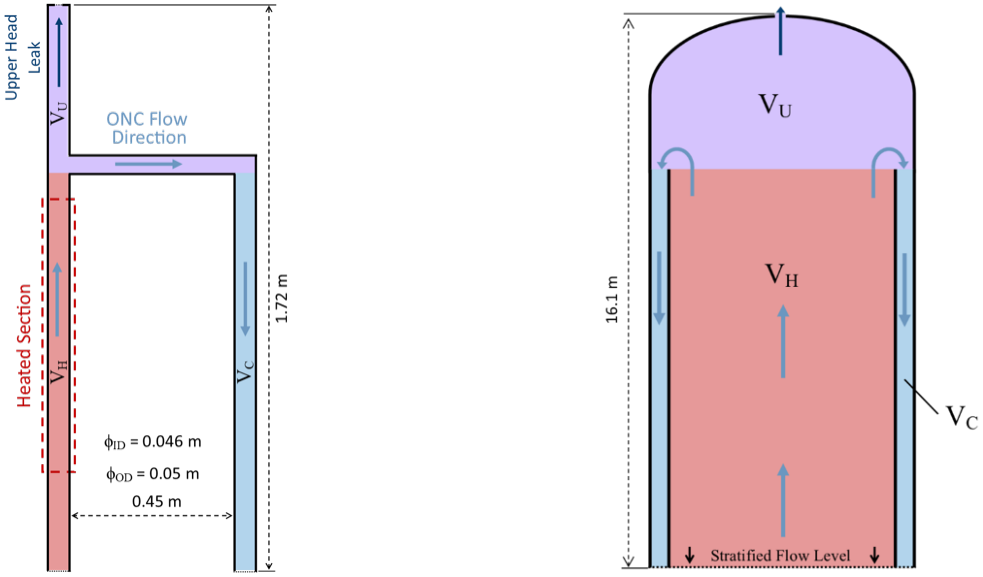

(a) *Diagram of model of experimental apparatus*

(b) *Diagram of reactor model*

Figure 2.17: *Model diagrams*

$$\rho_i(z,t) = X(z,t)\frac{P_{atm}}{R_{He}T(z)} + (1 - X(z,t))\frac{P_{atm}}{R_{Air}T(z)} \tag{2.13a}$$

$$\bar{\rho}_i(t) = \bar{X}(t)\frac{P_{atm}}{R_{He}\bar{T}_i} + \left(1 - \bar{X}(t)\right)\frac{P_{atm}}{R_{Air}\bar{T}_i} \tag{2.13b}$$

$$\bar{\rho}(t) = \sum \frac{V_i \bar{\rho}_i(t)}{V} \tag{2.13c}$$

Using the simplified equation of state given in Equation 2.13 to provide the system average density for Equation 2.12, a 1st order ordinary differential equation can be written for the change in the system average helium molar fraction, $\bar{X}$, with time. The general form of this differential equation is

$$\frac{d\bar{X}}{dt} = \frac{-j(t)A_h}{V\bar{C}} \tag{2.14}$$

For the mixed flow conditions specified by Equation 2.11a, the time dependent flux function in the numerator of Equation 2.14 can be rewritten as

$$j\left(t\right) = v_h\left(t\right) C_h \bar{X}\left(t\right) \tag{2.15}$$

The resulting differential equation for the mixed flow scenario is

$$\frac{d\bar{X}}{dt} = \frac{-v_h\left(t\right) A_h C_h \bar{X}\left(t\right)}{V\bar{C}} \tag{2.16}$$

In order to calculate the mean flux value used in the calculation of the hole time scales (Equation 2.17) for either of the two limiting scenarios, knowledge of the full temporal flux function, $j\left(t\right)$ was needed. To find this, Equation 2.14 was numerically integrated.

$$\frac{d\bar{X}}{dt} = \frac{-v_h\left(t\right) A_h C_h\left(1\right)}{V\bar{C}} \tag{2.17a}$$

$$\frac{d\bar{X}_L}{dt} = \frac{-v_h\left(t\right) A_h C_h\left(1\right)}{V_L\bar{C}_L} \tag{2.17b}$$

$$\tau_{h,plug} = \frac{\bar{C}_L V_L}{\bar{j}_{plug} A_h} \tag{2.18}$$

$$\tau_{h,mixed} = \frac{\bar{C}V}{\bar{j}_{mixed} A_h} \tag{2.19}$$

Matlab's ODE45 solver was used to numerically integrate Equations 2.16 and 2.17 while iteratively solving for the fluid velocity at every time step. For the case of the experimental setup, the mean flux through the top hole for either mixed or plug flow assumptions could be found by numerically integrating Equations 2.16 and 2.17a, respectively, from time equal to zero to the ONC time that was experimentally measured for a specific temperature and hole size combination.

However, when applying the lumped model to the GT-MHR geometry, the ONC time, and thus the upper end bound on the integration of Equations 2.16 and 2.17b, are unknown. Therefore, rather than the bounds of integration being determined by experimental values, for calculations involving the reactor geometry the numerical integration of the molar fraction

ODE's was performed from from time t_0 to some point in time t_{ONC} at which point $X = X_{ONC}$. That is, instead end bounds of the integration being specified in time, the bounds of integration were specified in terms of a mole fraction, X_{ONC}.

To accomplish this, a shooting method was employed to solve for the time $t\left(\bar{X}_L = X_{ONC}\right)$; i.e. the time at which $\bar{X}_L$ becomes equal to the defined ONC molar fraction X_{ONC}. For the mixed flow model, in which $\bar{X} = \bar{X}_L$at all times due to its perfect mixing, this simply required that the bounds of integration for Equation 2.16 be iterated until $\bar{X}_L = X_{ONC}$ at t_{ONC}. For the plug flow model however, in which $\bar{X}_L \neq \bar{X}$ at any time other than t_0, an additional outer iteration loop was needed. First, Equation 2.17a was numerically integrated as previously described so that $v\,(t)$ could be obtained. Then, using the velocity profile obtained from the integration of Equation 2.17a, Equation 2.17b was integrated to calculate $\bar{X}_L\,(t_{ONC})$. This process was repeated until a value of t_{ONC} fulfilled the criteria $\bar{X}_L\,(t_{ONC}) = X_{ONC}$.

2.4.2.4 Ratio of temporal scales

$$\frac{\text{Diffusion Time Scale}}{\text{Hole Time Scale}} = \frac{\tau_D}{\tau_h} \tag{2.20}$$

The ratio of the temporal scales for diffusion and the upper head hole forms a dimensionless parameter that can be used to quantify the relative magnitude of the effect of the upper head hole on the ONC time to that of the diffusive flux. For both the reactor and experimental geometries, as the value ratio of τ_D/τ_h grows, so does the relative importance of the effect of the hole as compared to that of the diffusion in determining the ONC time of the system. For the purposes of this study, a τ_D/τ_h value of unity is used as the benchmark for when the effect of the leak at the top of the system needs to be considered when calculating predicted ONC time.

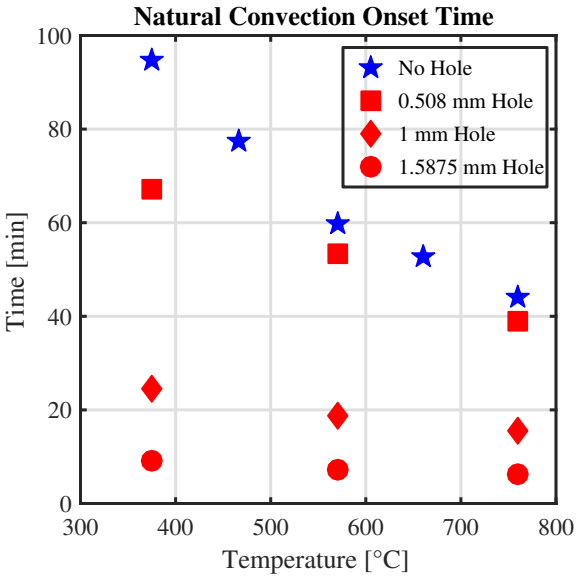

Figure 2.18: *ONC time vs temperature for various hole sizes*

2.4.3 Experimental Results and Analysis

2.4.3.1 Application of models to experimental results

In Figure 2.18, the ONC times observed for each tested hole size are plotted alongside previously published results [9] in which opening C was fully sealed throughout the experiment. For all temperatures and hole sizes, the experimentally determined ONC times were repeatable to within 15 seconds or less.

For a given hole size, the relative effect of the hole on the ONC time was inversely correlated with temperature. As the size of the hole increases, the rate at which helium is leaked through opening C continues growing larger, eventually almost negating any temperature-induced differences in the rate of diffusive mass flow out of openings A and B.

Table 2.5 presents the ratio τ_D/τ_h as calculated for each tested hole size and temperature in the experimental setup for both the plug flow and mixed flow scenarios. The calculated values of τ_D/τ_h appear to correspond well to their respective data points in Figure 2.18. Additionally, the hole time scale itself proved to be a very good predictor of ONC time for the cases where the effect of the hole was most dominant, as can be seen in Table 2.4.

For any given temperature, the magnitude of the difference between the ONC times of

τ_h/t_{ONC}	Temperature [K]	Hole Size [m]		
		.0005 m	.001 m	.0015875 m
Plug Flow	375 K	4.17	1.53	1.09
	575 K	4.44	1.64	1.13
	760 K	5.35	1.73	1.17
Mixed Flow	375 K	4.72	1.83	1.60
	575 K	5.20	2.00	1.68
	760 K	6.54	2.14	1.77

Table 2.4: *Ratio of hole time scale to measured ONC time*

τ_D/τ_h	Temperature [K]	Hole Size [m]		
		.0005 m	.001 m	.0015875 m
Plug Flow	375 K	0.676	5.10	19.4
	575 K	0.592	4.68	17.4
	760 K	0.542	4.21	15.6
Mixed Flow	375 K	0.618	4.42	13.7
	575 K	0.524	3.99	12.1
	760 K	0.459	3.54	10.7

Table 2.5: τ_D/τ_h *ratio calculated for experimental system*

the tests with a hole and that without uniformly increases with increasing τ_D/τ_h. It is also clear that, although it is not possible to define a precise, singular value for τ_D/τ_h at which the effect of the hole becomes relevant under all conditions, assuming a value of unity to be the approximate inflection point appears entirely appropriate. Regardless of the assumed level of mixing, the ONC times for all tests resulting in ratio values greater than unity are seen to be almost entirely determined by the effect of the hole, while those tests with τ_D/τ_h values less than on have ONC times that approach that of the no-leak, diffusion only values.

2.4.3.2 Effect of mixing assumption on calculated τ_D/τ_h

Although the values of τ_D/τ_h calculated using both the plug flow and mixed flow models appear to follow the same trends, in every case the time scale ratio calculated assuming plug flow was uniformly larger than the corresponding mixed flow value. Two factors were responsible for this trend. Figures 2.19 and 2.20, respectively, show the calculated $v\,(t)$ and $\bar{X}\,(t)$ curves over time for both the mixed and plug flow scenarios. While the respective velocity and mole fraction curves of the plug and mixed flow are mostly quite similar, two differences should

be noted. First, the minimum velocity calculated to have flown through the two larger holes was significantly lower under the plug flow assumption than it was under the mixed flow assumption. As the plug flow model assumes that flow through the upper hole is always pure helium, the viscosity and density used to calculate Re are those of helium. In contrast, for the fully mixed model, the – and thus the fluid properties – of the exit fluid varies over time as the system's average helium mole fraction changes. Thus, although both models start off experiencing equal viscous effects, over time the viscous losses experienced by the mixed model decrease, while for the plug flow model they do not. Correspondingly, the amount of helium calculated as removed from the system by the upper hole is noticeably reduced for several of the tests when using the plug flow, rather than mixed flow, assumptions.

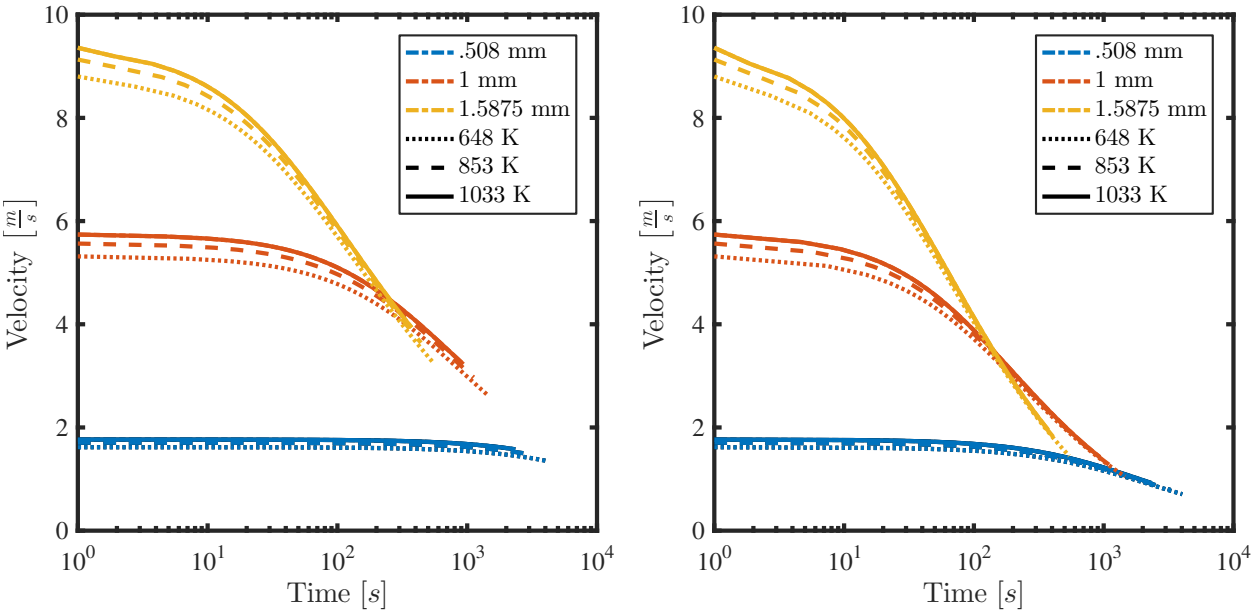

(a) *Mixed Flow* **(b)** *Plug Flow*

Figure 2.19: *Calculated $v\,(t)$ for experimental setup.*

However, these frictional differences between the plug and mixed flow model explain a negligible amount of the variance in each model's calculation τ_D/τ_h . Although the viscous differences will change the value of $\bar{j}$ calculated by each model, the slightly different values of molar flux do not substantially affect the calculated τ_D/τ_h . Rather, as was previously mentioned in section 2.4.2.3, the individual model's differing reported values of τ_D/τ_h is again primarily due to the the different molar capacities, CV , used in each model to calculate

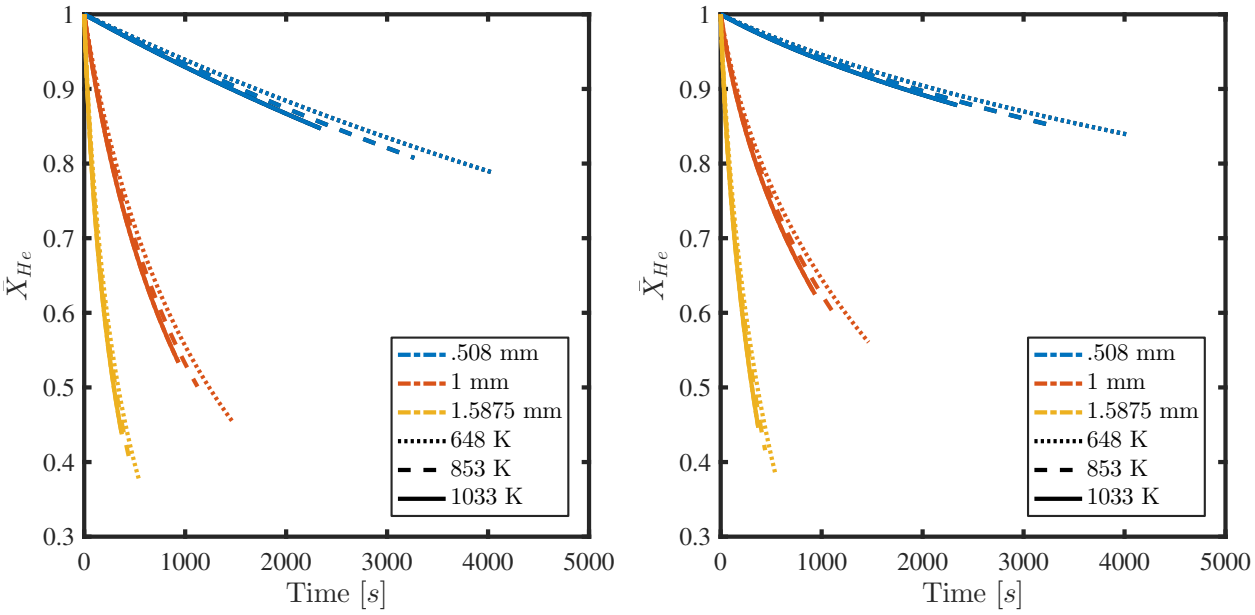

(a) *Mixed Flow* **(b)** *Plug Flow*

Figure 2.20: *Calculated $\bar{X}(t)$ for experimental setup.*

the hole time scale of Equation 2.9. That is, although the mixed flow model results in lower viscous losses and therefore is able to remove more helium from the system in a given time, the plug flow model has to remove less helium overall for ONC to be achieved for the reasons stated at the end of Section 2.4.2.3. Importantly, although this holds true even for the experimental setup used here, the effect of the difference in characteristic molar capacities is *much* larger for the geometry of the GT-MHR. Whereas the upper volume in the experimental apparatus makes up only about 30% of the total system volume, the upper fluid volume estimate used for the GTMHR here is 81% of the total fluid volume. Thus, the $v(t)$ and $\bar{X}(t)$ for a given hole size and temperature as calculated by the mixed and plug flow model can be assumed to be negligibly different for all the GTMHR results presented here.

2.4.3.3 Application of model to GT-MHR geometry

Figure 2.21 plots the upper head hole size that would be required for the ratio τ_D/τ_h to reach unity for each of the posited mixing scenarios over a range of hot leg temperatures. Also plotted as lines across both Figure 2.21a and 2.21b are the diameters of an instrumentation

penetration and the hole size defined as an anticipated operational event of the GT-MHR. That is, it is expected that even *without* undergoing the effects of some external event that, sometime during the life of the reactor, a the pressure vessel will be penetrated by a hole of the AOO-5 size. Figure 2.21a assumes that ONC were to occur when the mole fraction of helium in the lower volume of the reactor dropped to 5% while Figure 2.21b assumes ONC would occur when the composition dropped below 25% helium. Importantly, Figure 2.21 shows that regardless of the amount of interior mixing and for any reasonable ONC mass fraction, the effect of an upper head hole of the size specified as Anticipated Operational Event – 5 (AOO-5) for the MHTGR is likely to be vastly more important than any diffusive effects over the vast majority of the entire expected temperature range. Additionally, even the break of a smaller instrumentation penetration is likely to significantly impact ONC time if mixing within the system turns out to be limited.

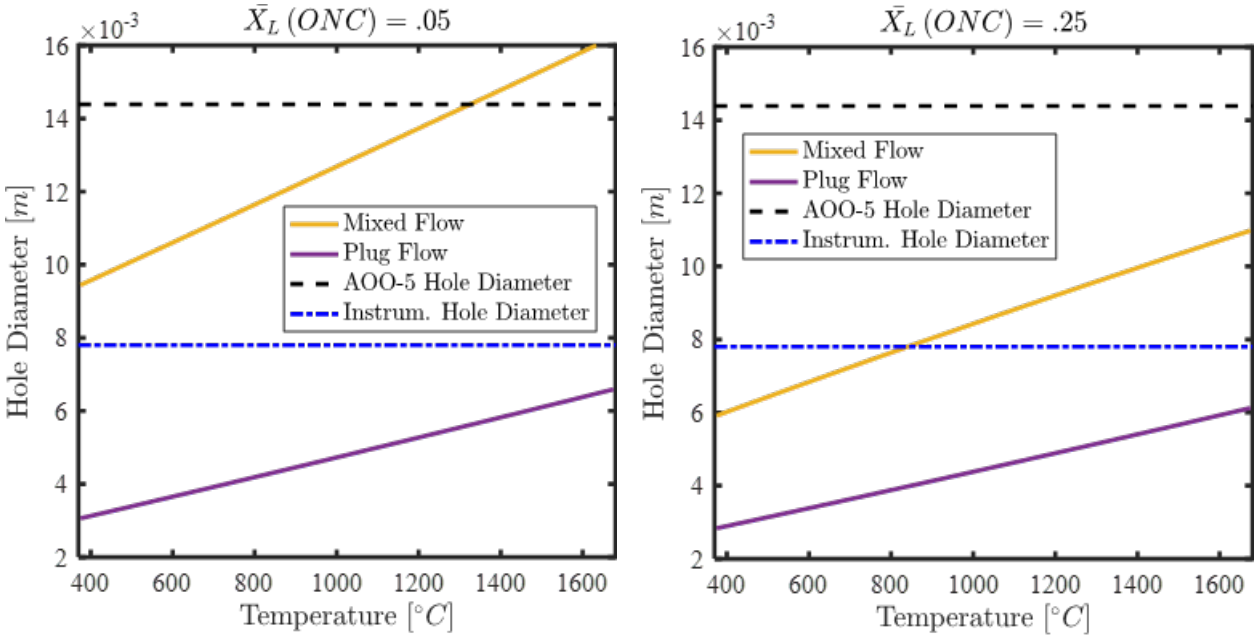

(a) $\bar{X}_L\,(ONC) = .05$ **(b)** $\bar{X}_L\,(ONC) = .25$

Figure 2.21: *Hole size required for leak to dominate diffusion as a function of core temperature*

Finally, Figure 2.22 shows the effect of changing the ONC criteria on the hole size required for the mixed flow model to meet two different thresholds. Each calculation plotted in Figure 2.22 was done for a hot leg temperature of 760 $°C$. The resulting trend shown in Figure 2.22

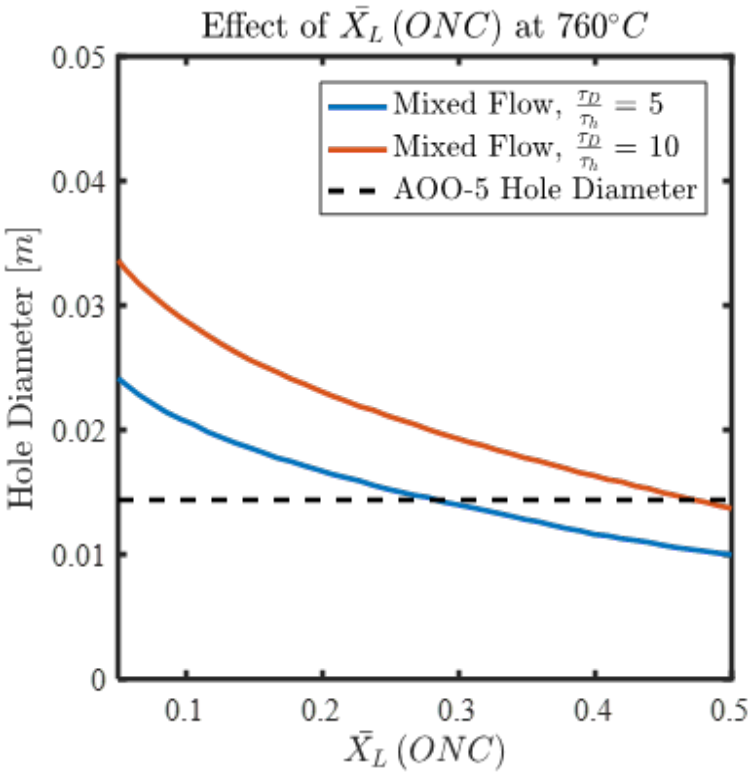

Figure 2.22: *Effect of helium fraction at ONC on effective hole size*

matches that observed when comparing Figures 2.21a and 2.21b. Physically, larger values of $\bar{X}\,(ONC)$ would correspond to geometries with lower amounts of internal mixing, higher temperature differentials between the legs, and lower overall loop flow resistance.

2.5 Conclusions

Air-ingress after depressurization under an inlet-outlet duct break is one of significantly important postulated scenarios under safety analysis of HTGRs. Previous experimental tests conducted at JAERI used 'inverse U' shaped setup to study transition from molecular diffusion to natural circulation. A new 'h' shaped setup was designed and developed in this study to understand the effect of upper unheated leg. In contrast to previous non-oxidizing studies, where Nitrogen was used as the gas present in external cavity, the present study was conducted with ambient air. Although both experimental studies have consistently shown that high temperature leads to earlier ONC, there were some clear differences in quantitative comparisons. The ratio of the diffusion time constant to ONC time, $\frac{\tau}{t}$, for the current study is found to be consistently lower than previous reports for the same corresponding test temperatures. This behavior can be attributed to the presence of this extended leg which increases the ONC time as it acts as an additional source of helium reservoir which leads to downward diffusion of helium.

As the hot leg temperature was increased, the ratio $\frac{\tau}{t}$ increased because of the greater role of natural convection currents. The experimental data on ONC times reported here will also be useful for understanding and validating future computer models. In the future, graphite test blocks will be placed in the high temperature helium tube to better understand the effect of the gaseous products resulting from graphite oxidation on ONC behavior.

A CFD simulation of the experiment was developed with the commercial code ANSYS CFX with the goal of predicting the experimentally observed ONC times. There was a good agreement between the CFD-predicted and experimentally measured ONC times; the predicted ONC times fell within 4% of actual values. Post-ONC velocity predictions also matched well with the experimental measurements.

To reiterate, the goal of the second part of this work was to find the minimum size of an upper head hole that would result in the effects of the helium loss through the hole to be the dominant factor in the determination of the onset of natural convection time following a loss of coolant accident due to a break in the main coolant pipe. In this work, the effect of a leak

in the upper head of an HTGR reactor occurring during such an accident was experimentally modeled and an analytical model was created to scale the results from the experiments to the GT-MHR geometry. To compensate for the inability to precisely predict the amount internal mixing that would take place in the complex geometry of an HTGR after the main coolant pipe break, two lumped parameter models were created to analyse the limiting cases of either perfect, or negligible, molecular mixing withing the geometries of interest.

The addition of the simulated upper reactor head breach was experimentally shown to significantly reduce the amount of time from the simulated main coolant pipe break to the onset of natural convection. Using the τ_D/τ_h ratio to scale the effects of the hole from the experiment to the reactor indicates that not only would a upper head hole of the benchmark AOO-5 hole size likely significantly decrease ONC time, but that under certain circumstances, so also would the break of an instrumentation penetration. If the amount of mixing is minimal, the hole size required to dominate – much less match – the effects of diffusion falls far below the AOO-5 benchmark. Given that the reactor is expected to, at some point within its operational life, incur an AOO-5 size hole *without* an external event, it seems highly prudent to plan for such a hole being created or enlarged by the same external event that causes a rupture of the main coolant channel.

Acknowledgments

This work was supported in part by the U.S. Department of Energy, Office of Nuclear Energy, under Award Number DE-NE0008412.

Bibliography

[1] Tetsuaki Takeda and Makoto Hishida. Studies on diffusion and natural convection of two-component gases. *Nuclear Engineering and Design*, 135(3):341–354, 1992. DOI: 10.1016/0029-5493(92)90201-6.

[2] Tetsuaki Takeda and Makoto Hishida. Studies on molecular diffusion and natural convection of multi-component gases. In volume 135, pages 1489–1497, 1993.

[3] Tetsuaki Takeda and Makoto Hishida. Studies on molecular diffusion and natural convection in a multicomponent gas system. *International Journal of Heat and Mass Transfer*, 39(3):527–536, 1996. ISSN: 00179310. DOI: 10.1016/0017-9310(95)00148-3.

[4] Tieliang Zhai. *LOCA and Air Ingress Accident Analysis of a Pebble Bed Reactor*. PhD thesis, Massachusetts Institute of Technology, 2003.

[5] Andrew C Kadak and Tieliang Zhai. Air ingress benchmarking with computational fluid dynamics analysis. *Nuclear Engineering and Design*, 236(October 2004):587–602, 2006. DOI: 10.1016/j.nucengdes.2005.11.019.

[6] Richard R Schult, Paul D Bayless, Richard W Johnson, James R Wolf, and Brian Woods. Scaling Studies for High Temperature Test Facility and Modular High Temperature Gas-Cooled Reactor. Technical report, Idaho National Laboratory (INL), 2012.

[7] Chang H Oh, Eung S Kim, Hee C No, and Nam Z Cho. Final Report on Experimental Validation of Stratified Flow Phenomena, Graphite Oxidation, and Mitigation Strategies of Air Ingress Accidents. Technical report, Idaho National Laboratory (INL), 2011.

[8] N Kodochigov, Yu Sukharev, E Marova, N Ponomarev-Stepnoy, E Glushkov, and P Fomichenko. Neutronic features of the gt-mhr reactor. *Nuclear Engineering and Design*, 222(2):161–171, 2003.

[9] Daniel Gould, Daniel Franken, Hitesh Bindra, and Masahiro Kawaji. Transition from molecular diffusion to natural circulation mode air-ingress in high temperature helium loop. *Annals of Nuclear Energy*, 107:103–109, 2017. ISSN: 0306-4549. DOI: 10.1016/j.anucene.2017.03.049.

[10] James R Welty, Charles E Wicks, and Robert E Wilson. *Fundamentals of Momentum, Heat, and Mass Transfer*. Wiley, New York, 3rd edition, 1984, page 487. ISBN: 0471874973.

[11] Charles R Wilke. Diffusional properties of multicomponent gases. *Chemical Engineering Progress*, 46(2):95–104, 1950.

[12] Daniel Franken, Daniel Gould, Prashant K. Jain, and Hitesh Bindra. Numerical study of air ingress transition to natural circulation in a high temperature helium loop. *Annals of Nuclear Energy*, 111:371–378, 2018. ISSN: 0306-4549. DOI: 10.1016/j.anucene.2017.09.007. URL: http://www.sciencedirect.com/science/article/pii/S030645491730275X.

[13] Stone & Webster Engineering Corp. MHTGR PSID. Technical report, Department of Energy, 1987.

[14] H. G. Olson, H. L. Brey, F. E. Swart, and F. M. Mathie. The Fort St. Vrain High Temperature Gas-Cooled Reactor XI Control rod drive and orifice assemblies. *Nuclear Engineering and Design*, 61:323–329, 1980.

[15] Richard R Schultz, Paul D Bayless, Brian D Hawkes, Richard W Johnson, and James R Wolf. Scaling Studies for High Temperature Test Facility and Modular High Temperature Gas-Cooled Reactor. Technical report February, Idaho National Laboratory, Idaho Falls, 2012.

[16] J.N. N Reyes, J.T. T Groome, B.G. G Woods, B. Jackson, and T.D. D Marshall. Scaling analysis for the high temperature Gas Reactor Test Section (GRTS). *Nuclear Engineering and Design*, 240(2):397–404, 2010. ISSN: 00295493. DOI: 10.1016/j.

nucengdes.2009.03.020. URL: http://linkinghub.elsevier.com/retrieve/pii/S0029549309001794.

[17] Chang H Oh and Eung S Kim. Air-ingress analysis: Part 1. Theoretical approach. *Nucl. Eng. Des.*, 241(1):203–212, 2011. ISSN: 00295493. DOI: 10.1016/j.nucengdes.2010.05.064.

[18] Novak Zuber, Gary E Wilson, Mamoru Ishii, Wolfgang Wulff, and B E Boyack. An integrated structure and scaling methodology for severe accident technical issue resolution : Development of methodology. *Nuclear Engineering and Design*, 186:1–21, 1998.

[19] Chang H Oh, Hyung S Kang, and Eung S Kim. Air-ingress analysis: Part 2 Computational fluid dynamic models. *Nuclear Engineering and Design*, 241(1):213–225, 2011. ISSN: 0029-5493. DOI: 10.1016/j.nucengdes.2010.05.065. URL: http://www.sciencedirect.com/science/article/pii/S0029549310004127.

Chapter 3

The Effects of Oxidation on Graphite

3.1 Introduction

The potential of graphite – even nuclear grade graphite – to undergo oxidation if exposed to atmospheric air at high temperatures has long a concern for graphite moderated reactors[1]. Schweitzer and Singer first experimentally investigated the effects of air flow and temperature on the oxidation process of nuclear graphite and determined reaction rates and equilibrium temperatures for an early reactor-grade graphite in an attempt to determine the conditions required for a self-sustaining oxidation reaction to occur [2–4]. Since then a great deal of work has been done to characterize the oxidation rate and kinetic parameters of numerous different grades of graphite under a wide range of temperatures and air flow rates. Lee et. al [5] experimentally characterized the oxidation behavior of two modern nuclear graphite thermogravimetrically. The transient oxidation behavior of several grades of nuclear graphite when exposed a smooth flow of highly purified, dry air of was reported by Chi et. al [6]. A comprehensive model for the oxidation of graphite oxidation was proposed by El-Genk et. al [7] and validated for several different grades of nuclear graphite.

However, all of this work has been done in laboratory environments with single-effects experiments. There has been far less work done on whether the conditions and flow patterns present in a reactor both before and after ONC can be fully represented by the previous oxidation experiments conducted with forced convective flows. For example, although Takeda and Hishida [8] found that the ONC time was not substantially influenced when the effects of graphite oxidation were included in the system, they also found that the flow rate of oxidizing gas into the system varied over time prior to ONC. As part of an effort to develop and validate computer codes for future HTGR designs, Oh et. al performed a comprehensive analysis of the ONC phenomenon and graphite oxidation [9]. Again however, the ONC and oxidation physics were analyzed separately and only the effects of fully developed, constant flow rate, forced convective flows were examined.

Additionally, potential changes to the thermal properties of any graphite left behind following an oxidizing flow have not been thoroughly examined. Although it has been shown by researchers such as Snead et. al [10] that neutron irradiation, which also causes damage

to the graphite crystalline structure [11], can significantly change graphite's thermal conductivity and structural strength, the effect that oxidation has on its thermal properties – in particular graphite's thermal diffusivity and emissivity – has not been well established.

Thus, the goals of this work are twofold. First, to capture the mixed effects of air ingress and graphite oxidation to investigate any role played by varied flow conditions on reaction kinetics. And second, to identify and measure any changes in the graphite's thermal properties due to the oxidation process. The remainder of this chapter provides details of two sets of experimental studies that were were performed to accomplish these goals, as well as analysis of the results from said experiments.

3.2 Axial Flow Experiments irradiation

Experiments in which an air flow was induced through a heated, representative graphite flow channel were performed with both forced and natural convection driven flows. For the forced convection tests, air flow rates of 15, 25, and 30 SLM were used. For the natural convection test, the flow velocity was similar to that of the injected air previously measured in 2.2.1.4 and plotted in Figure 2.15. This velocity of $0.20\,\mathrm{m\,s^{-1}}$ translates to an approximate volumetric flow rate of 20 SLM air. After the test pieces were oxidized, samples from each piece were also used to measure the effect of oxidation on the thermal diffusivity and emissivity of graphite.

3.2.1 Experimental Design

The aforementioned experiments were designed to obtain measurements of thermal diffusivity, crystal structure, and surface roughness form samples of annular graphite test pieces that were exposed to defined environmental conditions and experienced a quantifiable amount of oxidation. The samples were analyzed after the experiment was finished and thus the measurements performed on each sample were representative of the total integrated effect that the oxidation had on a specific annular graphite test piece. Environmental conditions, on the

other hand, were measured using in-situ methods and were obtained throughout the entire course of each experiment.

3.2.1.1 Environmental Measurements

Throughout each experiment, measurements of the furnace temperature, room humidity, fluid flow rate, and oxygen content of exiting flow were taken. Furnace temperature was measured with 3 k-type thermocouples. The temperatures reported from the thermocouples were both recorded and used as inputs for the PID controllers controlling the power to each of the three furnaces used to heat the sample. In each of the forced flow experiments, flow rate was measured and controlled using a thermal mass flow controller (Figure 3.3). To quantify the amount of oxidation experienced by each test piece, the flow exiting each annular test piece was sampled and tested for oxygen content during all periods of bulk flow. In the cases of the forced flow experiments, the data from this measurement allowed for the total amount of oxygen consumed by the oxidation reaction to be calculated. Further information on each of these measurements can be found in Section 3.2.2.

3.2.1.2 Post Experiment Measurements

After each experiment was preformed, several further measurements were taken on the tested cylinders and their representative samples. First, the total mass of each cylinder was measured post-run and recorded to allow better quantification of the oxidation endured by each test piece. Second, samples from each tested annular graphite cylinder were subjected to tests to determine the change in the graphite's thermal properties. Thermal diffusivity was measured using the laser flash method. This state of the art method is detailed in Section 3.2.4.2. To provide better understanding of the causes of any change in a sample's thermal properties, each sample was also subjected to a x-ray diffraction test to determine if any significant changes to the graphite's crystal structure had occurred. Although other methods – such as Raman Scatter Analysis – of determining and quantifying the exact crystal structure of graphite exist, our goal was merely to determine if the crystal structure of the

tested pieces had substantially changed in any way. Thus, the XRD analysis was wholly sufficient.

Finally, the surface roughness of selected samples was tested using a needle profilometer. Information on the impact of oxidation on graphite's surface roughness was desired for two reasons. First, surface roughness is a major factor in the emissivity of an object and the magnitude of the change in roughness caused by oxidation was desired for the analyses performed on the experimental data reported in Section 3.3. Secondly, as surface roughness also plays a large role in determining thermal contact resistance, measurements of average surface roughness and slope were needed to calculate the value of thermal contact resistance between oxidized spheres used in the finite elements model of Chapter 5. Once again, although other, possibly more exacting methods of measuring surface roughness parameters exist, the needle profilometer was of sufficient resolution and accuracy to achieve our goals while also being readily available for use.

3.2.2 Experimental Setup

The basic experimental setup used in this study is the same as the apparatus described in Section 2.2.1. A diagram of the setup is shown in Figure 3.1a. Annular test pieces were inserted into the apparatus from below the left leg and supported via a smaller 42mm OD by 45mm ID quartz tube. This tube in turn was supported by a custom flange assembly. This flange assembly, that can be seen at the bottom of Figure 3.1b, was created by welding a steel washer with a 40mm ID between 2 KF 50 flanges.

After the test piece and the supporting quartz tube were inserted into the assembly, the KF 50 flange nearest the test piece was clamped to another such flange at the base of the left leg of the quartz h-tube, while the other end of the welded assembly was attached to other KF style parts that allowed flow connections to be made. Below all this was either a steel blank flange, or a custom made, LWIR transparent, window that also acted as a cover for the final KF 50 connection below the left leg. The zinc-selenide window was used for the experiments detailed later in 3.3. This addition both sealed the apparatus and allowed for

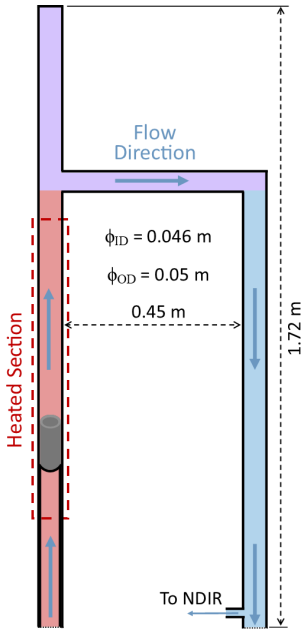

(a) *Diagram of experimental setup.*

(b) *The test piece on the supporting quartz tube and its supporting flange assembly.*

Figure 3.1: *Experimental setup for oxidation testing*

an IR camera to be used to view the test piece's lower face during an experiment.

Connections for fluid flow were placed at the lowest regions of both legs, below the quartz h-tube. These KF50-NPT tees were placed below the left and right legs and used to inject and remove gasses, respectively. Depending on the experiment, a combination of air, helium and oxygen were connected to the left leg. The helium and oxygen gasses used in the experiments were of the Matheson Ultra High Purity grade. Air injected into the assembly consisted of atmospheric air, pressurized using an oil free compressor. During air injection experiments, the injected air had a relative humidity of about 50%.

For the forced convection experiments, flow control was maintained using thermal mass flow controllers, such as that shown in Figure 3.3. The mass flow controllers were controlled and read using standard analog 0 V to 5 V signals. These signals were generated and read by a LabJack T7 DAC, control of which in turn accomplished using its Matlab API.

On the lower right leg of the experimental setup were connections for exhausting, evacuating, and sampling the gas with the system. One opening was connected to a ball valve

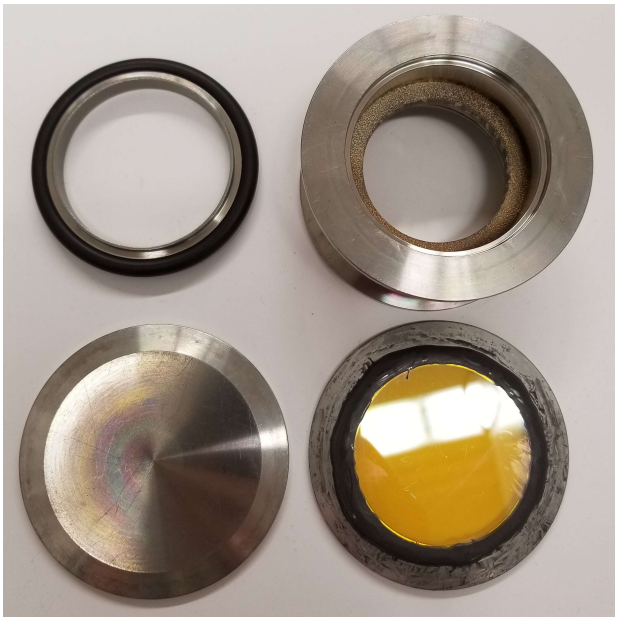

(a) *Clockwise from top left: Centering ring, welded flange assembly, IR window, blank flange.*

(b) *A KF 50 tee attached to a leg of the experimental apparatus. It allows fluid connections at the sides and a flange connection underneath.*

Figure 3.2: *Components used in lower legs of h-tube setup.*

and was used both to control the system pressure before an experiment, and as an exit for the flow during forced convection experiments. Gas samples were extracted from the setup's right leg using a small, brushless diaphragm pump. The sample flow rate was controlled via another thermal mass flow controller. Extracted sample gas was provided to the inlet of a Thermo-Fisher model 60i Non-Dispersive InfraRed (NDIR) analyzer at atmospheric pressure and a rate between 1.5–3.0 SLM. This unit was used to calculate the remaining oxygen content present in the gas flow after it had passed through the test piece.

The test pieces placed in this experimental apparatus consisted of annular cylinders of G-348 graphite. These cylinders had an inner diameter of 32.3 mm, an outer diameter of 45 mm, and lengths of 152.4 mm. G-348 is an fine grain isotropic graphite fabricated by cold hydro static pressure molding by Tokai Carbon. It is coal tar pitch coke – rather than petroleum – based and possess and average grain size of approximately 30 micron. It is most similar to the IG-430 grade of nuclear graphite. Both grades have similar grain sizes, use coal as their source coke, and are isostatically rather than vibration molded [6].

Figure 3.3: *A thermal mass flow controller used for flow injection with filter attached.*

3.2.3 Experimental Procedure

For the forced convection experiments, the procedure was as follows:

1. The G-348 test piece was inserted into the left leg of the quartz apparatus.
2. Valves were closed and covering flanges were attached to seal the system.
3. The system was evacuated to a rough vacuum and then back filled with helium.
4. The tube furnaces surrounding the test piece were turned on and the sample was heated to a steady state temperature of 900 °C. System pressure was maintained at close to atmospheric throughout this process by using an exhaust valve to let excess helium escape as needed.
5. After steady state conditions had been achieved, the ball valve attached to the lower right leg was opened. Immediately following this, the DAQ was commanded to send the proper voltage signals to the mass flow controllers and power supply, beginning bulk flow and providing power to the sampling pump.
6. Flow was continued for 90 minutes. During this time, temperature, mass flow rate, and oxygen content data were continuously collected.

7. At 90 minutes, bulk flow was stopped and the system was sealed, evacuated, and cooled.

For the tests involving natural convection driven flow, several steps of the procedure were modified. Steps 1 through 4 from the forced convection experiments were again performed. After this, however, additional steps were required to account for the fact that, unlike the forced convection experiments, bulk flow would not immediately begin due to the buoyancy effects discussed in Chapter 2. Due to the quantity of fluid needed by the NDIR, gas sampling could not begin until after ONC without affecting the results. Therefore, an IR camera was used in the manner previously described in Section 2.2.1 to detect the moment of ONC. The new steps taken for the natural convection oxidation experiments are as follows.

5a After steady state conditions were achieved, the flanges (see Figure 3.2a) covering the lower openings of both the right and left legs of the apparatus were removed. Monitoring of the temperature of the upper right corner of the quartz apparatus (identified in Figure 2.1a) was begun by an IR camera.

6a When ONC was detected, signals were sent to the sample pump's power supply and the sample line mass flow controller to begin extracting gas.

7a Sampling was continued for 90 minutes. During this time, temperature and oxygen content data were continuously collected.

8a At 90 minutes past ONC, the flanges were reattached to the openings of the lower legs and the system was sealed, evacuated, and let cool.

3.2.4 Results and Analysis - Axial Flow Experiments

Before and after images of the entrance and exit regions, respectively, of the graphite cylinders used in the 15 SLM forced convection test are shown in Figures 3.4a and 3.4b. The amount of mass lost to oxidation was large enough to measurably reduce both the length and thickness of the tested cylinder with the thickness of the exit region deceasing less than

	Flow Rate			
	15 SLM	**25 SLM**	**30 SLM**	**NC**
Initial Mass [g]	221	220.1	220.5	220.3
Mass Change [g]	55.6	65.7	73.2	69.2
Mean $^{P_{CO}}/_{P_{CO_2}}$	0.226	0.227	0.221	~
Entrance $\mathbf{Re_D}$	529	881	1058	~

Table 3.1: *Data from oxidation tests. Each flow rate corresponds to a specific experiment and test piece.*

that of the entrance region in all cases. As the temperature of the exit region of a test piece during oxidizing flow will always be higher than that of the entrance region due to the spatial differences in fluid temperature, the reduced erosion seen at the exit regions of the tested graphite samples indicates that the oxidation rate throughout the cylinder is impacted by spatial variations in fluid flow. The reaction rate for each test was calculated as an average for the entire sample per unit of exposed surface area. The surface area value used to calculate the reaction rate of the G-348 graphite was obtained by averaging the before and after oxidation dimensions of the test piece.

(a) *Exit* **(b)** *Entrance*

Figure 3.4: *15 SLM test piece next to untested sample*

The ratio of carbon monoxide to carbon dioxide produced, $^{P_{CO}}/_{P_{CO_2}}$, by the oxidation process was calculated by comparing the amount of oxygen consumed by the process with the amount of mass lost from the graphite sample. The total quantity of O_2 used was

found by comparing the amount of oxygen leaving the system with the amount put in. The volumetric percentage of oxygen leaving the system was measured continuously using the electro-chemical sensor attached to the NDIR throughout the duration of bulk flow in each experiment. This measurement is plotted in Figure 3.5b for each test. It should be noted that, in the case of the natural convection curve, the first 43.07 minutes of the test prior to ONC were excluded from the plot as no sampling was preformed during that time.

For each forced convection run, the total amount of O_2 leaving the system was found by multiplying the oxygen percent measurement with the flow rate measured by the MFC and then integrating the result over the duration of the experiment. For the natural convection run, no precise measurement of flow rate was available, and thus neither the entrance Reynolds number nor the average $^{P_{CO}}/_{P_{CO_2}}$ are reported for this run in Table 3.1. However, as the total mass lost during the natural convection run was found to be between that lost during the 25 SLM and 30 SLM tests, it is expected that the $^{P_{CO}}/_{P_{CO_2}}$for this run would fall in a similar range to those forced convection tests.

Oxidation rates per unit area are plotted in Figure 3.5a for each experiment. Due to the limited supply of graphite test pieces that were available to be used, experiments were conducted at only one temperature point, 900 °C. This temperature was chosen as it was high enough to induce significant amounts of oxidation and was close to the temperatures used in the experiments described in Chapters 2 and 4. The values obtained in this work are plotted against values previously reported for NBG-18 [12] and IG-110 graphites [13] and show reasonable agreement with Lee's results. The results from the forced convection experiments performed in this work show similar oxidation rates to the others previously published.

Importantly however, in the natural convection test there is some indication that either the pre-ONC environment conditions or the post-ONC buoyancy driven flow might be acting to enhance the oxidation rate beyond what would be expected for its (expected) 20 SLM-equivalent flow rate; the test piece from the natural convection test lost approximately 14% more mass than would have been predicted from the forced convection experimental data. However, better measurements of the precise post-ONC flow rate are likely needed before it

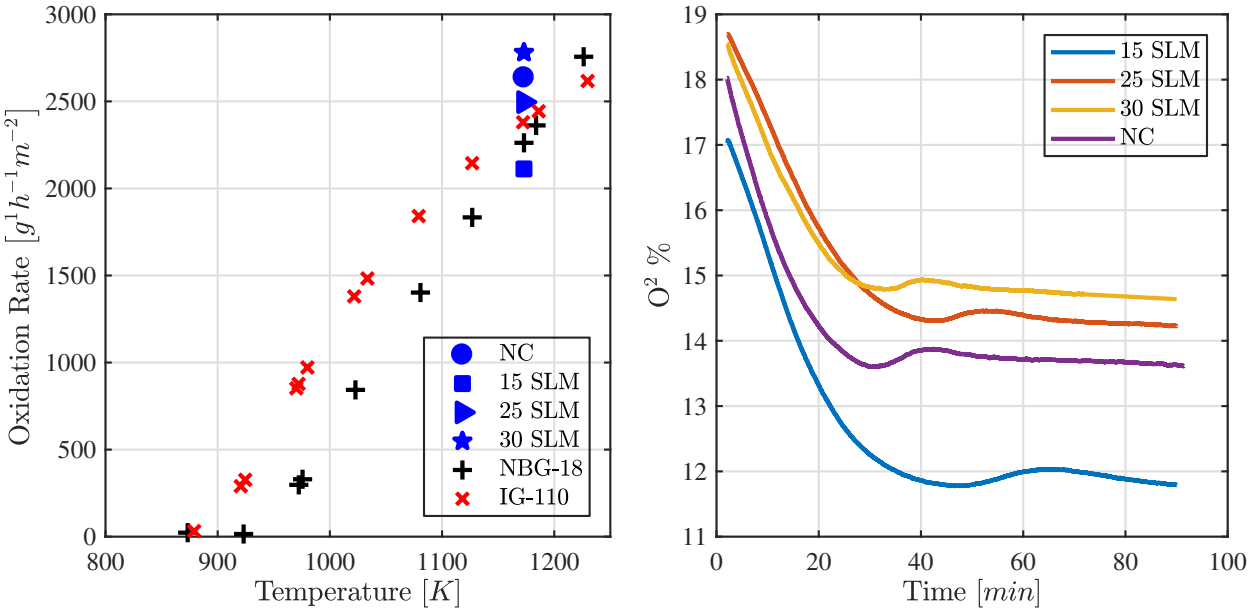

(a) *Oxidation rates per unit exposed area. Data plotted for NBG-18 and IG-110 graphite are obtained from Ref. [12] and Ref. [13], respectively.*

(b) *Percent O_2 remaining in flow.*

Figure 3.5: *Comparison of oxidation results*

can be conclusively said that that such effects are indeed occurring.

Further analysis of the oxidized graphite was performed using samples from the oxidized test pieces. Samples from both the natural convection test, as well as the 15, 25, 30 SLM forced convection experiments, were obtained from their corresponding test cylinders. The entrance regions of the graphite cylinders from each of these tests is shown next to that of an untested sample in Figure 3.6. In the figure, the locations from which the samples were removed can be identified from the holes seen in each of the tested cylinders. The extracted samples were 12.7 mm in diameter and machined to be less than 6 mm thick at their thickest point. Each sample was extracted using a plugging bit to drill into the side of the test cylinder before being milled on their un-oxidized, outer face to both provide a flat surface and to meat thickness requirements.

Figure 3.6: *Entrance region of G-348 test pieces. From left to right: un-oxidized sample, 15 SLM, 25 SLM, NC, 30 SLM*

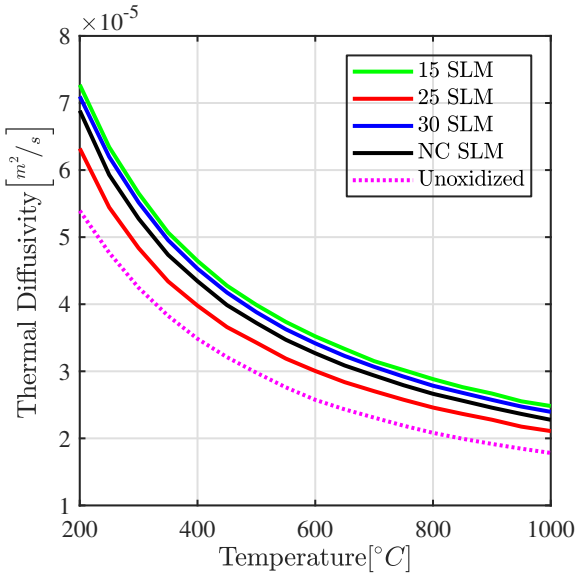

Figure 3.7: *Thermal diffusivity of samples from each test.*

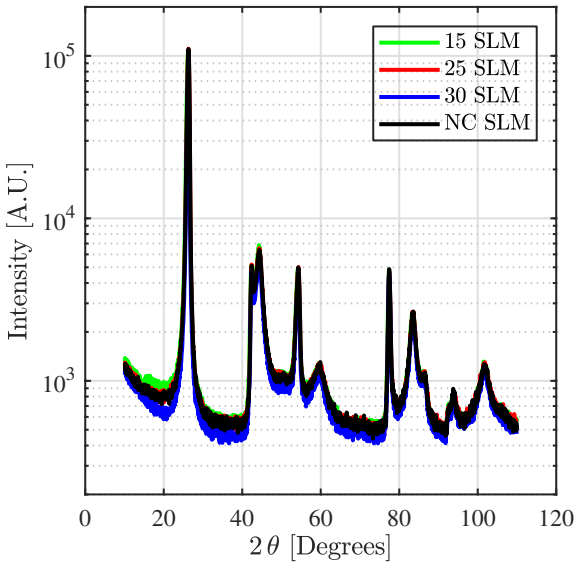

Figure 3.8: *XRD data from each tested sample.*

3.2.4.1 XRD

X-ray diffraction (XRD) analysis has been previously shown to be able to identify details a graphite's crystal structure, including details such as the degree of graphitization, crystalline size, inter-layer spacing, and anisotropy [11, 14, 15]. Several works have used this method for both virgin graphite and that which has been damaged by either irradiation or oxidation [16] [11]. The XRD analyses performed on the samples generated in this work (Figure 3.8), however, were not able to detect any crystal structure differences. As studies have shown differences when the bulk material was significantly changed due to neutron irradiation, it is assumed that the oxidation did not cause significant changes to the crystal structure.

3.2.4.2 Laser Flash Analysis

The flash method was developed by Parker et. al [17] as a method to quickly and accurately measure the thermal diffusivity of materials that would work at both moderate and high temperatures. The method is based upon being able to simulate an instantaneous change in temperature on a face of a test piece that can be accurately modeled as 1–D and perfectly insulated. Once the step change in temperature is applied to the front boundary of the test piece, the relative temperature change of the sample's opposite boundary is monitored until a maximum temperature is reached. The amount of time observed between the initial step change and the sample's rear face reaching it's maximum temperature is then recorded. Using this measurement in conjunction with the available analytical solution for the temperature of a 1–D object under these boundary conditions, the thermal diffusivity is able to be calculated. Importantly, this method does not require knowledge of the magnitude of the amount of energy instantaneously deposited onto the sample's front surface) for the thermal diffusivity of the sample to be obtained. Additionally, this method can be used to calculate the temperature dependence of a material's thermal diffusivity by simply preheating the sample material to different initial temperatures and repeating the test.

Although the method was originally defined to be used in conjunction with an arc image furnace, modern systems instead use a laser to deposit energy into the front face of the target

specimen. For this work, the LFA 467 laser flash system was used to measure the thermal diffusivity of each the samples taken from the tested graphite cylinders over a wide range of temperatures. Figure 3.7 shows the results obtained for each sample's thermal diffusivity over a temperature range of 200 °C to 1000 °C. In each case, the thermal diffusivity of the oxidized samples were shown to be greater than that of an un-oxidized control sample over the entire tested temperature range. This increase is assumed to be caused by the existence of an oxidation-induced porous layer on the face of the sample that originally faced the interior of the annular test piece.

Although the graphite sample's density will be directly affected by any porous layer formation, thermal conductivity is not expected to be significantly affected. Although the thermal conductivity of graphite is known to slightly decrease with increasing porosity, the density of the samples tested in this study did not decrease enough for this effect to be appreciable; only a surface layer of our test pieces showed significant oxidation and even for the least oxidation resistant graphite tested by J.J Lee the average porosity of the oxidized layers only every reached 25%, and for most grades was significantly less than this. In contrast, the thermal conductivity of 90 percent porous graphite foams is known to drop only 30%. Given the lack of any changes in the graphite sample's crystal structure as measured by the XRD analysis in Section 3.2.4.1, nor is any change in thermal conductivity likely to occur to due to changes in the graphite's structure. Thus, for the particular graphite samples tested in this study, it can be safely assumed that the oxidation process affected no significant change in their thermal conductivity. With this assumption, the average density of the porous layers of each test piece can be calculated by assuming that the oxidation layer thickness is similar to that found by J.J. Lee for NBG-18 graphite. These density values are then later used in modeling the heat transfer capabilities of a bed of oxidized graphite spheres in Chapter 5.

Surprisingly, the sample from the G-348 cylinder that underwent air flow of 15 SLM shows a higher increase in thermal diffusivity than observed for the 25 SLM, 30 SLM and NC samples despite the latter three samples being obtained from test pieces that lost far more mass due to oxidation. However, the interior furnace temperature during the 15 SLM test

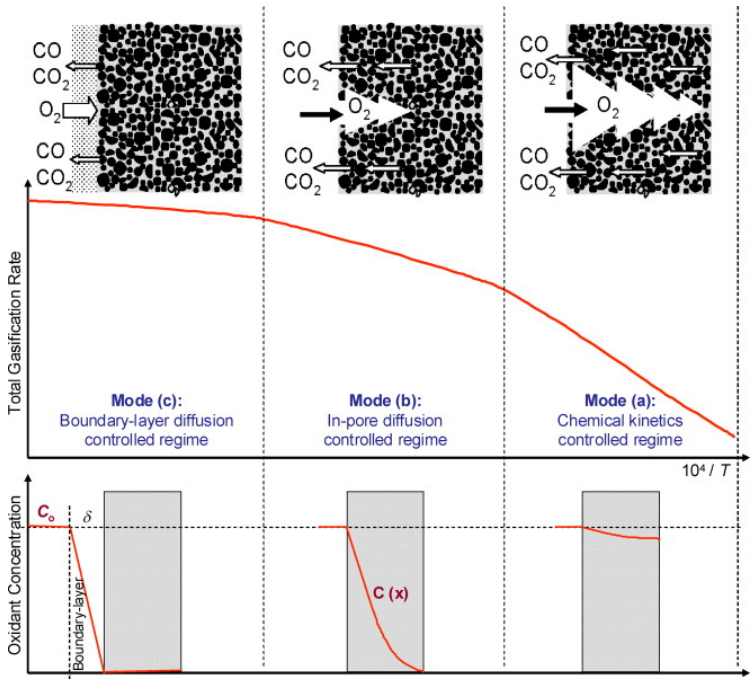

Figure 3.9: *Oxidation modes of porous nuclear graphite. Figure from Ref.[19].*

was measured to be 10 °C to 15 °C lower than that of the other three tests. It is also highly likely that the relative temperature difference between the average test piece temperature of that run and those with the higher flow rates is even greater than the 10 °C to 15 °C difference measured in the interior of the surrounding furnace. In certain temperature ranges, the rate and effect of graphite oxidation is known to be highly temperature dependent [18]. At lower temperatures, the rate of oxidation is low and has the effect of increasing the porosity affected graphite, without changing the graphite's outer dimensions. At higher temperatures, oxidation begins to occur only on the graphite surface. This results in little, if any, changes to the porosity of the graphite, but quite possibly in large changes to its outer dimensions.

The transition temperature at which the oxidation process can be said to move from regime to regime is very difficult to define and is known to vary between individual grades of graphite [12]. While no in-depth study has been done on the transition points of G-348, Se-Hwan Chi and Gen-Chan Kim found large, temperature-dependent differences in the transient oxidation kinetics between 808 °C to 911 °C for several different grades of graphite – including the similar IG-430 grade [6]. This indicates that at these temperatures the reaction is not immediately, fully Mode C (see Figure 3.9) and some amount of temperature

Figure 3.10: *Surface profile samples. Clockwise from top left: NC SLM 1, Control, Saw Cut, NC SLM 2*

dependence in the oxygen penetration depth still exists. Therefore, it is theorized that the lower temperature of the graphite cylinder during the 15 SLM test run enabled deeper penetration of oxygen into the cylindrical test piece and resulted in the sample taken from that test piece possessing a thicker porous layer than that from the higher flow rate tests.

3.2.4.3 Surface Roughness Changes

The effects of the oxidation process on the surface roughness of the tested graphite were examined by using a profilometer to quantify the surface roughness of several graphite samples cut from the test cylinders. The measured roughness of those samples that were analyzed with the profilometer are shown in Figure 3.10. Clockwise from top left, the samples in Figure 3.10 are denoted Control, Saw Cut, Oxidized 1, and Oxidized 2. The 'Control' and 'Saw Cut' samples are un-oxidized samples with differently machined surfaces, while the Oxidized 1 and Oxidized 2 pieces are taken from the entrance and exit of a test piece that had undergone significant oxidation. The measured surface of the 'Control' sample was faced with a 4 flute carbide end mill turning at approximately 3000 rpm. The control surface is

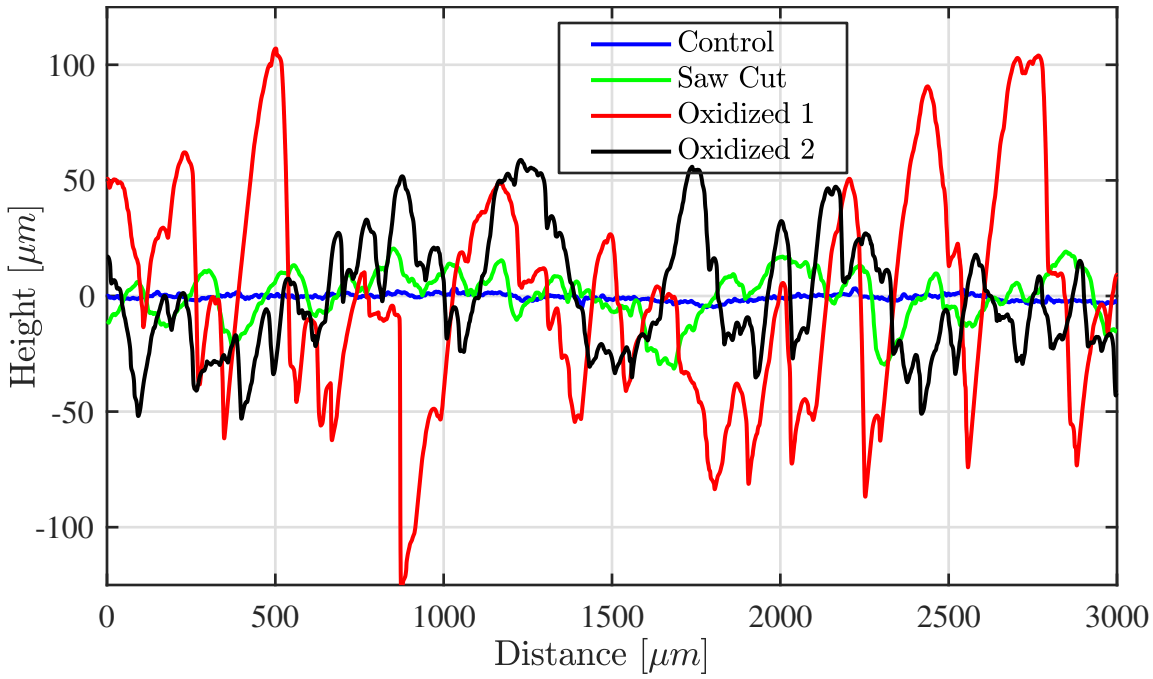

Figure 3.11: *Surface profiles of representative graphite samples*

most similar to the axial surfaces of the rods later described in Section 4.3. In contrast, the face of the large annular piece denoted 'Saw Cut' resulted from an annular cylinder being cut with a large band saw. This type of surface is the most representative of the average surface conditions present on the portions of un-oxidized graphite viewed by the IR camera. Finally, the two oxidized samples are representative of the damaged surfaces seen in Figures 3.15b, 3.6, and 3.4.

The roughness of each surface is quantitatively defined by the surface's average roughness, R_a and average slope, Δ_a. These values were calculated as defined in ASME B46.1 [20] and are shown in Table 3.2.

Previous work done analyzing graphite emissivity has indicated that the emissivity of certain grades graphite will rise as surface roughness, such as that caused by oxidation, in the SWIR and MWIR wavelengths [21]. This is also likely what caused the increase in emissivity in the LWIR region reported in Section 3.3.4. The increased roughness of the oxidized samples shown in Figure 3.15 is highly apparent compared to the 'Control' and 'Saw Cut' samples shown in Figure 3.10.

	$\mathbf{R_a}$ [m]	$\mathbf{\Delta}_a$
Control	1.56×10^{-6}	94.0×10^{-3}
Saw Cut	10.89×10^{-6}	263.2×10^{-3}
Oxidized 1	47.55×10^{-6}	1.024
Oxidized 2	25.84×10^{-6}	687.5×10^{-3}

Table 3.2: *Roughness parameters for each of the samples tested.*

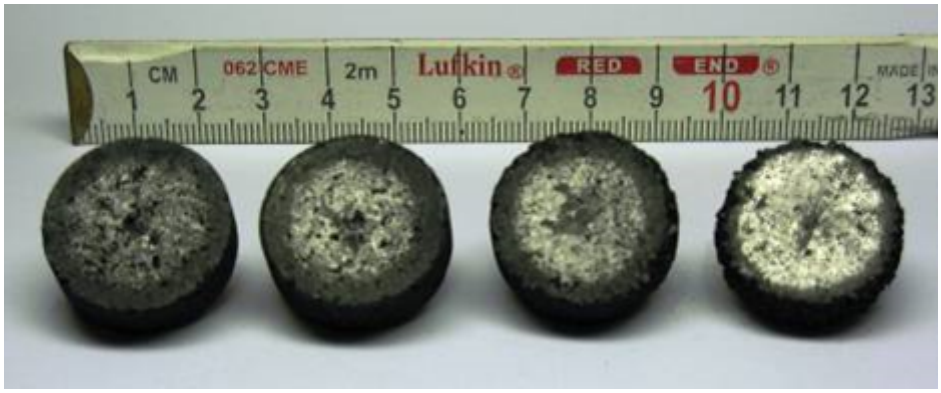

Figure 3.12: *Surface of graphite coupons exposed to a high temperature, oxidizing environment. The outer edges were not exposed due to the ceramic clamps used to hold the coupons. Figure from Ref.[22]*

3.3 Emissivity Experiments

3.3.1 Changes to Emissivity

Due to the HTGR's high operating temperatures and gas filled core, radiative heat transfer is likely to be significant in any accident scenario. Helium's low (in comparison to water) thermal conductivity and high transmissivity result in the potential for large amounts of excess heat present during an accident scenario to be transported to the outer walls of the reactor structure via radiation. However, if such a method of heat dispersal is to be depended on, an accurate estimate for the emissivity of the graphite within the core at the time of the accident is needed. Additionally, if the accident itself, such as in the case of an air ingress, has the potential to alter the graphite's emissivity, the phenomenon must be fully understood as well.

If the ash content of the graphite is high enough that an ash layer forms on the graphite surface, the emissivity of the graphite can be greatly reduced. Although nuclear graphite is

purified to total impurity levels below 300ppm, it is anticipated that over the lifetime of the reactor some of these impurities will eventually be oxidized and can form a light ash deposit on the outer surface of the graphite components. These oxidized impurities often exhibit a light gray color, and are associated with reduced emissivity and heat transfer efficiency from the purely black carbon-only surface of the graphite components. Figure 3.12 is provided as an example of some of the potential changes in surface properties which can be attributed to oxidation. Here, the oxidation is shown to radically change the appearance – and therefore likely also the emissivity – of a typical graphite sample that suffers from an above average level of impurities.

If the ash content of the graphite is high enough that an ash layer forms on the graphite surface, the emissivity of the graphite can be greatly reduced. To demonstrate this effect an assembly of 7 graphite rods with an ash content of less than 500 ppm were packed in a manner similar to that shown in Figure 4.10 on page 105 and heated to 900 °C in the open atmosphere. During the test, large apparent inter-rod temperature variations began to appear. However, these variations in apparent temperature were identified as being solely caused by oxide layers that built up on the faces of different rods at different rates. In reality, the average temperature of each rod in the assembly were almost identical, however, as can be seen in Figure 3.13, the amount of thermal energy they emitted was very different.

In Figure 3.13, three pseudo-colored images are shown from the aforementioned test. The data with which these images were made were obtained from IR camera images taken immediately before, during, and immediately after the detachment of a flake of the ash layer that had grown on the surface of the graphite. The rods on which a complete ash layer has formed can be identified in Figure 3.13 by their blue – rather than orange – appearance.

The plot shown in Figure 3.14 is an approximate calculation for the ratio of the average emissivities between the outer rods identified in Figure 4.10 as numbers 1 and 2. This value is plotted over a chosen time period of interest during the initial heating of the graphite test pieces while they were exposed to the atmosphere. The x-axis reference point $t_0 = 0$ seconds was set to be equal to the time of the frame shown in Figure 3.13b, at which the flake detached from the rod. At this point in time, the ratio of emissivities plotted in Figure

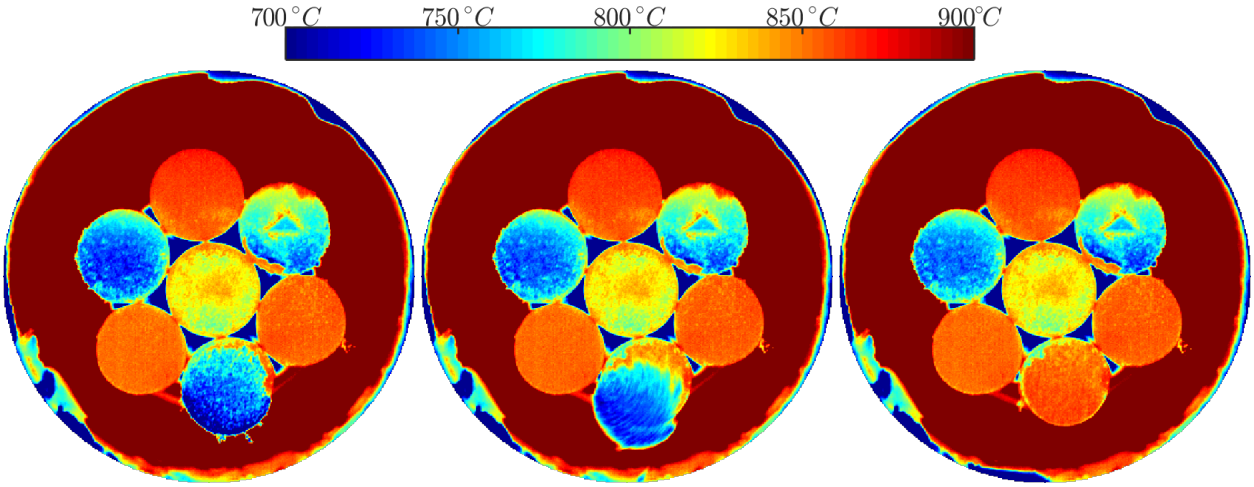

(a) *Attached ash layer* **(b)** *Detached ash layer* **(c)** *Clear surface*

Figure 3.13: *Emissivity change due to ash layer forming and leaving graphite face*

3.14 suddenly increases by about 50%. The timing of this jump perfectly coincides with the detachment of the oxide layer from the face of the rod as shown in Figure 3.13b. Therefore, it can be safely concluded that the variation in rod temperature seen by the camera and shown in Figure 3.13 is indeed due to the spatially and temporally varying emissivity caused by the formation of oxide layers on the surface of the graphite rods. Each of the rods in the assembly exhibited similar behavior throughout the experiment; their emissivities would slowly drop as an ash layer formed on the surface of the rod, the layer would fall way, and then the emissivity of the rod would return to it's initial state. The effect of the ash layer on emissivity was seen to be equal for all of the rods in the assembly.

For this calculation, it was assumed that both the average temperature and cross-sectional area of each rod were identical and did not vary temporally during the specified time period during which the measurement was taken. The IR camera was set to record 6.25 frames per second, which resulted in a measurement time of .16 seconds. With these assumptions, any temperature differences observed between these two rods would therefore be the direct result of differing emissivities. Indeed, analysis of Figures 3.13 and 3.14 provides confirmation that, in an oxidizing environment, variations in emissivity far and away become the dominating factor in apparent temperature differences between outer rods.

Oxidation reactions are also known to affect the emissivity of graphite by changing a

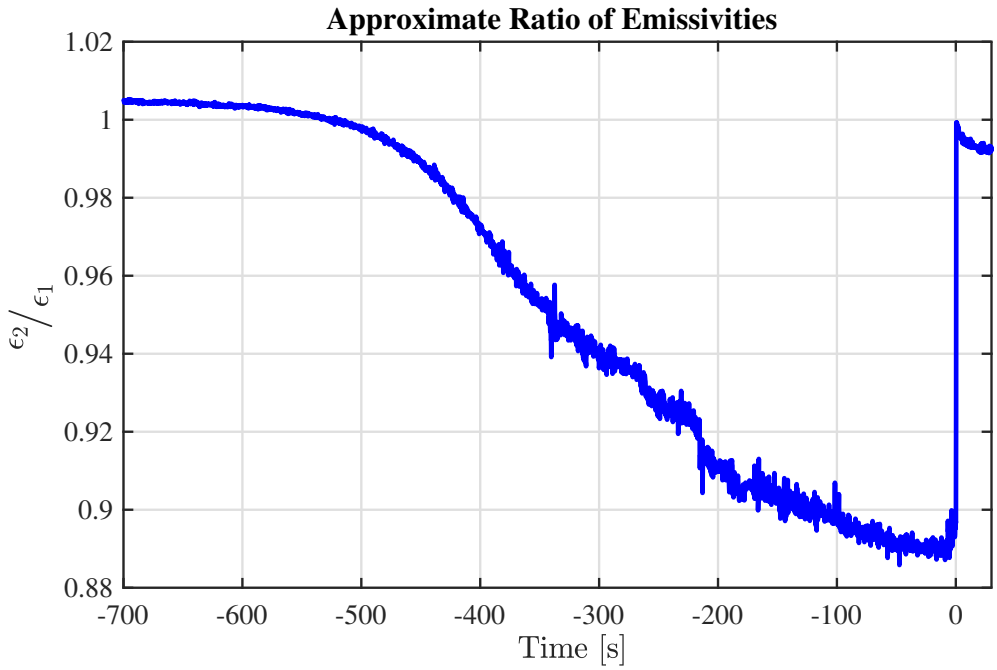

Figure 3.14: *Change in relative emissivity due to an ash layer first building, and then leaving a graphite surface. Figure from Ref. [23]*

material's surface roughness.

In contrast, oxidation – which, as demonstrated in Section 3.2.4.3 can substantially increase surface roughness – has been previously shown to increase the emissivity of graphite over certain wavelengths [24]. Thus, total change in the emissivity of graphite in an HTGR will be a function of several different variables, and combined effects experiments are required for a meaningful understanding of the phenomenon.

3.3.2 LWIR Emissivity Measurements

The FLIR A655sc thermal imaging camera was used characterize the emission properties of the G-348 graphite in the long wave domain. The camera has a spectral range of about 7.5 - 14 micron. Although the specific spectral response of the sensor is proprietary, the camera's calibration curve is programmed into the camera itself and can be used in FLIR's proprietary software, allowing for approximate values for average normal Emissivity in the spectral region to be backed out. To do this, a high-temperature paint known to have a constant emissivity in the region of interest was applied to a small portion of the observable face of a graphite test

piece and the entire test piece was heated to a constant, uniform temperature - usually 1173 K. Once the G-348 test piece was brought to steady state conditions, it could be assumed that any apparent temperature differences reported by the thermal camera between the pixels of the painted surface and those immediate surroundings was due solely to emissivity differences between the paint and the G-348. As the spectral emission of the paint is well characterized and known to be constant in the long wave domain [25], knowledge of the FLIR camera's specific spectral response is not needed for an accurate and relevant emissivity parameter to be specified for input into the FLIR software. Given the known emissivity of the painted region and specifying the mean temperature of the painted region as the true temperature of the pixels closely surrounding the painted region, the FLIR software will report the an average normal emissivity of bare G-348 surface in the 7.5-14 micron wavelength range. This process resulted in an un-oxidized, long wave normal emissivity value of 0.86 for bare, un-oxidized G-348 graphite with surface roughness similar to that of the 'Saw Cut' sample of Figure 3.10.

3.3.3 Experimental Procedure for Emissivity Experiments

To find out what affects the oxidation process had on the emissivity of G-348, several experiments were carried out in which the IR camera was used to monitor the lower face of the graphite test piece as it was impacted by oxidizing flow. For these tests, the vast majority of the G-348 test piece was coated with a material known to inhibit oxidation. The only uncoated areas on the test pieces were found on the lower – i.e. in terms of its positioning in the furnace – face of the test cylinders, a portion of which was left bare to interact with the flow. Additionally, on some test pieces part of the uncoated region on the lower face was painted with the known emissivity paint. As this painted section was placed directly next to the bare portion of the lower face, any observed differences in the steady state temperatures on a virgin test piece between bare and painted regions could be attributed to emissivity. The cylinders used in these tests possessed the same I.D and O.D as those discussed in Section 3.2.2, but were 76.2 mm long. The following procedure was used for these experiments:

1. The G-348 test piece was inserted into the left leg of the quartz apparatus.

2. Valves were closed and covering flanges attached to seal the system.

3. The system was evacuated to a rough vacuum and then back filled with helium.

4. The tube furnaces surrounding the test piece were turned on and the sample was heated to a steady state temperature of 900 °C. System pressure was maintained at close to atmospheric throughout this process by using an exhaust valve to let excess helium escape as needed.

5. The power output of the furnace was constrained to a narrow range around the output value that resulted in the steady state conditions. The allowed variation in output was large enough to allow the temperature controller within the furnace to maintain a steady state temperature before the initiation of flow, but small enough that the system could be accurately described as under constant flux

6. After steady state conditions had been achieved, the ball valve attached to the lower right leg was opened. Immediately following this, the DAQ was commanded to send the proper voltage signal to the mass flow controller, beginning bulk flow through the system.

7. Flow was continued for a predetermined amount of time, during which the spatial temperature distribution of the lower face of the test piece was recorded by the IR camera.

8. Bulk flow was stopped and the system was sealed, evacuated, and either cooled or brought back to steady state conditions for another experiment.

3.3.4 Results and Analysis - Emissivity Experiments

The state of the G-348 test cylinders after being tested is shown in Figure 3.15. In Figure 3.15a, the three different sections of the visible, or lower, face are identified. The 'Coated'

section is covered with the anti-oxidation coating, the 'Bare' section is bare G-348, and the 'Painted' section is the area that was originally covered with the known-emissivity paint. Although remnants of the paint can still be identified in this last section, most of the paint disintegrated midway through the second test. The sample shown in Figure 3.15a was tested at 900 °C with 15 SLM air flowing through it.

Even greater damage is seen in 3.15b which shows the sample that was tested at 1000 °C in 6.8 SLM of pure oxygen. Half of the visible face of this test piece was coated and half was left bare. After being exposed to the oxygen flow for a total of 15 minutes, the oxidation reaction had removed the top 4 mm of graphite from the bare section of the visible face.

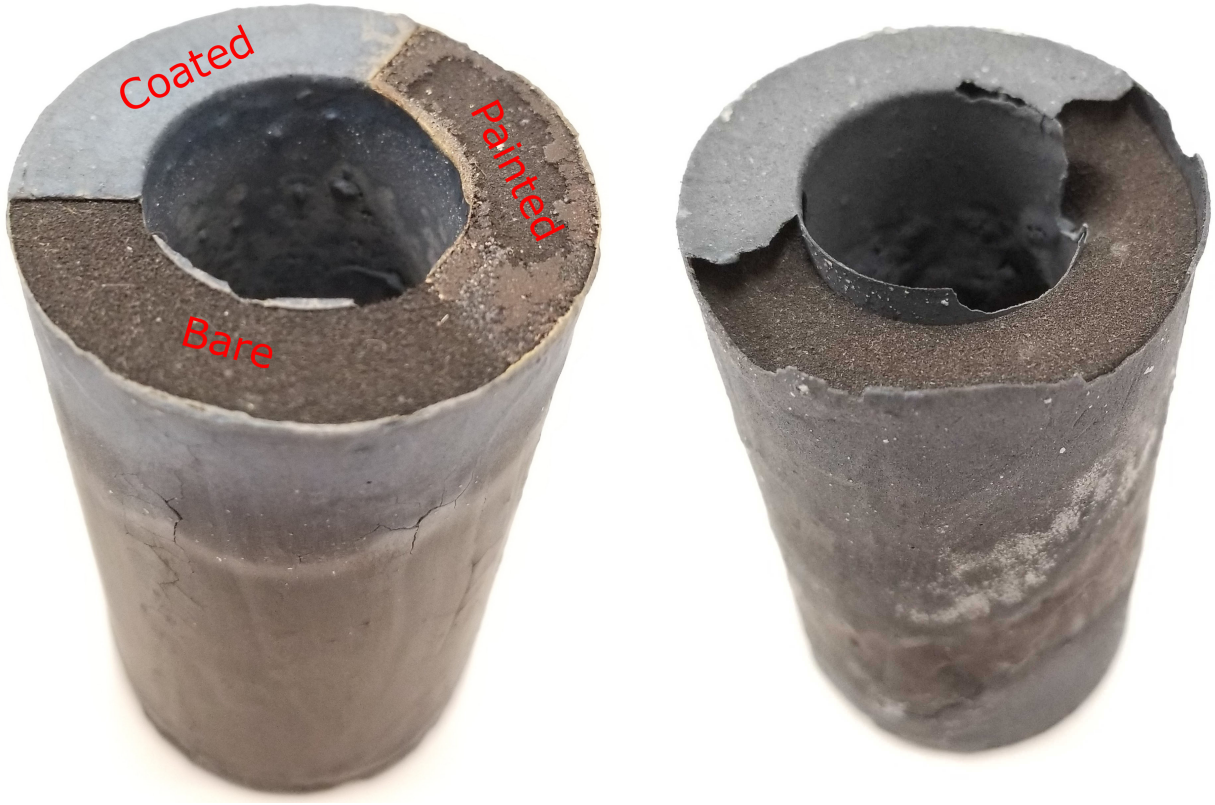

(a) *Damage resulting from a total of 12 minutes of 15 SLM air flow.*

(b) *Damage resulting from a total of 15 minutes of 6.8 SLM O_2 flow.*

Figure 3.15: *Condition of the G-348 cylinders that were partially coated with the anti-oxidation coating after testing.*

In Figure 3.16, the temperature response of the face of the graphite test pieces to the oxidizing flow is plotted for several experimental runs. For each of the runs shown in Figure

3.16a, 3.16b, the average temperatures of the 'Bare' and 'Painted' sections are plotted. Air flow was begun 30 seconds into Figure 3.16a and 20 seconds into 3.16b. At each of these points, a sharp jump in the temperatures of both sections identifies the moment that the oxidation reaction began. 6 minutes later, each plot shows another sudden temperature spike. This spike indicates the moment that air flow was stopped in each experiment. At that moment, excess oxygen is still present in the area surrounding the test pieces and thus the oxidation reaction continues relatively unabated for another few seconds before the remaining oxygen is used up. However, as the bulk flow of air has already stopped, the amount of convective cooling felt by the test piece is already greatly reduced. This combination of events leads to the temperature spikes shown at approximately 400 seconds in Figure 3.16.

Despite enduring the same rate and duration of oxidizing flow, the temperature histories shown in Figure 3.16b appear very different from those in Figure 3.16a. This is due to the disintegration of the known-emissivity paint that occurred during the second run. Even at the beginning of the 2nd run, the paint – which is specified only for "intermittent" use at 900 °C – had begun to be removed by the combination of high temperatures and oxidizing flow. This increased the amount of reactive surface area available to the oxidation process and leads to the higher overall temperature of the 'Bare' section seen in Figure 3.16b compared to Figure 3.16a. Eventually however, as more paint is lost and the visible surface of that section approaches what is seen in Figure 3.15a, the average emissivity of the 'Painted' section begins to approach that of the 'Bare' surface, resulting in the apparent – but not actual – temperature drop seen for mean temperature of the 'Painted' section in Figure 3.16b.

As each sample was brought to a steady state, uniform temperature before each of the runs began, the apparent variance in the steady state temperatures of the bare and painted surfaces shown over the first 20 seconds of data plotted in Figure 3.16b indicates that the emissivity of the bare graphite surface has increased since the start of the first run. This 25 °C jump indicates an approximate emissivity change of 3.5%. This is less than the 5 - 15 percent increase seen by Plunkett and Kingery [21], but as the graphite they used was not

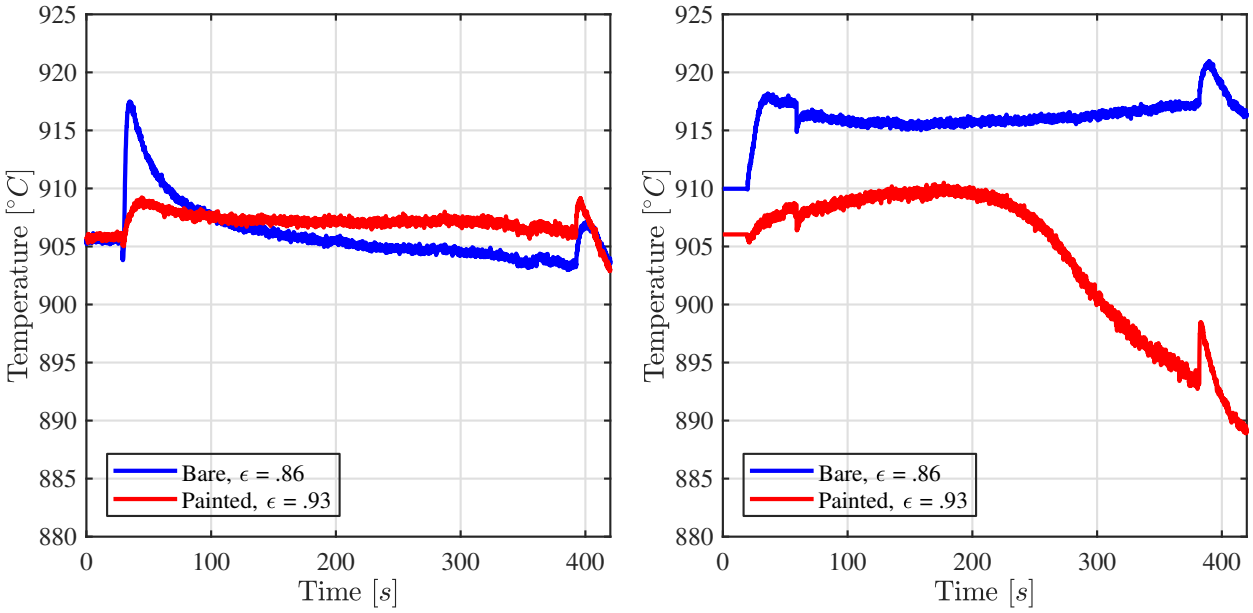

(a) *15 SLM air – 1st run*

(b) *15 SLM air – 2nd run*

Figure 3.16: *Effect of oxidation on LWIR emissivity.*

nuclear grade graphite [26], it is likely that their sample was simply more affected by the oxidation.

In contrast to the small changes in temperature seen in the air flow experiments in Figure 3.16, the trials that resulted in the damaged test piece shown in Figure 3.15b were conducted at a higher initial temperature and with pure oxygen rather than atmospheric air. In this run, 6.8 SLM of O_2 was flown through the test piece for approximately 7 minutes. The temperature history of the average temperature of the bare region of the cylinder's visible face is shown in Figure 3.17. The magnitude of the temperature increase caused by the pure oxygen in this run indicates that this is likely an example of oxidation in the diffusion controlled regime. This interpretation also fits with previously determined values for the transition temperature between the in pore diffusion and fully boundary layer controlled regimes of oxidation occurring in the vicinity of 1123 °C [6, 12].

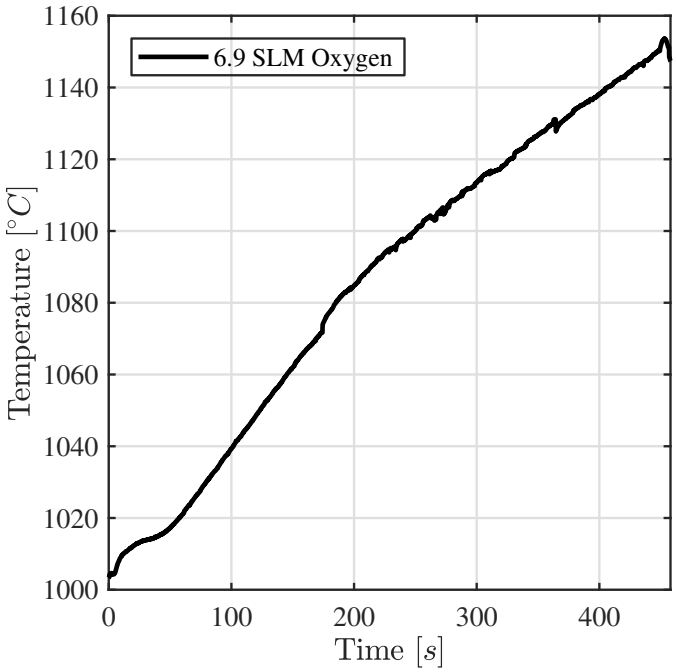

Figure 3.17: *'Bare' section average temperature during flow of 6.9 SLM O_2*

3.4 Conclusion

In the transition region between the diffusion controlled and boundary layer controlled regimes, the precise effects of oxidation on a particular sample's thermal diffusivity is difficult to precisely predict. However, the direction of the effect was seen to be constant for all tested samples. After an accident, an increased thermal diffusivity would allow thermal energy to dissipate through the graphite structure more quickly. Although it is unable to be directly measured, based on the very short depth of the observed porous layer on the graphite samples tested, it was concluded that the thermal conductivity of the graphite samples was likely unchanged by the oxidation process. However, if this increased thermal diffusivity is, as suggested in this work, caused by a decrease in the graphite's density, the thermal capacity of the graphite within the HTGR will decrease. Which of these variables is more important will depend on the time scale of the energy release with in the reactor and the relative amount of heat being transported out of the core by conduction through the graphite.

Emissivity is a function of both macroscopic and microscopic variables. If an air ingress

were to occur within an HTGR, both macroscopic and microscopic effects known to affect graphite emissivity are likely to occur. If large amounts of impurities have built up into the graphite over time and significantly elevated its effective ash content, then an air ingress is likely to severely inhibit the radiative heat transfer abilities of the graphite due to the formation of low emissivity, ash layers on its surface. However, if the purity of the graphite is still close to that of its virgin specifications when the air ingress were to occur, the oxidation induced roughening of the graphite surface would have the effect of slightly raising the its emissivity.

Although the lack of precise velocity measurements makes it impossible to conclusively state the exact reasons for the difference, the in-situ oxidation experiments performed natural convection resulted in more oxidation occurring than was predicted based on the forced flow experiments. Further research into the precise causes of this increased effect is therefore suggested.

Acknowledgments

The author would like to thank Ardalan Chaichi and Dr. Manas Gartia at Louisiana State University for performing the spectroscopic and laser flash tests on the oxidized graphite samples.

Bibliography

[1] Richard Edwin Nightingale. *Nuclear Graphite: Prepared under the Auspices of the Division of Technical Information United States Atomic Energy Commission*. Academic press, 2013.

[2] Donald G Schweitzer. Oxidation and Heat Transfer Studies in Graphite Channels I. The Effect of Air Flow Rate on the CO 2 and CO-O 2 Reactions. *Nuclear Science and Engineering*, 12(1):49–45, 1962.

[3] Donald G Schweitzer. Oxidation and Heat Transfer Studies in Graphite Channels III. The Chemical Reactivity of BNL Graphite and Its Effect on the Length of Channel Cooled by Air. *Nucl. Sci. Eng.*, 12(1):51–58, 1962.

[4] D. G. Schweitzer. Experimental results of air ingress in heated graphite channels. In *Responce of fuel, fuel elements and gas cooled reator cores under accidental air or water ingress conditions*, number October, pages 50–55, Beijing, 1995.

[5] Jo Jo Lee, Tushar K. Ghosh, and Sudarshan K. Loyalka. Comparison of NBG-18, NBG-17, IG-110 and IG-11 oxidation kinetics in air. *Journal of Nuclear Materials*, 500:64–71, 2018. ISSN: 00223115. DOI: 10.1016/j.jnucmat.2017.11.053.

[6] Se-Hwan Chi and Gen-Chan Kim. Comparison of the oxidation rate and degree of graphitization of selected ig and nbg nuclear graphite grades. *Journal of Nuclear Materials*, 381(1):9–14, October 2008. ISSN: 0022-3115. URL: http://www.sciencedirect.com/science/article/pii/S0022311508003954.

[7] Mohamed S. El-Genk and Jean-Michel P. Tournier. Comparison of oxidation model predictions with gasification data of ig-110, ig-430 and nbg-25 nuclear graphite. *Journal of Nuclear Materials*, 420(1-3):141–158, 2012. ISSN: 0022-3115.

[8] Tetsuaki Takeda and Makoto Hishida. Studies on molecular diffusion and natural convection in a multicomponent gas system. *International Journal of Heat and Mass Transfer*, 39(3):527–536, 1996. ISSN: 00179310. DOI: 10.1016/0017-9310(95)00148-3.

[9] Chang H Oh, Cliff Davis, Larry Siefken, Richard Moore, Hee Cheon NO, Jong Kim, Goon C Park, John C Lee, and William R Martin. Development Of Safety Analysis Codes And Experimental Validation For A Very High Temperature Gas-Cooled Reactor. Technical report INL/EXT-06-01362, Idaho National Labratory, Idaho Falls, 2006.

[10] Lance L. Snead, Christian I. Contescu, Thak Sang Byun, and W. Porter. Thermophysical property and pore structure evolution in stressed and non-stressed neutron irradiated ig-110 nuclear graphite. *Journal of Nuclear Materials*, 476:102–109, 2016. ISSN: 0022-3115.

[11] Ram Krishna, James Wade, Abbie N. Jones, Michael Lasithiotakis, Paul M. Mummery, and Barry J. Marsden. An understanding of lattice strain, defects and disorder in nuclear graphite. *Carbon*, 124:314–333, 2017. ISSN: 00086223. DOI: 10.1016/j.carbon.2017.08.070.

[12] Jo Jo Lee, Tushar K. Ghosh, and Sudarshan K. Loyalka. Oxidation rate of nuclear-grade graphite NBG-18 in the kinetic regime for VHTR air ingress accident scenarios. *Journal of Nuclear Materials*, 438(1-3):77–87, 2013. ISSN: 00223115. DOI: 10.1016/j.jnucmat.2013.11.032. URL: http://linkinghub.elsevier.com/retrieve/pii/S0022311513012695.

[13] Jo Jo Lee, Tushar K. Ghosh, and Sudarshan K. Loyalka. Oxidation rate of nuclear-grade graphite IG-110 in the kinetic regime for VHTR air ingress accident scenarios. *Journal of Nuclear Materials*, 446(1-3):38–48, 2014. ISSN: 00223115. DOI: 10.1016/j.jnucmat.2013.11.032. URL: http://linkinghub.elsevier.com/retrieve/pii/S0022311513012695.

[14] Mohindar S. Seehra and Arthur S. Pavlovic. X-ray diffraction, thermal expansion, electrical conductivity, and optical microscopy studies of coal-based graphites. *Carbon*, 31(4):557–564, 1993. ISSN: 0008-6223.

[15] Z. Zhou, W. G. Bouwman, H. Schut, and C. Pappas. Interpretation of x-ray diffraction patterns of (nuclear) graphite. *Carbon*, 69:17–24, 2014. ISSN: 0008-6223.

[16] Guiqiu Zheng, Peng Xu, Kumar Sridharan, and Todd Allen. Characterization of structural defects in nuclear graphite IG-110 and NBG-18. *Journal of Nuclear Materials*, 446(1-3):193–199, 2014. ISSN: 00223115. DOI: 10.1016/j.jnucmat.2013.12.013.

[17] W. J. Parker, R. J. Jenkins, C. P. Butler, and G. L. Abbott. Flash method of determining thermal diffusivity, heat capacity, and thermal conductivity. *Journal of applied physics*, 32(9):1679–1684, 1961. ISSN: 0021-8979.

[18] Mohamed S. El-Genk and Jean-Michel P. Tournier. Development and validation of a model for the chemical kinetics of graphite oxidation. *Journal of Nuclear Materials*, 411(1-3):193–207, 2011. ISSN: 00223115. DOI: 10.1016/j.jnucmat.2011.01.129.

[19] Mohamed S. El-Genk and Jean-Michel P. Tournier. Validation of gasification model for nbg-18 nuclear graphite. *Nuclear Engineering and Design*, 250:142–155, 2012. ISSN: 0029-5493.

[20] 1 ASME B46. Surface texture (surface roughness, waviness, and lay): an american national standard, 2002.

[21] J D Plunkett and W D Kingery. THE SPECTRAL AND INTEGRATED EMISSIVITY OF CARBON AND GRAPHITE. In *Carbon*, volume 26, pages 457–472, 1960. ISBN: 9781483198354. DOI: 10.1016/B978-1-4831-9835-4.50054-9. URL: http://www.sciencedirect.com/science/article/pii/B9781483198354500549.

[22] Will Windes. NGNP Graphite R&D Technical Lead, Idaho National Labratory, 2014.

[23] Dan Gould, Hanwen Liu, and Hitesh Bindra. Thermographic Studies on the Impact of Material Discontinuities and Oxidation on the Thermal Behavior of a Graphite Matrix. In *NURETH-16*, 2015.

[24] Y S Touloukian and David P DeWitt. Thermal radiative properties: nonmetallic solids. In *Thermophysical Properties of Matter, Vol.8*. 1972. ISBN: 0-306-67020-8.

[25] Jean-Remy Filtz, Ingrid Wetterlund, Bror Persson, Petra Andersson, Robert Jansson, Tony Lemaire, Maria Öhlin, Jukka Myllymäki, Jean-Remy Filtz, Ingrid Wetterlund, Bror Persson, Petra Andersson, Robert Jansson, Tony Lemaire, Maria Öhlin, and Jukka Myllymäki. Improving heat fluxmeter calibration for fire testing laboratories (HFCAL) Final report. Technical report, 2002, pages 1–121.

[26] Julian Glasser and William Glasser. Directory of Graphite Availability. Technical report, Air Force Materials Laboratory, Wright-Patterson, 1967, page 195.

Chapter 4

Safety Implications of Point Thermal Contacts

4.1 Introduction

Numerous thermal engineering applications – such as nuclear waste systems, nuclear reactors, high temperature catalytic reactors, heat removal from computer chips – involve two major challenges: in-situ measurement of temperature at different locations within the spatial domain, and material heterogeneities or discontinuities within the domain that makes their thermal behavior prediction or estimation difficult. These practical examples involve heat transfer across fixed (welded, soldered) or loose joints between solid objects. In these cases, it is often difficult to predict or measure temperature – a problem that makes thermal design particularly challenging. Direct or indirect heat transfer between solids is also of significance in various problems in which the materials (solids) develop cracks and the effective heat transfer through the material is dependent upon the thermal contact conductance between the cracked, discontinuous regions [1].

When these heterogeneous systems have solids in contact with one another, they exhibit finite thermal contact conductance and radiative heat transfer through interacting surfaces. In order to use the classical continuum approach to predict the thermal behavior of such systems, it is important to understand and resolve the thermal contact conductance. Although there are several thermal contact conductance models detailed in the literature [2–4], they assume that contact spots are circular with identical radii. However, in a realistic situation, when two objects are brought in contact, surface irregularities introduce variations in their contacts. Predicting energy flow using these models require detailed information about these contacts and the resulting gaps between the solids, which is usually very difficult to obtain. Other limitations associated with adopting continuum models for these complex geometries are that analytical solutions do not exist, and numerical discretization becomes challenging as the nodal contacts between different heterogeneous regions, where interface boundary conditions are applied, are completely grid size dependent.

Various models have been proposed in the literature to overcome some of these limitations [5, 6]. Yovanovich [5] reviews the role of geometry, mechanics and thermal physics to model thermal contact resistances, and discusses various improvements on the earlier mod-

els. Another mechanical, geometrical approach to model thermal contact conductance was proposed by Salgon et al. [7], which depends upon contact area between two bodies. Singhal et al. [8] developed surface topography and material property dependent model for axially contacting cylinders which was experimentally validated. Xu et al. [9] described thermal contact at different roughness scales using a fractal description. However, the requirement that the contacts need to be described at macroscopic to microscopic levels based on resolution of the geometry, still persists. This increases the complexity and reduces the reliability and general applicability of the models. In large systems with length scales of a few meters, it is difficult to resolve features below millimeter level. Verma et al. [10] recently introduced a stochastically reconstructed topography to extract a thermal contact conductance model at interfaces between solids.

Traditionally, thermal contact conductance is modeled as a heat transfer coefficient that is obtained from the experimental data. Thus, thermal contacts arising due to physical discontinuities have previously been modeled using empirical correlations based on experimental data availability. Data obtained from past experiments generally consisted of embedded thermocouple responses. This provided limited information at very low spatial resolution. Thermocouple embedding is associated with creation of heterogeneous contacts between two different materials. Models constructed from these low fidelity experimental data were not sufficient to capture either the spatial or the temporal effects of the individual point contacts. Therefore, uncertainties associated with these intrusive temperature measurement systems are not negligible. Additionally, it may not even be possible to install such intrusive temperature measurement devices in many practical systems. Therefore, learning from experiments using detailed local measurements via non-intrusive instrumentation is probably the most effective approach. Due to the high resolution data requirements for such models, high fidelity non-intrusive techniques were developed [11–13]. A study by Burghold et al. [11] provides a method to estimate heat transfer coefficients with transient temperature measurements using thermographic images. Dynamic estimates of heat transfer mechanisms can then be utilized for describing the transient heat transfer under different test conditions. With improved resolution and speed, modern IR thermography can significantly improve the

understanding and modeling of thermal contact resistances in various practical systems.

However, even with the use of modern IR cameras, inverse heat transfer problems involving non-homogeneous solids or assemblies of different solids, where multiple thermal contacts and gaps between different solids constitute the major heat transfer resistance, can be a daunting task. This is because thermographic or non-intrusive measurements of the temperature at any internal contacts are not possible even through an IR transparent window. The challenge is to use the bulk surface temperature measurements that can obtained from an IR camera along with other available information, such as geometric arrangement, in order to construct the unknown internal temperature distributions of multiple solids in thermal or physical contact. A spatio-temporal regression algorithm is required to fuse the surface IR signal response to the material or geometric information in order to obtain the temperature map for the entire domain of interest.

4.2 Effective Thermal Conductivity

In packed beds, such as found in the Pebble Bed Reactor (PBR) and MGTHR HTGR designs, the existence of the point-to-point contacts between the particles greatly complicates any analysis of heat transfer within the bed. A common method of analysis for such beds is to represent the entire bed as a single, homogeneous domain with modified material and thermal properties. In particular, the thermal conductivity of the representative homogeneous domain is defined as the effective thermal conductivity, k_{eff}, of the packed bed, as opposed to the bulk thermal conductivity value of the bed's constituent material. The effective thermal conductivity of a region within such a packed bed is generally calculated by lumping all relevant heat transfer mechanisms into a single representative value [14]. Heat transfer mechanisms often taken into account in the calculation of k_{eff} include: conduction through individual particles, conduction between particles across solid contact areas, conduction between particles through a fluid, radiative heat transfer between particles, and inter-particle convective heat transfer. In this study, however, the conduction between particles across solid contact areas element is the area of primary focus.

4.3 Experimental Work

4.3.1 Experimental Setup Design and Construction

The experimental setup was designed so that all test pieces could be observed with a FLIR A-655sc LWIR camera. Due to its capability of measuring the spatial variation in surface temperature at a much higher resolution than almost any other method of temperature measurement the use of the IR camera provides significant advantages over the use of individual thermocouples. Additionally, the accuracy of thermocouple sensors is itself a function of thermal contact conductance, which can introduce uncertainty in the measurement. The IR camera was also used to confirm that no significant temperature gradients existed across the face of each rod.

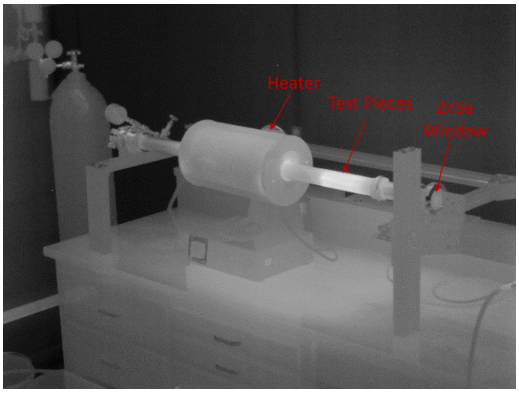

(a) *Infrared image of completed experimental setup*

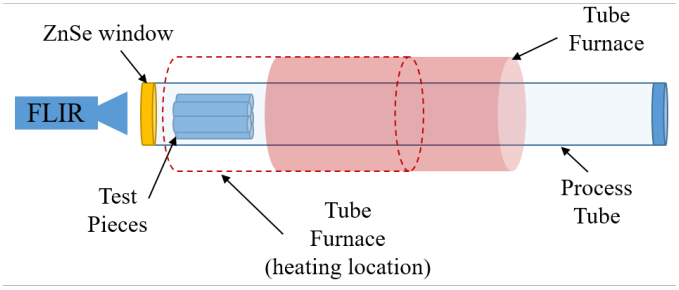

(b) *Schematic of the experimental setup*

Figure 4.1: *Image and schematic of the experimental setup*

A 46mm ID by 50mm OD quartz tube was used to hold the tested assemblies. Heat was applied using electrically powered tube furnaces. The quartz process tube was chosen to hold the test samples within the furnace due to several advantages such as SWIR transmission and low thermal conductivity. The radiative heat from the electrical heater can be efficiently transmitted through the quartz tube in the temperature range of interest (at high temperature 1000-1500 K). Each end of the quartz process tube was sealed with compression fittings that allowed the attachment of KF style fittings to each end of the tube. Due to the choice of graphite as one of the test rod materials, it was important to ensure an inert environment

existed within the tube to prevent undesired oxidation from occurring during tests. The completed setup was customizable and capable of conducting numerous high temperature experiments with test pieces of up to 45 mm in diameter in inert, oxidizing, and vacuum environments.

A completed setup and its supporting structure is shown in Figure 4.1a. When this image was captured, the heater had recently been moved from its original position surrounding the test sample within the tube. The bright section of the quartz chamber to the right of the furnace in Figure 4.1a identifies the location of the cooling test pieces. A schematic of the setup can be seen in Figure 4.1b. The dotted line presents the position of the external radiative heater before initiating the cool-down experiments.

A custom view port utilizing a ZnSe window was also designed, machined and built utilizing the KF flange interface provided by the compression fittings, so that the long wave IR camera could be used to measure the spatial and temporal variation of temperature inside the entire domain throughout an experiment. As the transmission of the ZnSe window has the potential to vary significantly depending on it's condition and coating, it was necessary to determine its transmission over the LWIR domain. This correction factor for transmission is obtained first heating a test piece to a steady state temperature and then observing said test piece with the FLIR camera and inserting, then removing the ZnSe window from the camera's view path. Although it's true temperature will be constant through the process, as the window will block some of the emitted LWIR radiation from reaching the camera's sensor, the FLIR camera will report an apparent change in the test piece's temperature with insertion or removal of the window. The windows transmission was then calculated from the magnitude of the signal difference obtained with and without the window.

Details of the rod assemblies tested in this work are given in Table 4.1. Pictures of example assemblies of each tested type are shown.

1	2	3	4	5	6
			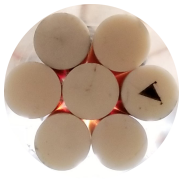		
G-348 Graphite 30 Rods 2.5 mm Radius 72 mm Length Thin Shell	G-348 Graphite 18 Rods 2.5 mm Radius 72 mm Length Thick Shell	G-348 Graphite 7 Rods 7.5 mm Radius 152 mm Length No Shell	Alumina 7 Rods 7.5 mm Radius 152 mm Length No Shell	GE-214 Quartz 7 Rods 7.5 mm Radius 152 mm Length No Shell	GE-214 Quartz 68 Rods 2.5 mm Radius 72 mm Length No Shell

Table 4.1: *Details of tested rod assemblies.*

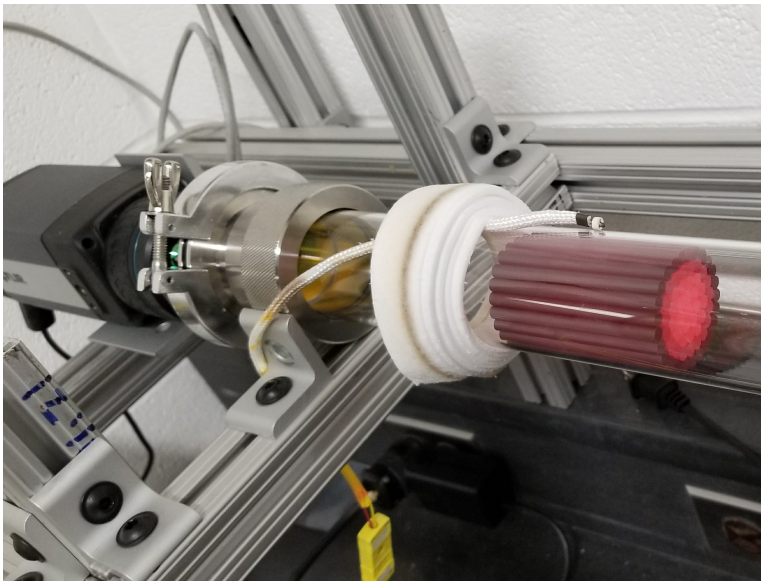

Figure 4.2: *Test assembly beginning to cool.*

4.3.2 Experimental Procedure

The test assemblies were placed within the quartz process tube so that they were as near to the minimum focal distance of the IR camera as possible without requiring a heater placement that could overheat the tube seals or ZnSe window. Once the assembly was placed inside the process tube, the process tube was sealed, evacuated to a full rough vacuum, and the radiative heater was switched on. The assembly was heated until all rods reached the desired steady state temperature.

To initiate the cooling experiment, the radiative heater was switched off and quickly

moved away from its original location surrounding the assembly. Figure 4.2 shows a cooling assembly of graphite rods. The dotted line in Fig. 4.1b shows the position of heater before initiating cool-down experiment. Care was taken to assure that the tube furnace was always moved far enough from the test pieces that any residual heat contained within the tube furnace would not affect the cooling rate of the tested samples. The cooling assembly was monitored throughout this process via the IR camera through the ZnSe window.

4.3.3 Image Processing

The thermal images of the rods (flat surfaces) transmitted through the ZnSe windows and captured by the IR camera during the dynamic cooling experiments described above were processed to obtain the training and test data. Figure 4.3 shows the rod definition achievable using the thermographic camera (resolution 640×480). The spatial resolution of images in the configuration used for these experiments is approximately 0.2 mm per pixel.

For each experiment, the images recorded by the IR camera are analyzed with the goal of obtaining three different measurements - the temporal change in temperature of each rod during the experiment, the location of each rod, and the identity and number of rods each rod is in physical contact with. In the case of the large-rod assemblies, a relatively simple approach can be adopted as, due to their size, only one packing arrangement of the 7 rods is possible within the quartz tube. The temporal variation in average temperature experienced by each of the seven rods is directly reported by the FLIR camera. In addition, for the large-rod assemblies, simple visual inspection of the IR images can provide the data for the number of physically touching rods in each of the simple assemblies. However, in case of small-rod assemblies, due to the large number of rods and the significantly increased packing complexity, an automated method of determining the temperatures, centers and contacts within each assembly was developed.

The Circular Hough Transform algorithm in Matlab image processing toolbox, *imfindcircles*, was used to find the center and radii of each of the rods seen by the IR camera. To help alleviate any errors that might have resulted from the IR camera's limited resolution,

the circle finding algorithm was sequentially run on a set of frames – generally about 200 in total – taken over a range of different assembly average temperatures. For each frame, the *imfindcircles* function was first run. Next, the center points of each located circle were analyzed to determine if that particular rod face had ever been identified in a previous frame. This process was repeated until each rod in the tested assembly was accounted for and their centroid locations known.

Once the center location of each rod was determined, the distance between the center of each rod and every other rod was obtained. These distances were then compared to the mean radius (in pixels) of all identified rods. Pairs of rods whose centers were found to be separated by a distance of approximately one rod diameter were defined as in physical contact with one another.

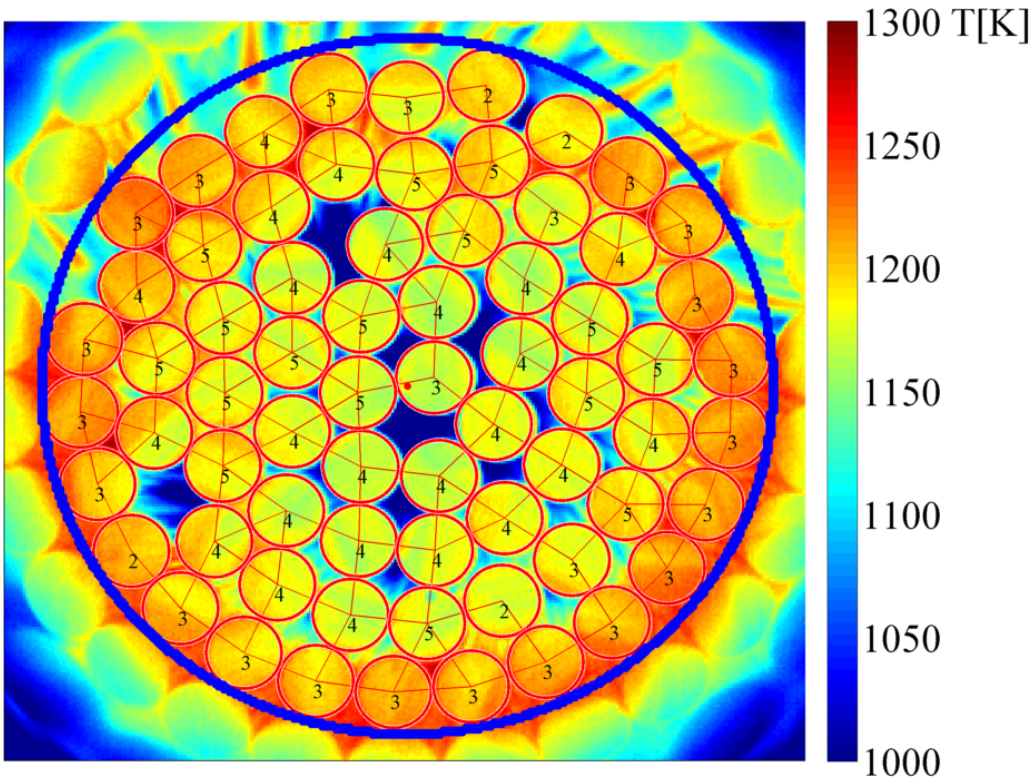

Figure 4.3: *Representative results from image segmentation and analysis. Color bar scale- Temperature [K]. Figure from Ref. [15]*

The results of the image segmentation process can be seen in Figure 4.3. In this figure, every circle found by the circle finding algorithm is displayed, overlaid on images obtained

from the IR camera. Each identified rod is circumscribed in red (color online), and the centers of rods deemed in contact with one another are depicted in the figure with edges connecting the rod centers. The total number of rods each rod is in contact with is also obtained. The identified rods, the identification of the adjoining neighbors for each identified rod, and the temperature history is used to generate a mathematical graph of the entire assembly, kernel matrices, and training and test data for the machine learning based regression analysis (see next section).

4.4 Application of Homogeneous Model

Thermal conduction in homogeneous solids at the macroscopic scale is a well established theory. Thus, if the temperature data at the surface of the solid could be obtained from surface measurements or remote measurements, the internal temperature distribution for homogeneous regions can be computed easily for dynamic or static physics. In the past, several researchers have solved inverse heat conduction problems to predict temperatures or heat flux conditions at unknown locations, using the measured or estimated data at known locations [16–19]. Colaco & Alves [20] developed a non-intrusive inverse heat transfer method using reciprocity functional approach to estimate spatially varying thermal contact heat transfer coefficients. Unfortunately, most of these methods are generally described as being restricted for use with homogeneous domains only.

However, although the rod assemblies tested in Section 4.3 are technically in-homogeneous in nature, the first modeling approach used was to attempt to represent the actual experimental geometries with an equivalent homogeneous domain. The goal was to find out if the effects of the point contacts in the experimental geometry could be adequately represented as a simple change in the bulk thermal conductivity of the representative medium. This method also serves as a baseline for comparison with the more advanced methods and methods discussed in Sections 4.5 and 4.6. It should also be noted that the homogeneous model presented here is also equivalent to the best possible porous media model. Porous media models attempt to predict the ideal k_{eff}, but are still homogeneous models. As the

present model uses an inverse heat transfer method to calculate the optimal k_{eff} for the specific geometry in question, any other k_{eff} provided by a conduction-only, porous media model will be, by definition, sub-optimal.

4.4.1 Model Description

1–D radial and 2–D axisymmetric homogeneous models were created for Assemblies 1 and 2 and an inverse heat transfer method was used to find the optimal k_{eff} for each assembly and model type. This was done in the following steps.

First, a direct solution for the homogeneous heat transfer problem for each assembly geometry and model type was obtained numerically. For 1–D radial model this meant discretizing and solving the one dimensional heat diffusion equation in radial coordinates, Equation 4.1a. For the 2–D model same process was done for the two dimensional heat diffusion equation in polar coordinates, 4.1b. The initial conditions used in numerically solving the direct problem posed by each numerical model were provided from an interpolation function applied to the spatial temperature data in the inital IR camera frame. In the case of the 1–D model, the radial position of each pixel was calculated. A low-pass filter was then applied to the measured temperatures before the radial temperature profile was provided to the interpolation function. For the 2–D method, no averaging was nessesary and the 2–D matrix of temperature data was directly provided to the interpolation algorithm used by the numerical solution for initial conditions.

$$\frac{\partial^2 T(r,t)}{\partial r^2} + \frac{1}{r}\frac{\partial T(r,t)}{\partial r} = \frac{1}{\alpha}\frac{\partial T\left(r,t\right)}{\partial t} \tag{4.1a}$$

$$\frac{\partial^2 T\left(r,\phi,t\right)}{\partial r^2} + \frac{1}{r}\frac{\partial T\left(r,\phi,t\right)}{\partial r} + \frac{1}{r^2}\frac{\partial^2 T\left(r,\phi,t\right)}{\partial \phi^2} = \frac{1}{\alpha}\frac{\partial T\left(r,\phi,t\right)}{\partial t} \tag{4.1b}$$

Next, the optimal value of thermal conductivity – i.e. the value of k_{eff} that would result in minimum mean norm 2 error was determined via an optimization process. In particular, Matlab's *lsqcurvefit* function was used with the trust-reflective-region algorithm [21]. The

	Assembly 1				Assembly 2			
	1–D		2–D		1–D		2–D	
Nodes	125	250	289	400	125	250	289	400
$\boldsymbol{k_{eff}}$ $\left[\frac{\mathrm{W}}{\mathrm{m\,K}}\right]$	1.416	1.415	1.725	1.760	1.597	1.597	2.090	2.128
$k_{eff}/k_{600\,^{\circ}\mathrm{C}}$	1.67E-02	1.67E-2	2.03E-2	2.07E-2	1.88E-2	1.88E-2	2.46E-2	2.50E-2
Residual Norm	9.01E6	9.00E6	4.05E7	3.92E7	2.74E6	2.74E6	7.31E6	7.16E6
Time Step [s]	6.25E-2	6.25E-2	8.34E-2	4.17E-2	6.43E-2	6.43E-2	4.28E-2	2.14E-2

Table 4.2: *Homogeneous Model Data*

stopping criteria for the optimization was defined in terms of both function tolerance and step tolerance, each with 1E-6 values. In practice, the function tolerance was generally satisfied first. More stringent stopping criteria were also tested, but the 1E-6 values were found to be sufficient.

For the final step in the process, the codes implementing the numerical solution of Equation 4.1 were run once more, this time using the optimal value of k_{eff} found by the optimization process.

4.4.2 Homogeneous Model Results

Table 4.2 provides results from the inverse method used. The effect of the point contacts reduces the effective thermal conductivity, k_{eff}, by factor of approximately 50 from the value reported for bulk, un-oxidized, G-348.

Although far fewer nodes were used in the 2–D models due to the explicit method's computational costs, mesh independence was still achieved.

4.4.2.1 1–D Homogeneous Model

The measured and predicted temperature profiles for the rods of assemblies 1 and 2 are plotted in Figure 4.4. Each line represents the avearge face temperature of an individual rod. The measured temperature profiles – i.e. those directly reported from the IR camera – are shown in blue while the temperature profiles given by the homogeneous model are colored red. The line denoted "Shell Temp" is the average temperature of the graphite shell

surrounding assemblies 1 and 2. This temperature was also used as the boundary condition for the 1–D homogeneous model.

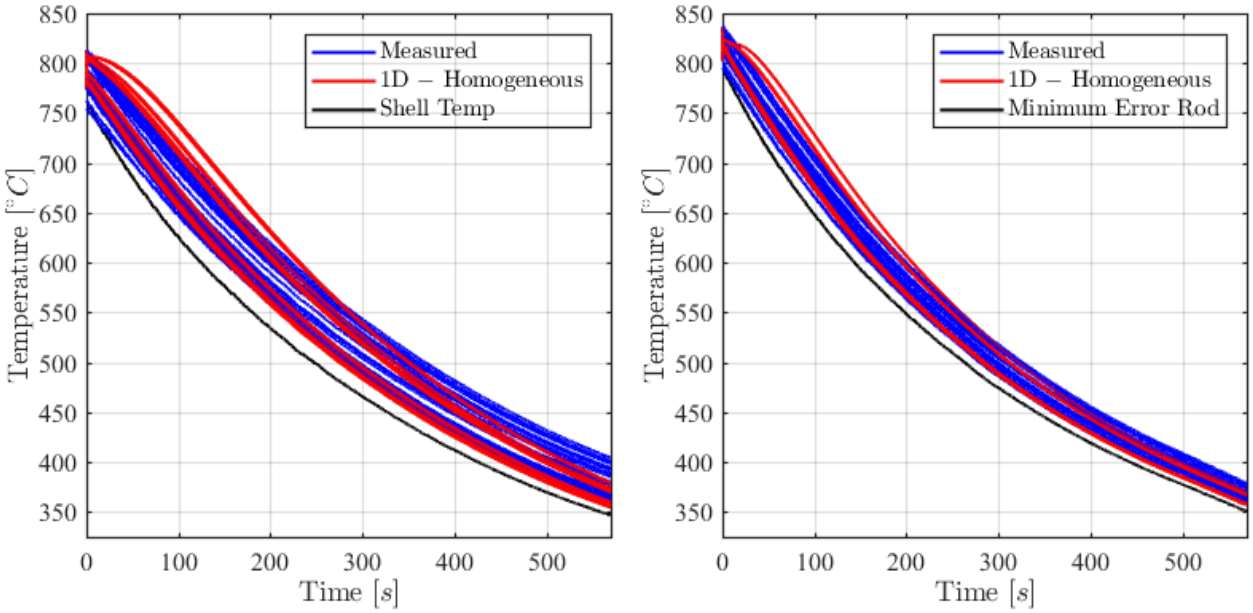

(a) *Thin shell* **(b)** *Thick shell*

Figure 4.4: *Comparison of measured vs. 1–D model temperatures.*

Although it appears that, compared to the number of measured temperature profiles, far fewer temperature profiles from the 1–D homogeneous model are plotted in Figures 4.4a and 4.4, this is not the case. Rather, the 1–D homogeneous model simply gave extremely 'banded' – i.e., graphicly overlapping – results with the majority of it's rod temperature results falling on one of three separate paths. This effect is caused by the packing structure of the rods in Assemblies 1 and 2. Spatial differences in the results of the 1–D model are a function of only a rods initial condition and radial location. The semi-regular, ringed nature of the structure means that all of the rods within the system are closely located to one of three distinct radii. Thus, for similar initial conditions, only 3 separate cooling paths are observable. This effect is better seen in Figure 4.5, in which the results from applying the 1–D homogeneous model to Assembly 1 are shown in pseudocolor by their radial location. Importantly, the banding effect is also not something that could be reduced by using any of the previously published effective thermal conductivity models. Again, this is due to the inverse heat transfer method already having found the optimal singular value of k_{eff} for this

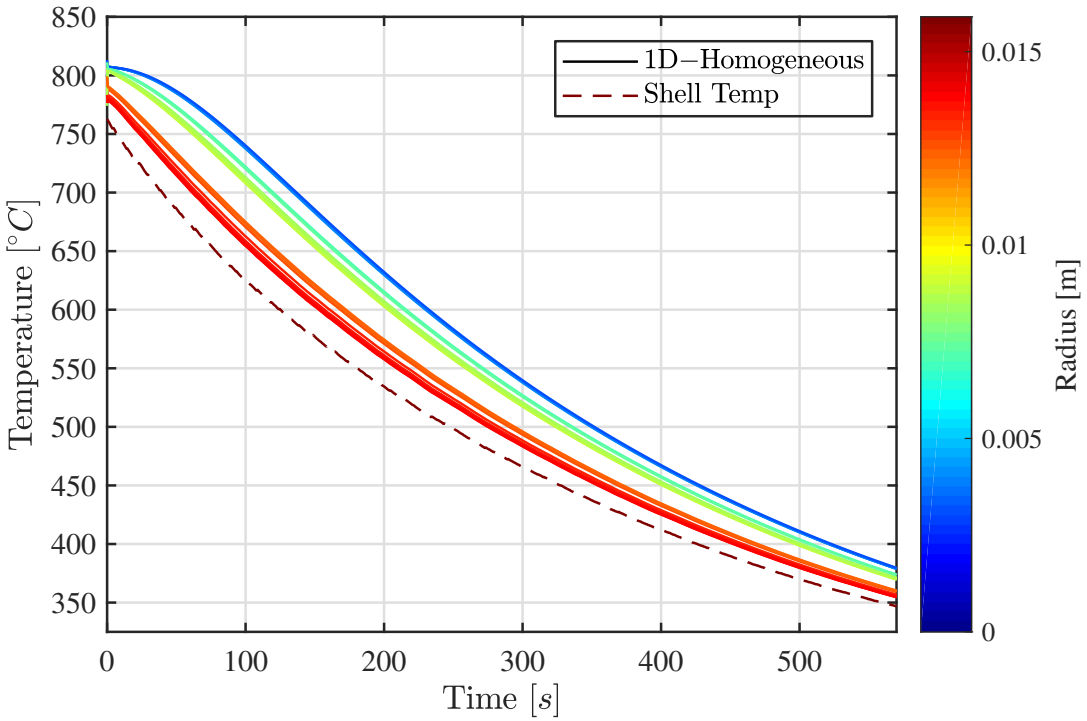

Figure 4.5: *1-D temperature profiles colored by radial location – Thin Shell Assembly*

particular data set.

Absolute and relative error given by the 1–D models can be seen in Figures 4.6 and 4.7, respectively. Despite the banding effects, the model was replicate the measured temperature profiles with less than a 5% mean error. Additionally, based on a later visual inspection, the faces of two of the rods within Assembly 1 are suspected to possess an emissivity that is noticeably different standard. As such a difference in face emissivity would result in measurement errors, if the experiment were to be redone with the suspect rods replaced, the model's prediction error would fall even lower.

4.4.2.2 2–D Homogeneous Model

A two dimensional, polar homogeneous model was also created to allow for more precise initial conditions to be applied to the homogeneous model. The initial conditions used in this model were again defined to be the temperatures of each rod's face, as reported by the IR camera, at time = 0 seconds. Computationally, the initial conditions for the numerical model were again provided from an interpolation function applied to the spatial temperature data

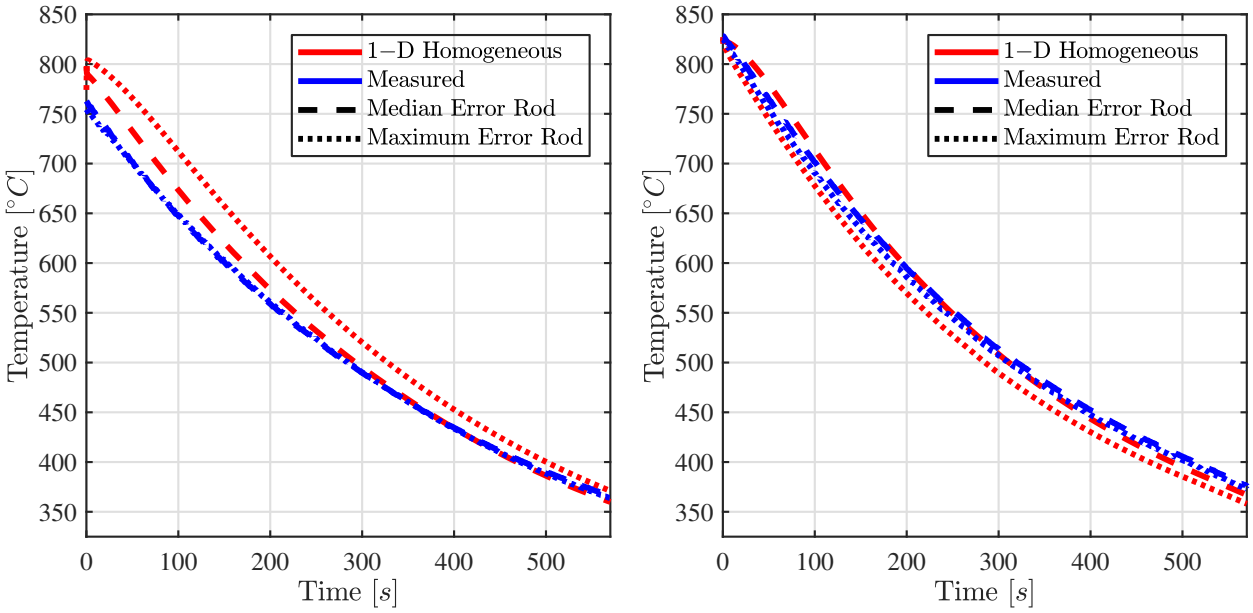

(a) *Thin shell* **(b)** *Thick shell*

Figure 4.6: *Comparison of measured vs. 1–D generated temperatures for selected rods.*

in the inital IR camera frame. Where as the initial conditions to the 1–D model could only be given as a function of radial location, the 2–D model could make use of initial conditions that vary in both radial and azimuthal location.

Adding azimuthally dependent initial conditions did reduce the profile grouping seen in the 1–D model. However, the error produced by the 2–D model (shown in Figure 4.9b) was significantly worse than that of the 1–D model. Thus it can be concluded that the inability to perfectly define the experiment's initial conditions was not a major source of error for the 1–D homogeneous model. Rather, the homogeneous model's inability to take into account other inter-rod heat transfer mechanisms, such as thermal radiation or varying contact resistance, is likely the primary cause of the 1–D model's inaccuracy.

4.5 Application of Machine Learning Model

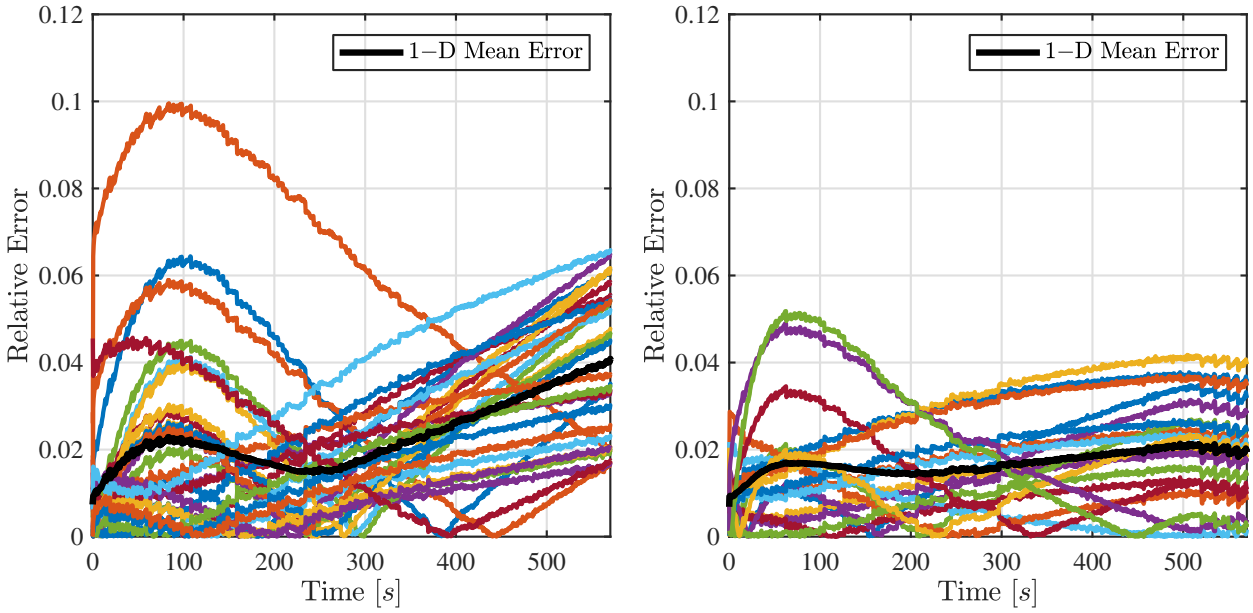

(a) *Thin shell* **(b)** *Thick shell*

Figure 4.7: *Relative error of 1–D temperatures for both thin and thick shell assemblies.*

4.5.1 Use of Machine Learning

There have been some recent attempts to adopt machine learning models to solve inverse heat transfer problems. However, their scope has been been limited to simple geometries with limited physical constraints [22, 23]. Additionally, these models are based on the conductive mode of heat transfer, so their application is generally limited to lower temperature regimes where radiative heat transfer can be neglected. In this paper, a novel machine learning approach is introduced to estimate the dynamic thermal responses in complex random arrangements of solids using support vector regression and algebraic graph theory. To illustrate this approach, assemblies of randomly packed, parallel cylinders with length-to-diameter ratios »1 were chosen to provide the test geometry. The rationale behind the choice of these assemblies was that the high length-to-diameter ratios of the cylindrical rods allow the system to be considered as a planar (2-D) network, with each cylindrical rod being considered as a node in the network. With this geometry, it is easy to make a simplified approach of categorizing lumped solids as either in or out of direct contact with their neighbors. The chosen assembly geometry was also selected to represent 2-D heat transfer through a network

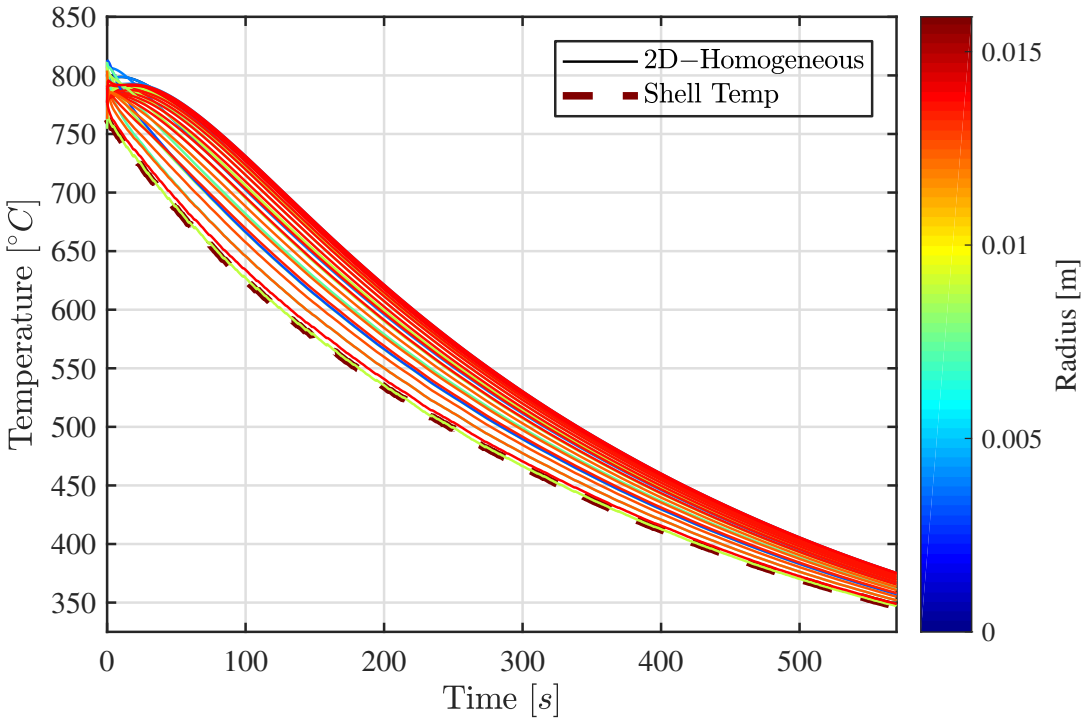

Figure 4.8: *2-D temperature profiles colored by radial location – Thin Shell Assembly*

of solids where the rate of heat transfer between the solids is almost entirely determined by their mutual minimal contact rather than by intra-solid conduction. The geometry of their mutual contacts in combination with data obtained at certain selected locations ('outer locations'), were used in this work to reconstruct a response of 'inner locations' using a support vector regression algorithm. In order to test this algorithm, the validation data for the 'inner locations', (which were not used in the regression), was also obtained. This paper first outlines the problem description and the procedure to obtain experimental data. This is followed by mathematical description of the prediction algorithm. Results of this study are analyzed in the next section. The final section discusses the conclusions from this work.

4.5.2 Problem Description

The experiments performed in this work involved the cooling of assemblies of cylindrical rods. The whole assembly is first brought to an almost uniform temperature via a radiative heater before being allowed to cool as heat is dissipated away from the outer surface of the quartz

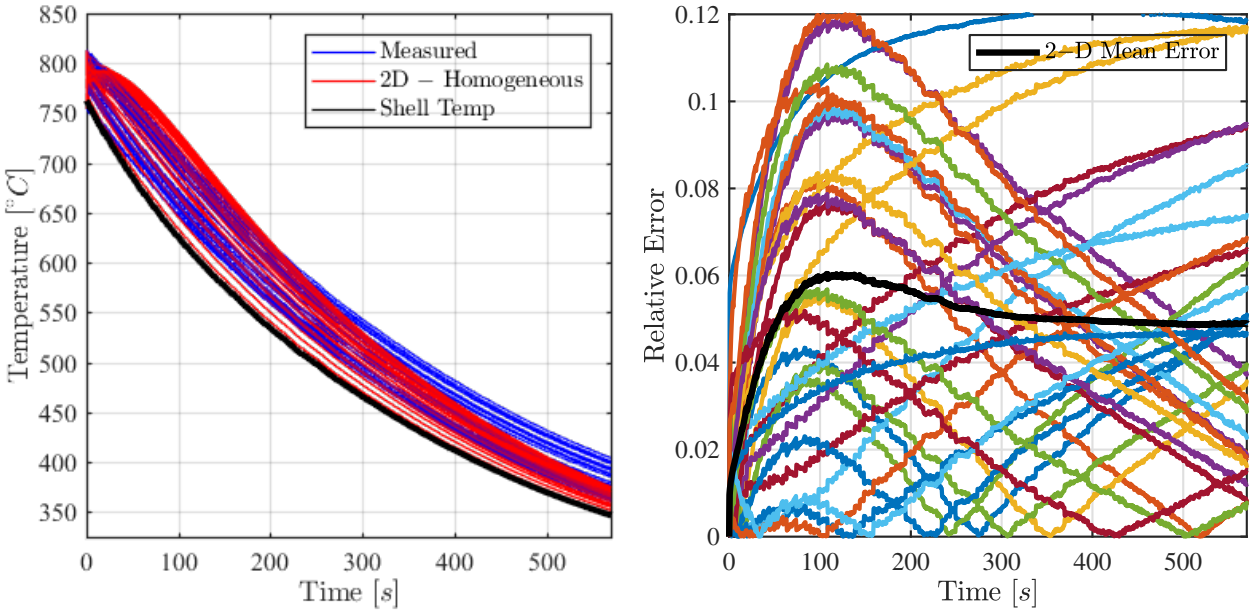

(a) *Measured vs. 2–D model temperatures* **(b)** *Relative error*

Figure 4.9: *2–D model results for the thin shell assembly.*

tube. Due to the high length-to-diameter ratio of each rod, the ends or the flat surfaces do not play any significant role in the governing physics, especially due to the non-convective environment inside the quartz tube. The aspect ratio of the rods justifies 2-D analysis. The first set of cases considered here consist of assemblies of 7, uniformly sized, cylindrical rods. Details of these assemblies can be seen in Table 4.1, in which the assemblies in question are labeled 3, 4, and 5. The rods were optimally packed within the quartz tube, with 6 outer rods held against 1 inner rod. This case represents a simplified scenario in which one solid is in contact with all other solids. A diagram depicting the assembly of 7 cylindrical rods can be seen in Figure 4.10.

The second studied case involved assemblies of a larger number of smaller cylindrical rods randomly packed inside the quartz tube. This assembly type is identified in Table 4.1 as number 6. In both cases the goal is to predict the temperature profile of the entire assembly when they are dynamically cooled from the outer surface using the prior information of geometry and dynamic temperature of outer rods. The black marks and faces on some of the rods in assemblies 4, 5, and 6 are locations where the constant emissivity paint was applied to the test rod.

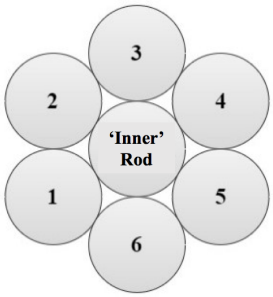

Figure 4.10: *Example of optimally packed assembly of large radii test pieces. 'Inner' rod in the figure is rod whose temperature is to be estimated and all other rods are referred to as 'Outer' rods in analysis presented later.*

Figure 4.11a & 4.11b show the IR images of the assemblies involved in each case. The outer rods have been marked in blue and other rods are shown in their initial maximum temperature. The dynamic cooling is initiated when all the rods are at the top/same temperature. The size (radius) and material of the rods were selected such that there would be no substantial gradients within each rod, so that the only significant thermal resistance is due to the network of gaps or contacts between the rods. In other words, each assembly can be represented as a graph with each rod corresponding to a node and edges appearing where there is direct physical contact between them. The Biot number (based on the natural convection and radiative cooling heat transfer, with diameter as the characteristic length) was always less than 0.1 for all the cases considered here. Although some intra-rod temperature variation can be seen in the IR images, these apparent intra-rod temperature gradients actually result from emissivity variations in the rod's non-uniform surface finish. Thus, the model developed and tested here treats the face average temperature of the rod as a instantaneous node temperature in the network.

It should be noted that although in many practical scenarios gravity and pressure may play some role in the overall thermal resistance of a network, in the current study the objective was not to resolve those issues but to construct a computational-experimental framework where limited temperature measurements can be used to predict temperature everywhere else in the assemblies. Due to the vacuum imposed on the test assemblies, such phenomenon do not affect the results of the experiments performed in this work.

The actual temperatures of the inner rods are used to validate the effectiveness of the proposed algorithm.

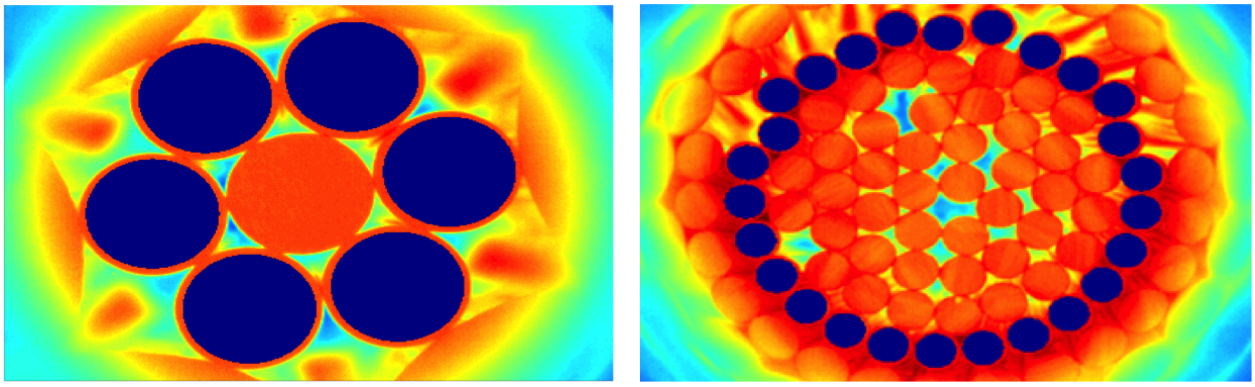

(a) *'Outer' rods (marked in 'blue' color) within 7 rod assembly are used for training input. 'Inner' rod temperature (not 'blue') is predicted in the algorithm described later*

(b) *'Outer' rods are marked with 'blue' color within the 68 rod assembly and are used as training set. Data from all 'Inner' rods (not in 'blue' color) are used for validation tests*

Figure 4.11: *Visualization of 'Outer' vs 'Inner' rods.*

4.5.3 Model description

4.5.3.1 Initialization

In machine learning regression, the data consists of a large set of samples, where each sample consists of an input and its corresponding output. These samples are divided into two disjoint sets, the *training set* and the *test set*. The training set is used to train the machine learning model, i.e. to optimize the model to perform the estimation task as accurately as possible. Once the model is obtained, the test samples, which were not used during the training process, are used to assess the performance of the model.

In this application, we will identify each sample with a 2-tuple of indexes, (i, t), where i is an index of a rod and t, a discrete time instance, that are divided into the training and test sets. Since the temperatures of the outer rods with indexes in a set, R_O, can be measured directly at at all time instants t, they can be used as training data. The temperatures of the inner rods whose indexes are in another set, R_I, which are available only up to a time interval $t = T_0$, can also be used.

Together, these samples make up the training set,

$$S_{train} = \{(i,t)|i \in R_O, 1 \leq t \leq T_\infty\} \cup \{(i,t)|i \in R_I, 1 \leq t \leq T_0\}. \tag{4.2}$$

The remaining samples constitute the test set,

$$S_{test} = \{(i,t)|i \in R_I, T_0 \leq t \leq T_\infty\}. \tag{4.3}$$

The models that are most frequently used in similar estimation tasks, such as neural networks or B-splines require features obtained using the physical coordinates of the rods and their temperatures $\theta_i(t)$ as direct inputs. Unfortunately these approaches are unfeasible. This is because the coordinates of the rods do not capture how the rods are connected to one another. Two rods that are physically near to one another may not be in direct contact with each other and the heat exchange between them may be relatively low. On the other hand, two rods that are further apart from one another may, in fact, be very tightly coupled thermally, through several intermediate rods that are in directly contact with both. Therefore, the connectivity between the rods is expected to play a major role in this contact heat transfer problem between randomly packed cylinders.

4.5.3.2 Kernel matrix

Each assembly of rods (see Section 2.) is depicted as a graph consisting of a set of nodes corresponding to the rods. An edge appears for every pair of rods in direct physical contact. This approach allows one to determine a diffusion kernel matrix $\mathbf{K}$, the *spatio-temporal kernel*. Each scalar entry, $K_{(i,t),(j,t')}$ of the spatio-temporal kernel reflects the degree of "similarity" between the pairs of samples (i,t) and (j,t') [24]. It is worthwhile to note that higher values of this entry arise when the rods indexed i and j are thermally tightly coupled and when the time interval separating the samples ($|t-t'|$), is small.

Since the matrix $\mathbf{K}$ captures both the degree of thermal coupling between the rods, as

well as how close two sample observations are in time, it is determined in this research as the Kronecker product of two separate matrices - a *spatial kernel* $\mathbf{K}^{\mathrm{s}}$, and a *temporal kernel* $\mathbf{K}^{\mathrm{t}}$, according to,

$$\mathbf{K} = \mathbf{K}^{\mathrm{s}} \otimes \mathbf{K}^{\mathrm{t}}. \tag{4.4}$$

The spatial kernel $\mathbf{K}^{\mathrm{s}}$ can be best understood by regarding the layout of the rod assembly as a weighted, undirected graph. Each node of the graph corresponds to a rod. For every pair of rods that are directly in contact with one another, there is a corresponding edge joining the corresponding nodes of the graph, with an associated weight of unity; otherwise there is no edge between them. An example of the connections between randomly packed set is shown in Figure 4.3.

Under these circumstances, the non-diagonal entries $L_{i,j}$, of the graph's Laplacian matrix $\mathbf{L}$ are given by [25, 26],

$$L_{i,j\neq i} = \begin{cases} -1, & \text{rods } i,j \text{ are in contact,} \\ 0, & \text{rods } i,j \text{ are not in contact;} \end{cases} \tag{4.5}$$

The diagonal entries of the Laplacian are the negatives of the row sums of the non-diagonal entries,

$$L_{i,i} = -\sum_{k\neq i} L_{i,k}. \tag{4.6}$$

In addition to the rods, the Laplacian is devised to take into account the contact that the outer rods have with the surrounding. In order to do so, the surrounding is considered as a *ghost node*, indexed 0. The temperature θ_0 of the surrounding *ghost node* with which the outer rods are in direct contact is treated as an additional parameter, and has its own index $i = 0$. Additional edges are introduced between the latter and the outer rods, albeit

with a smaller weight $l_0 < 1$. Hence,

$$L_{i,0} = L_{0,i} = \begin{cases} l_0, & i \in R_O \\ 0, & i \in R_I \end{cases} \tag{4.7}$$

This addition yields an additional row and column in the Laplacian $\mathbf{L}$ that are indexed 0, resulting in an $(N+1) \times (N+1)$ matrix. The weight l_0 above is an algorithmic constant. The combination of l_0 and θ_0 fix the representative external cooling rate for a particular case study.

The spatial kernel is obtained directly from the Laplacian as,

$$\mathbf{K}^{\mathrm{s}} = e^{-\sigma \mathbf{L}}. \tag{4.8}$$

The quantity $\sigma > 0$ is referred to as the *spatial constant*. The resulting spatial kernel $\mathbf{K}^{\mathrm{s}}$ obtained in this manner and whose scalar entries $K^s_{i,j}$ indicate the extent of thermal contact between the rods indexed as i and j, is a symmetric positive definite matrix [27].

The temporal kernel $\mathbf{K}^{\mathrm{t}}$ captures the degree of similarity based on the time difference $\Delta t = |t - t'|$ between two discrete time instances, t and t'. With $\tau > 0$ being a algorithmic constant called the *temporal constant*, each scalar entry $K^{\mathrm{t}}_{(t,t')}$ of the temporal kernel is obtained using the expression,

$$K^{\mathrm{t}}_{t,t'} = e^{-\frac{|t-t'|}{\tau}}. \tag{4.9}$$

The temporal kernel can readily be shown to be symmetric positive definite. It should be observed that the time differences $|t - t'|$ can lie within a very large interval $[1, \pm T]_\infty]$. Hence, in order to curtail the computational requirements, only differences $|t - t'| \leq 4$ have been used, resulting in a $(4N+1) \times (4N+1)$ dimension extended kernel matrix. Its row and column being indexed as (i, t) and (j, t'), with the entry in the $(i, t)^{\mathrm{th}}$ row and $(j, t')^{\mathrm{th}}$ column being $K_{(i,t),(j,t')}$.

As the Kronecker product of two positive definite matrices $\mathbf{K}^{\mathrm{s}}$ and $\mathbf{K}^{\mathrm{t}}$, the spatio-temporal kernel $\mathbf{K}$ is also a positive definite matrix. This matrix is used as inputs to

the regression model which also uses the observed temperatures, $\theta_i(t)$, $(i,t) \in S_{train}$ as reference output data during the training process and subsequently, also for estimating the temperatures of samples in S_{test}.

The specific machine learning model used is the *support vector regression* (SVR), a recent paradigm that relies on such Mercer kernels as inputs instead of actual features to perform temperature estimation [28, 29]. The application of the graph Laplacian in support vector machines (SVMs) have been proposed elsewhere [26, 30], although their use is mostly confined to classification problems rather than regression as reported in this paper.

4.5.3.3 Support vector regression

The spatio-temporal kernel $\mathbf{K}$ defines a reproducing kernel Hilbert space. Suppose $\mathbf{x}_{i,t}$ and $\mathbf{x}_{j,t'}$ are any two sample features, then their inner product in feature space is given by,

$$\langle \mathbf{x}_{i,t}, \mathbf{x}_{j,t'} \rangle = K_{(i,t),(j,t')}. \tag{4.10}$$

Given any sample $(i,t) \in S_{train}$, with $\theta_i(t)$ denoting the corresponding temperature, the objective of the SVM formulation is to obtain an estimation function $\hat{\theta}(\cdot)$ so that $\hat{\theta}(\mathbf{x}_{i,t}) = \hat{\theta}_i(t) \cong \theta_i(t)$.

The penalties incurred due to any error between $\theta_i(t)$ and $\hat{\theta}_i(t)$ which are denoted as ξ_i^- and ξ_i^+, and formulated in terms of an ϵ -insensitive loss function are [31],

$$\xi_{i,t}^- = \begin{cases} |\hat{\theta}(\mathbf{x}_{i,t}) - \theta_i(t)| - \epsilon, & \hat{\theta}(\mathbf{x}_{i,t}) \leq \theta_i(t) - \epsilon \\ 0, & \text{otherwise} \end{cases} \tag{4.11}$$

$$\xi_{i,t}^+ = \begin{cases} |\hat{\theta}(\mathbf{x}_{i,t}) - \theta_i(t)| - \epsilon, & \hat{\theta}(\mathbf{x}_{i,t}) \geq \theta_i(t) - \epsilon \\ 0, & \text{otherwise} \end{cases} \tag{4.12}$$

When the absolute difference between the estimated and actual temperatures is such that $|\hat{\theta}(\mathbf{x}_{i,t}) - \theta_i(t)| < \epsilon$, no penalty is incurred. In the feature space the SVM formulation allows

the function $\hat{\theta}(\mathbf{x}_{i,t})$ to be the following hyperplane,

$$\hat{\theta}(\mathbf{x}_{i,t}) = \langle \mathbf{w}, \mathbf{x}_{i,t} \rangle + b \tag{4.13}$$

The vector $\mathbf{w}$ and the scalar term b in the above equality are the directional vector and the bias of the hyperplane.

The correct SVM regression model for the task of temperature estimation is obtained through the training process that can be formulated as a constrained optimization problem [28]. Its objective function in primal form that needs to be minimized is given by,

$$C\sum_{i=1}^{N} \xi_{i,t}^{+} + C\sum_{i=1}^{N} \xi_{i,t}^{-} + \mathbf{w}^{\mathrm{T}}\mathbf{w} \tag{4.14}$$

Here C is a constant used in the formulation. Note the inclusion of the quadratic regularization term $\frac{1}{2}\mathbf{w}^{\mathrm{T}}\mathbf{w}$ [32].

Unlike usual machine learning models that would directly require as input argument the feature vector $\mathbf{x}_{i,t}$, the SVM performs this task using only inner products $\langle \mathbf{x}_{i,t}, \mathbf{x}_{j,t'} \rangle$, with each (j, t') being a sample in S_{train}, called a *support vector*. This is evident from the dual formulation of the SVM problem where the objective function can be shown to be given by the following expression,

$$-\frac{1}{2}\boldsymbol{\lambda}^{\mathrm{T}} \begin{bmatrix} +\mathbf{K} & -\mathbf{K} \\ -\mathbf{K} & +\mathbf{K} \end{bmatrix} \boldsymbol{\lambda} - \boldsymbol{\lambda}^{\mathrm{T}} \begin{bmatrix} +\epsilon\mathbf{1} - \boldsymbol{\theta} \\ +\epsilon\mathbf{1} + \boldsymbol{\theta} \end{bmatrix}. \tag{4.15}$$

In the above expression $\boldsymbol{\theta}$ is a vector of the observed temperatures of all samples in S_{train} and $\mathbf{K}$ is the spatio-temporal kernel. The quantity $\boldsymbol{\lambda}$ is a block vector containing the vectors $\boldsymbol{\lambda}^{+}$ and $\boldsymbol{\lambda}^{-}$ whose terms are the Lagrange multipliers of the training samples corresponding to the constraints,

$$\theta_i(t) - (\langle \mathbf{w}, \mathbf{x}_{i,t} \rangle + b) \leq \epsilon + \xi_{i,t}^{+}, \tag{4.16}$$

$$(\langle \mathbf{w}, \mathbf{x}_{i,t} \rangle + b) - \theta_i(t) \leq \epsilon + \xi_{i,t}^{-}. \tag{4.17}$$

These constraints are a direct outcome of the use of the ϵ-insensitive loss function. For samples (i,t) such that $|\hat{\theta}(\mathbf{x}_{i,t}) - \theta_i(t)| < \epsilon$, no penalty is incurred and $\xi^+_{(i,t)} = \xi^-_{(i,t)} = 0$. When the absolute differences between $\hat{\theta}(\mathbf{x}_{i,t})$ and $\theta_i(t)$ exceed this margin, two cases arise: for samples that lie above the hyperplane and at least at a distance ϵ away from it, the quantity $\xi^+_{(i,t)} \geq 0$. Likewise, for the points below it and again at a distance that is at least ϵ away, $\xi^-_{(i,t)} \geq 0$.

The Lagrange multipliers corresponding to these inequality constraints are $\lambda^+_{(i,t)}$ and $\lambda^-_{(i,t)}$, which form the vectors $\boldsymbol{\lambda}^+$ and $\boldsymbol{\lambda}^-$ respectively, so that,

$$\boldsymbol{\lambda} = \begin{bmatrix} \boldsymbol{\lambda}^+ \\ \boldsymbol{\lambda}^- \end{bmatrix}. \tag{4.18}$$

It can be shown that the constraints if the dual form are given by [28],

$$\boldsymbol{\lambda}^{\mathrm{T}} \begin{bmatrix} \mathbf{1}^+ \\ \mathbf{1}^- \end{bmatrix} = 0 \tag{4.19}$$

Solving the SVM in dual form yields the values of the Lagrange multiplier vectors $\boldsymbol{\lambda}^+$ and $\boldsymbol{\lambda}^-$. For any sample that lies outside the margin, a constraint is active; consequently $\lambda^+_{(i,t)} > 0$ or $\lambda^-_{(i,t)} > 0$. Together these samples (i,t) form the support vectors of the SVM.

In order to obtain the value of the hyperplane's bias b, we consider Lagrange multipliers that are strictly in the interval $(0, C)$, to obtain the two sets B^+ and B^- defined as,

$$B^+ = \{(i,t) \in S_{train} | 0 < \lambda^+_{(i,t)} < C\}, \tag{4.20}$$

$$B^- = \{(i,t) \in S_{train} | 0 < \lambda^-_{(i,t)} < C\}. \tag{4.21}$$

The bias b can be determined from any one support vector, although for numerical precision it is typically obtained as an average over all support vectors as shown below,

$$b = \frac{1}{|B^+| + |B^-|} \sum_{(i,t)\in B^+} \left(\theta_i(t) - \sum_{(j,t')\in S_{train}} (\lambda^+_{(j,t')} - \lambda^-_{(j,t')}) \langle \mathbf{x}_{i,t}, \mathbf{x}_{j,t'} \rangle - \epsilon \right) + \frac{1}{|B^+| + |B^+|} \sum_{(i,t)\in B^+} \left(\theta_i(t) - \sum_{(j,t')\in S_{train}} (\lambda^+_{(j,t')} - \lambda^-_{(j,t')}) \langle \mathbf{x}_{i,t}, \mathbf{x}_{j,t'} \rangle - \epsilon \right) \tag{4.22}$$

Using this value of the bias b, the estimated temperature of any test sample $(j, t') \in S_{test}$ can be obtained as,

$$\hat{\theta}(\mathbf{x}_{j,t'}) = \left(\sum_{(i,t)\in S_{train}} (\lambda^+_{(i,t)} - \lambda^-_{(i,t)}) \langle \mathbf{x}_{i,t}, \mathbf{x}_{j,t'} \rangle \right) + b. \tag{4.23}$$

The inner products in the above expression are the entries $K_{(i,t),(j,t')}$ of the spatio-temporal kernel.

4.5.4 Results

The algorithmic parameters defined in the model description $(l_0, \theta_0, \sigma, \tau, \epsilon, C)$ were tuned for each case to predict the dynamic temperature distribution $\hat{\theta}(\mathbf{x}_{i,t})$ in different experiments with different materials and sizes (diameters) of the rods. Values of these parameters and algebraic constants are listed in Table 4.3. The particular case of large-rod assemblies (with 7 rods) was repeated with three type of materials. The temperatures in the large-rod assemblies of different materials are obtained using the model described in the previous section and shown in Figure 4.12. The trajectories of the estimated temperatures, $\hat{\theta}(\mathbf{x}_{i,t})$, are plotted along with test data and training data for graphite, alumina, and large-quartz rods in Figures 4.12a, 4.12b, and 4.12c respectively. Data from different experiments show consistency in the cooling process as expected without any abnormal behavior. Qualitatively, the cooling profiles of individual rods agree with the typical cooling profiles of solid media without any internal convective effects. The case with assembly of large alumina rods (Fig.4.12b) shows a kink resulting from the transition in the training datasets used for predictive modeling at $t = T_0$. This transition time can be seen more clearly in the error plots (e.g. Fig. 4.12d),

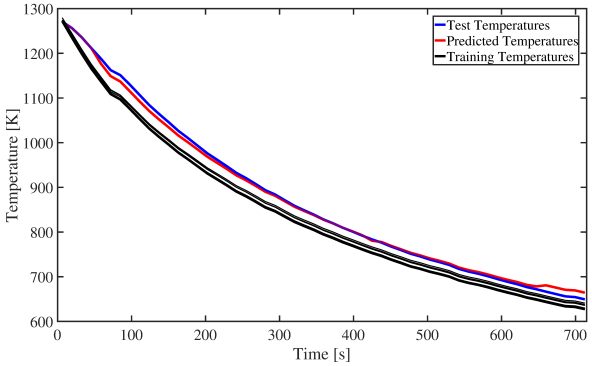

(a) *Model predicted temperature for 'inner' rod in assembly of large (15mm) graphite rods (T_0 = 45 sec).*

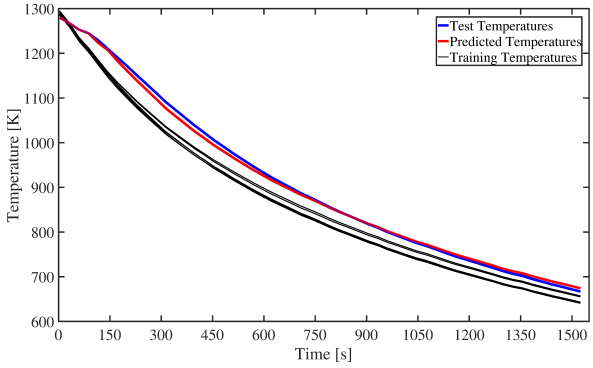

(b) *Model predicted temperature for 'inner' rod in assembly of large (15mm) alumina rods(T_0 = 87 sec).*

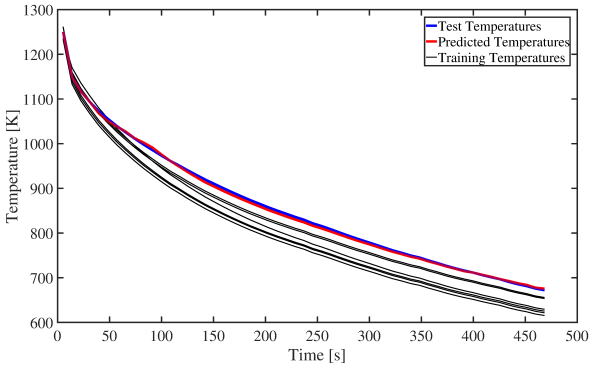

(c) *Model predicted temperature for 'inner' rod in assembly of large (15mm) quartz rods (T_0 = 31 sec).*

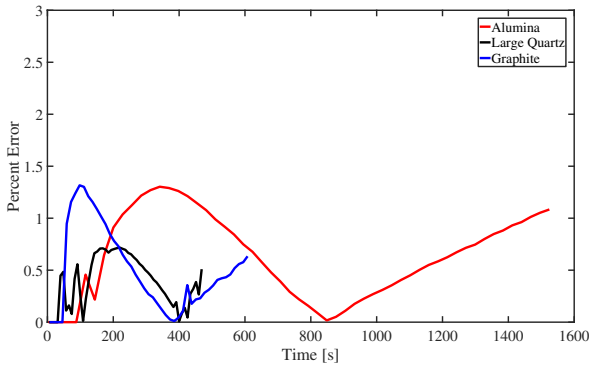

(d) *Percent error obtained by SVR model for each assembly.*

Figure 4.12: *Predicted 'inner' rod temperature results from large-rod assemblies packed in a regular close-fit configuration.*

where at times $t < T_0$ shows that error is equal to zero as during this time all rods are used for training the machine learning model.

Each case with different material rods was repeated at least three times and temperature results remained within $< \pm 0.1\%$. This is expected as in case with large-rods there is only 1 optimal way to pack the 7 rods. Normalized error values for each test case are computed from $||\frac{\hat{\theta}(\mathbf{x}_{i,t}) - \theta_i(t)}{\theta_i(t)}||$. In Figure 4.12d, the percent error resulting from the SVR generated temperature predictions is plotted for each of the three large-rod assemblies versus time. In all cases the normalized RMS error given by the model predictions remains below 1.5%. The values of algorithmic parameter set were unique for each case with different material types.

The results for the assembly of small (5mm) quartz rods are shown in Figure 4.13 and

Table 4.3: *Table of parameters used in SVR algorithm for each assembly.*

	l_0	θ_0	σ	τ	ϵ	C
Alumina	.15	700	5.1	.1	5.8	2000
Graphite	.15	400	5.1	2.1	5.8	2000
Large Quartz	.5	700	5.1	2.1	5.8	2000
Small Quartz	.15	700	15.1	.1	1.8	2000

4.14. The model predictions and experimental data, i.e. temperature vs time plots for small-rod assembly, are shown in Fig. 4.13. The maximum normalized error remains less than 3% throughout the domain of the experiments. Due to large number of trajectories present in Figure 4.13, more information is provided in Figure 4.14 which shows comparison between real and model estimated thermal images. It is evident from comparing the two images that model performs quite well in predicting the temperature of 'inner' rods. In case of small-rod assemblies, there are different possible packing configurations, such as both 64 rods and 68 rods can fit in quartz test tube. It should be noted that with the same set of values for algorithmic parameters, the model was able to predict temperatures in different configurations within accuracy level of 3%.

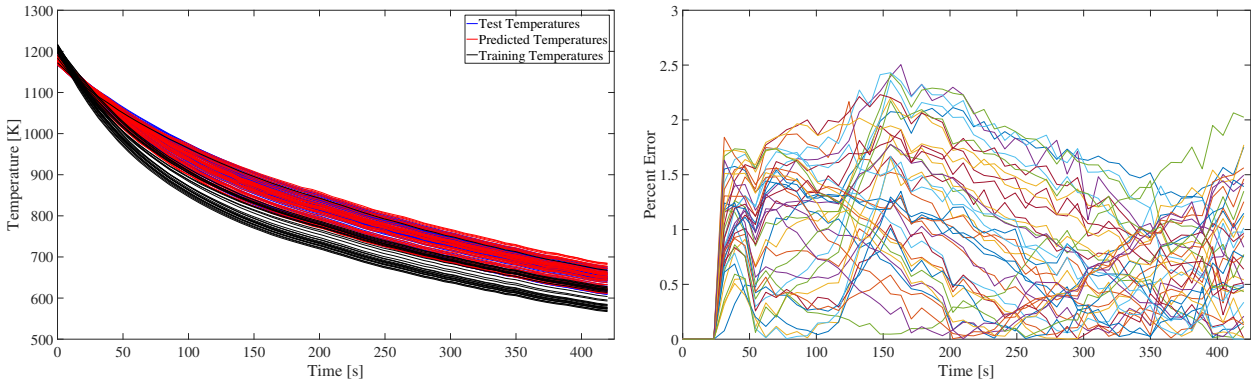

(a) *Predicted and measured (test) temperature results from assembly of 68 small (5mm) quartz rods.*

(b) *Normalized RMS error based on the predicted and measured (test) values.*

Figure 4.13: *Predicted temperature results and RMS estimates from assembly of 68 small (5mm) quartz rods .*

The algorithm is able to estimate temperature trajectories versus time without any information on the actual thermo-physical properties such as thermal conductivity, heat capacity, density, surface roughness, emissivity of the test materials or the convection coefficient

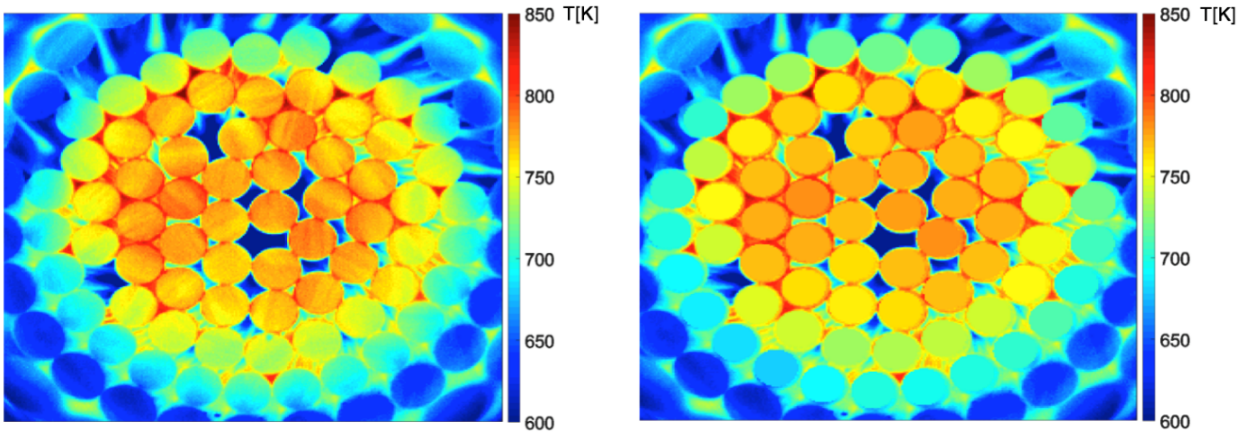

(a) *IR image of small rod assembly while cooling.* **(b)** *IR image of small assembly while cooling with overlaid model predictions.*

Figure 4.14: *IR images with and without model prediction overlay (at* $t = 200$ *sec).*

around the outer quartz tube. Only 6 algorithmic parameters were tuned for the different cases based on the different materials and test geometries. These parameters were kept constant in most of the cases, apart from the few exceptions that can be seen in the tabulated values. These values of the parameters used for the regression, listed in Table 4.3, can be qualitatively explained with the relative physical behavior of the different materials or size conditions. For example, the 'outer' Graphite rods are expected to cool at a faster rate than the alumina due to their high emissivity and heat transfer with the external tube, and the algorithmic constant (θ_0) is lower for the graphite rods. In other words, for any significant different cooling behavior combination of algorithmic constants (l_0, θ_0) need to be tuned in the current formulation of this model. Similarly σ, the *spatial parameter*, which is used to construct the spatial Kernel functions, for small quartz rods was lower than the values for all other cases which use rods of larger diameter. Therefore, this model can be improved in future by providing physics based parameterization.

4.6 Application of Finite Element Model

4.6.1 Discrete Element Method Simulation

For both the homogeneous and support vector regression models described, respectively, in Sections 4.2 and 4.5, all required geometric information on each specified rod assembly was able to be obtained from image data generated by the IR camera. Although the low resolution of the IR camera does not allow for the precise measurement of each rod's location, this limitation was not previously an issue. In fact, a major advantage of each of the two aforementioned models was that their accuracy was not highly dependent on such information. For the case of the support vector regression model, the spatial coordinates of each rod were technically not even needed; the model was based solely on which rods were defined to be in contact with one another. And although rod position data was technically required by the homogeneous models, that which could calculated from IR camera images proved wholly sufficient. Given that the final predictions of the 2–D model – in which it was possible to fully define each rod's location – were less accurate than those provided by the 1–D model, for which rod position could only be defined radially, the precision of the geometry data used is not a limiting factor.

However, finite element models require very precise geometric information to accurately simulate the effects of point contacts on inter particle heat transfer. In contrast to the machine learning method, it is not possible – independent of the measured rod location – to simply define rods to be in contact with one another. Rather, the geometry of the assembly must be defined with a sufficient level of precision for a mesh to be created in which nodes from adjoining rods can be properly connected. Geometry defined using only the image analysis method outlined in Section 4.3.3 was found to be insufficiently accurate for proper mesh connections to be made between adjoining rods. Although it is possible that using higher-resolution, visible light images would allow for the image analysis procedure to produce a sufficiently accurate and precise assembly geometry, the problem was instead solved by using an N-body algorithm to improve the accuracy of the geometry data given

from the analysis of the IR images. This approach not only allowed for a 2–D finite element model of the rod assembly to be created, but also provided an opportunity to validate a method an algorithm that could then be used to create other, more complicated geometries.

Therefore, a 2–D Discrete Element Method (DEM) simulation was used to modify the rough rod geometry information provided by the IR camera. The approximate rod centroid locations found from the IR image analysis were used as initial conditions for the simulation. Due to the initial rod centroid locations not being precisely accurate, some rods will initially overlap. These overlapping regions result in forces – and thus accelerations – being applied to the offending particles. This process is repeated over a large number of time steps, during which each particles acceleration and velocity are tracked and integrated to provide new position data each time step. The newest position data is then again analyzed for overlaps, following which new forces are applied. This process repeats until particles are deemed to be moving sufficiently slowly.

Because centroid locations given by the IR camera are used as initial conditions for this process, few overlaps initially exist and the system is quickly able to converge to a low energy, low velocity state. At this point, its absolute rod positioning will be almost identical to those of the actually assembly and the relative rod locations will be sufficiently accurate to use in a finite elements simulation.

4.6.2 COMSOL Model

A commercial multi-physics software, COMSOL, was used to create a finite element model (FEM) of the experimental assemblies. Due to the very high aspect ratios of the objects within assemblies, a 2-D model was used. Geometry information, i.e. the location of each rod's centroid in relation to the outer graphite shell, was obtained from the N-body algorithm as discussed in Section 4.6.1. This process resulted in the geometry shown in Figure 4.15. The contact locations of adjoining – as opposed to merely nearby – objects in the geometry can be visibly identified in Figure 4.15 from the high density regions of the overlain mesh. The inner boundary of the outer shell is highlighted in blue. Matching the conditions of the

experimental setup, the empty areas surrounding the rods within the shell was modeled in COMSOL as a vacuum. Thus no material is seen in between the rods in Figure 4.15.

Following the methodology used in the homogeneous models, the heat capacity of the solid domains was defined as a function of temperature while a constant value was used for the bulk thermal conductivity of the material.

The boundary conditions used in the model were surface-to-surface radiation, thermal contact resistance, and prescribed temperature. The outer and inner shell boundaries were given time dependent, prescribed temperature boundary conditions. Specifically, the temperatures of these boundaries were set to be equal to the median temperature of the shell face.

Any portion of a rod or shell boundary that was in contact with a portion of the shell or another rod was subjected to thermal contact resistance boundary condition. This boundary condition modified the heat flux passing through the boundary by incorporating a resistance term at the boundary. A parametric sweep of resistance values was used to find a near-optimal value of thermal contact resistance for Assembly 1. This value, $8 \times 10^{-5}\,\mathrm{K\,W^{-1}\,m^{-2}}$, was then also used for the COMSOL model of Assembly 2 as well.

Finally, all interior boundaries not in physical contact with another boundary were set to be gray, diffuse surfaces with emissivity values of 0.86.

The COMSOL model was a 570 second transient simulation. The model start time, t_0, was defined as the moment when, following the removal of the surrounding tube furnace, the median shell temperature fell below the lowest measured rod face temperature.

Initial temperatures of the shell and rod faces were obtained from the IR camera measurements at the time t_0 and input into the COMSOL model as a spatial interpolation function. As the simulation marches through time from t_0, the thermal energy initially stored within the rods is diffused and radiated outwards towards the to the shell, which, due to its lower, prescribed temperature, acts as a sink.

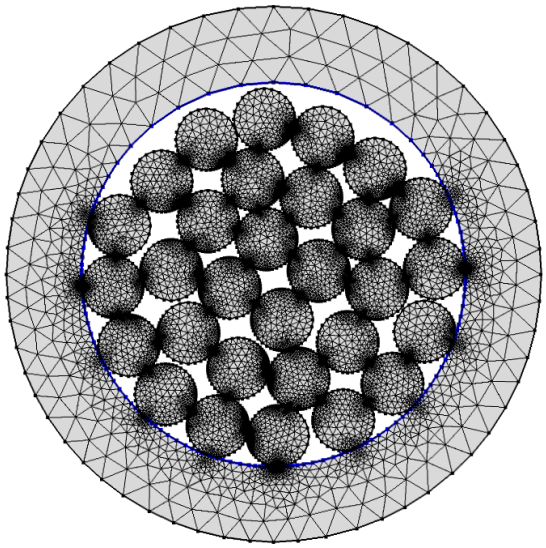

Figure 4.15: *Geometry and mesh of thin-shell FEM model.*

4.6.3 Finite Element Results

A comparison between the the measured rod temperatures for Assemblies 1 and 2 and the temperatures given by the COMSOL finite element model is plotted in Figures 4.16a and 4.16b, respectively. It is immediately apparent that the finite element model eliminates the banding effect (see Section 4.4.2.1) that reduced the accuracy of the 1–D homogeneous model. Disappointingly, the maximum error given by the finite element model is noticeably worse than that given by the 1–D homogeneous model for either Assembly 1 or 2. This difference can be seen by comparing Figures 4.17 and 4.6 or 4.18 and 4.7.

However, it should be remembered that while the homogeneous models of Section 4.4 – and, for that matter, the machine learning model presented in Section 4.5 as well – were fully refined and maximally optimized for the specific data set to which they were applied, this is not even remotely true of the FEM model. Not only are there several parameters (e.g. emissivity, sphere overlap, and contact resistance) that could be further optimized to allow the FEM model to produce more accurate results for the Assembly 1 and 2 data sets, the model is also far more easily extendable to other data sets and geometries.

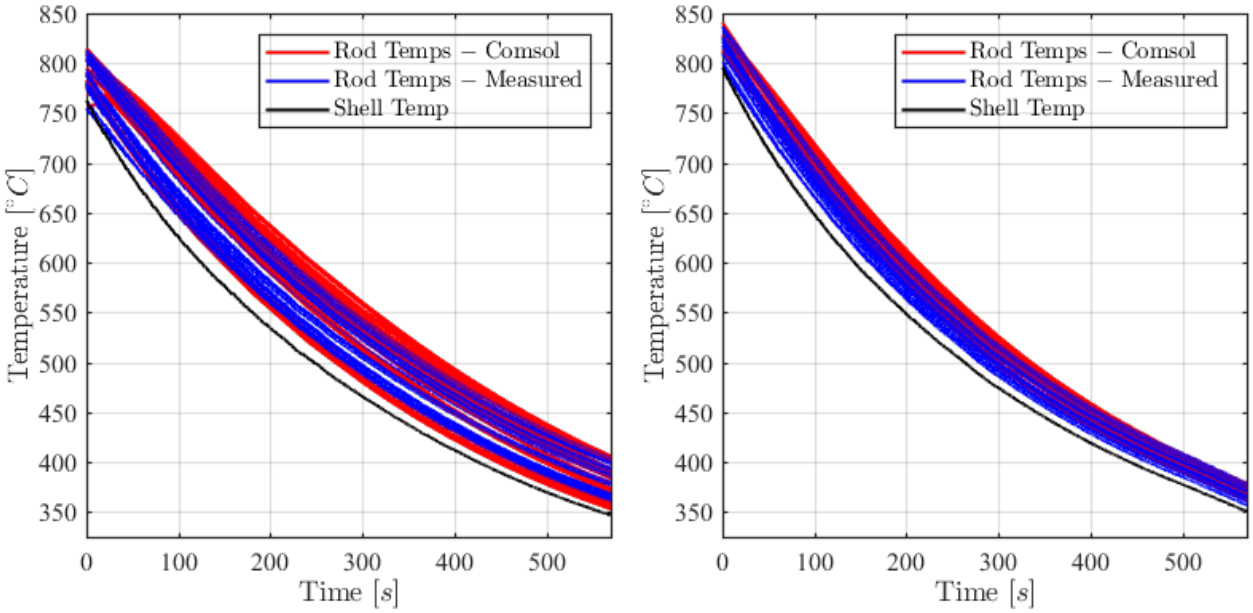

(a) *Thin shell* **(b)** *Thick shell*

Figure 4.16: *Comparison of measured vs. FEM generated temperatures.*

4.7 Conclusions

The homogeneous models are simple, but even with the ideal geometry, initial conditions, boundary conditions, and effective material properties, they often simply do not represent small-scale, randomly packed geometries well. This is especially true of 1–D models due to the banding effect introduced by multiple objects possessing approximately similar spatial coordinates.

The machine learning based approach presented in 4.5 represents an effective combination of graph theoretic kernels and support vector regression to estimate these temperatures. Using temperature information of all rods for few initial time steps and subsequently that of a limited set of rods i.e. 'outer' rods, the temperature trajectories of inner rods were predicted for much larger duration. The results from this model clearly demonstrate the effectiveness of the machine learning approach. This approach differs from previous work as it does not take into account thermo-physical properties or phenomenological models. Instead, a limited set of algorithmic parameters are used. The cases studied were simple enough due to low Biot number and large aspect ratios to justify their representation as planar graphs.

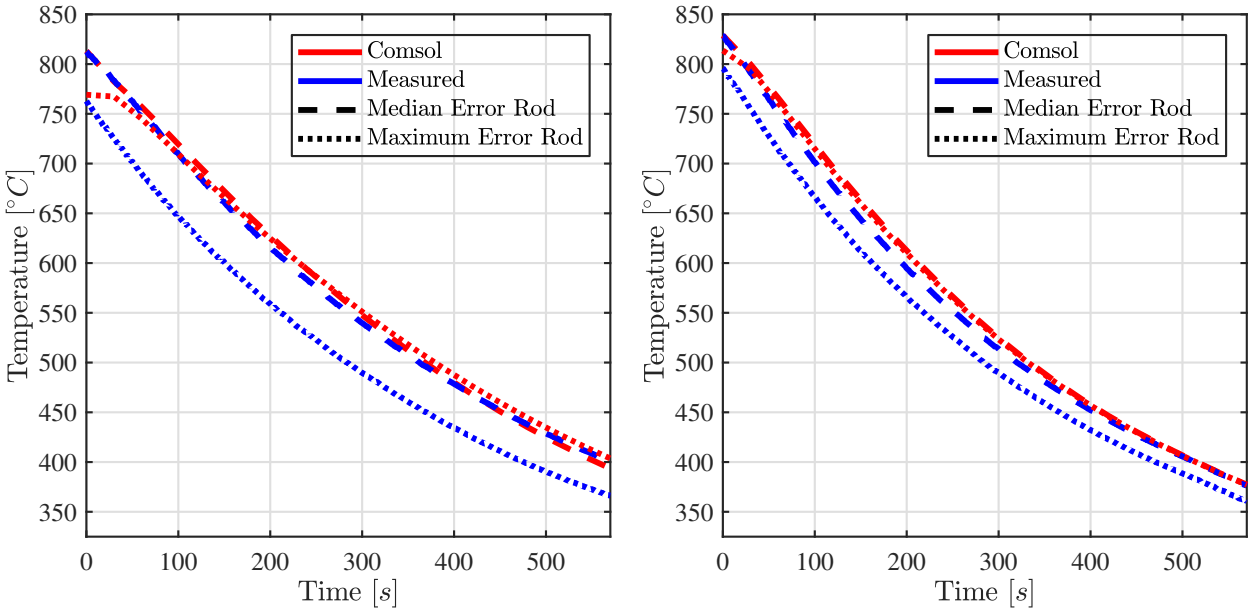

(a) *Thin shell* **(b)** *Thick shell*

Figure 4.17: *Comparison of measured vs. FEM generated temperatures for selected rods.*

Future research may address more generic situations of solid assemblies containing arbitrary geometries and demonstrating pronounced temperature gradients within solids.

Finally, the finite elements simulation was able to eliminate the banding effect of the homogeneous models. The mean relative error of the COMSOL results was also found to be equivalent or better than the homogeneous models. Most importantly however, the finite elements model – unlike the optimized homogeneous model – has the potential for significant refinement and extension.

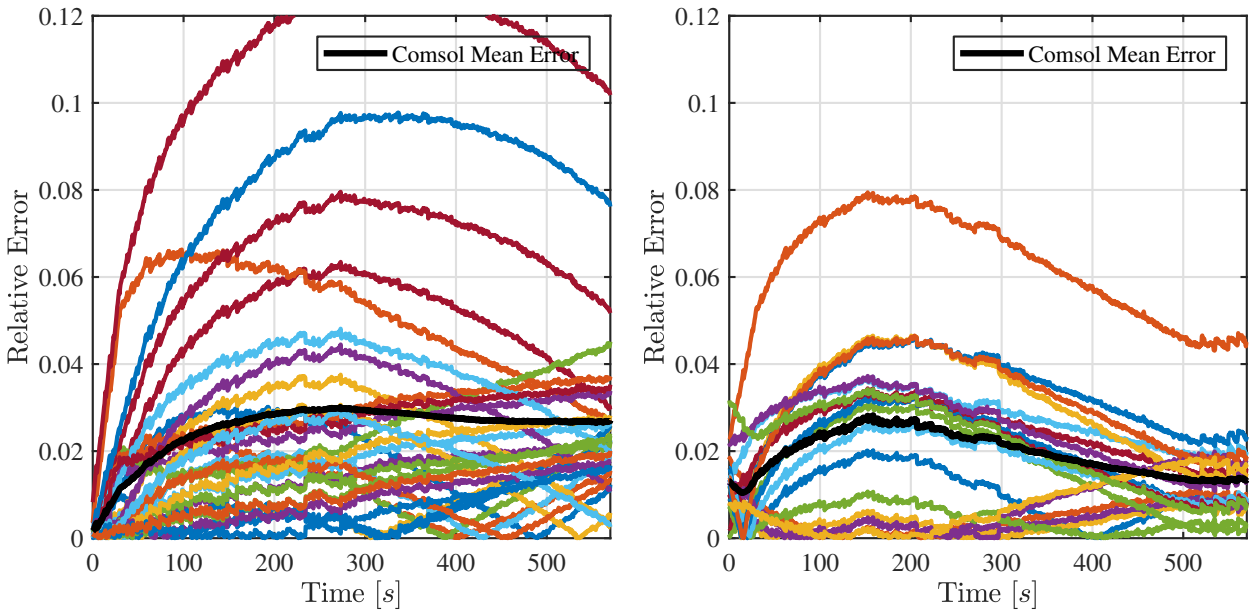

(a) *Thin shell* **(b)** *Thick shell*

Figure 4.18: *Relative error of FEM temperatures for both thin and thick shell assemblies.*

Bibliography

[1] M N Vu, S T Nguyen, M H Vu, Anh Minh Tang, and V T To. Heat conduction and thermal conductivity of 3D cracked media. *International Journal of Heat and Mass Transfer*, 89:1119–1126, 2015.

[2] M G Cooper, B B Mikic, and M M Yovanovich. Thermal contact conductance. *Int. J. Heat Mass Transf.*, 12(3):279–300, 1969. ISSN: 0017-9310. DOI: 10.1016/0017-9310(69)90011-8. URL: http://www.sciencedirect.com/science/article/pii/0017931069900118.

[3] B B Mikić. Thermal contact conductance; theoretical considerations. *International Journal of Heat and Mass Transfer*, 17(2):205–214, 1974.

[4] C.V. Madhusudana. *Thermal Contact Conductance*. Springer, 1996. ISBN: 978-1-4612-3978-9.

[5] M Michael Yovanovich. Four decades of research on thermal contact, gap, and joint resistance in microelectronics. *IEEE transactions on components and packaging technologies*, 28(2):182–206, 2005.

[6] M. Bahrami, M. M. Yovanovich, and J. R. Culham. Thermal joint resistances of conforming rough surfaces with gas filled caps. *Journal of thermophysics and heat transfer*, 18(3):318–325, 2004. DOI: 10.2514/1.5480.

[7] Jean-Jacques Salgon, F Robbe-Valloire, J Blouet, and Jacques Bransier. A mechanical and geometrical approach to thermal contact resistance. *International journal of heat and mass transfer*, 40(5):1121–1129, 1997.

[8] Vishal Singhal, Paul J Litke, Anthony F Black, and Suresh V Garimella. An experimentally validated thermo-mechanical model for the prediction of thermal contact conductance. *International Journal of Heat and Mass Transfer*, 48(25-26):5446–5459, 2005.

[9] Ruiping Xu, Haidong Feng, Lanping Zhao, and Lie Xu. Experimental investigation of thermal contact conductance at low temperature based on fractal description. *International communications in heat and mass transfer*, 33(7):811–818, 2006.

[10] Navni N Verma and Sandip Mazumder. Extraction of thermal contact conductance of metal-metal contacts from scale-resolved direct numerical simulation. *International Journal of Heat and Mass Transfer*, 94:164–173, 2016.

[11] E M Burghold, Y Frekers, and R Kneer. Determination of time-dependent thermal contact conductance through IR-thermography. *International Journal of Thermal Sciences*, 98:148–155, 2015.

[12] C Fieberg and R Kneer. Determination of thermal contact resistance from transient temperature measurements. *International Journal of Heat and Mass Transfer*, 51(5-6):1017–1023, 2008.

[13] Ling Shi and Huiling Wang. Investigation on thermal contact resistance by photothermal technique at low temperature. *Heat and mass transfer*, 43(11):1179–1184, 2007.

[14] W. Van Antwerpen, C. G. Du Toit, and P. G. Rousseau. A review of correlations to model the packing structure and effective thermal conductivity in packed beds of mono-sized spherical particles. *Nuclear Engineering and Design*, 240(7):1803–1818, 2010. ISSN: 00295493. DOI: 10.1016/j.nucengdes.2010.03.009.

[15] Daniel W Gould, Hitesh Bindra, and Sanjoy Das. Thermal response construction in randomly packed solids with graph theoretic Support Vector Regression, 2017.

[16] Oleg M Alifanov. *Inverse heat transfer problems*. Springer Science & Business Media, 2012. ISBN: 3642764363.

[17] Christophe Le Niliot and Paulin Gallet. Infrared thermography applied to the resolution of inverse heat conduction problems: recovery of heat line sources and boundary conditions. *Revue générale de Thermique*, 37(8):629–643, 1998.

[18] A M El-Sabbagh, C Fieberg, E El-Magd, and R Kneer. Modeling of transient thermal contact resistance out of conjugate gradient method. *Materialwissenschaft und Werkstofftechnik*, 38(4):288–293, 2007.

[19] Jung-Hun Noh, Won-Geun Kim, Ki-Up Cha, and Se-Jin Yook. Inverse heat transfer analysis of multi-layered tube using thermal resistance network and Kalman filter. *International Journal of Heat and Mass Transfer*, 89:1016–1023, 2015.

[20] Marcelo J Colaço and Carlos J S Alves. A fast non-intrusive method for estimating spatial thermal contact conductance by means of the reciprocity functional approach and the method of fundamental solutions. *International Journal of Heat and Mass Transfer*, 60:653–663, 2013.

[21] Thomas F. Coleman and Yuying Li. On the convergence of interior-reflective newton methods for nonlinear minimization subject to bounds. *Mathematical programming*, 67(1-3):189–224, 1994. ISSN: 0025-5610.

[22] Obed Cortés, Gustavo Urquiza, J A Hernandez, and Marco A Cruz. Artificial neural networks for inverse heat transfer problems. In *Electronics, Robotics and Automotive Mechanics Conference, 2007. CERMA 2007*, pages 198–201. IEEE, 2007. ISBN: 0769529747.

[23] K Goudarzi, A Moosaei, and M Gharaati. Applying artificial neural networks (ANN) to the estimation of thermal contact conductance in the exhaust valve of internal combustion engine. *Applied Thermal Engineering*, 87:688–697, 2015.

[24] V David Sánchez A. Advanced support vector machines and kernel methods. *Neurocomputing*, 55(1-2):5–20, 2003.

[25] Franois Fouss, Kevin Francoisse, Luh Yen, Alain Pirotte, and Marco Saerens. An experimental investigation of kernels on graphs for collaborative recommendation and semisupervised classification. *Neural networks*, 31:53–72, 2012.

[26] Amarnag Subramanya and Partha Pratim Talukdar. Graph-based semi-supervised learning. *Synthesis Lectures on Artificial Intelligence and Machine Learning*, 8(4):1–125, 2014.

[27] Risi Imre Kondor and John Lafferty. Diffusion kernels on graphs and other discrete input spaces. In *ICML*, volume 2, pages 315–322, 2002.

[28] Debasish Basak, Srimanta Pal, and Dipak Chandra Patranabis. Support vector regression. *Neural Information Processing-Letters and Reviews*, 11(10):203–224, 2007.

[29] Richard G Brereton and Gavin R Lloyd. Support vector machines for classification and regression. *Analyst*, 135(2):230–267, 2010.

[30] Deng Cai, Xiaofei He, and Jiawei Han. Semi-supervised regression using spectral techniques. Technical report UIUCDCS-R-2006-2749, University of Illinois at Urbana-Champaign, 2006.

[31] Yuh-Jye Lee, Wen-Feng Hsieh, and Chien-Ming Huang. Ssvr: a smooth support vector machine for insensitive regression. *IEEE Transactions on knowledge and data engineering*, 17(5):678–685, 2005.

[32] Alexander J Smola and Risi Kondor. Kernels and regularization on graphs. In *Learning theory and kernel machines*, pages 144–158. Springer, 2003.

Chapter 5

Application of Experimental Results to Pebble Bed Reactor

5.1 Introduction

In Chapter 4, due to experimental constraints, cylindrical geometry was used to look at the effects of point contacts on the heat transfer within an HTGR. However, in many HTGR designs the nuclear fuel is arranged in a packed bed of spheres rather than cylinders. Thus, rather than the line contacts that were modeled in Chapter 4, point contacts will exist between the fuel elements in such a reactor. In this chapter a 3–D CFD simulation is performed in which the effects of oxidation and point to point contacts could be applied to a simulated packed bed geometry. The results from the 3–D CFD simulation are then compared those generated by an ideal 1–D homogeneous model.

5.2 3–D Model

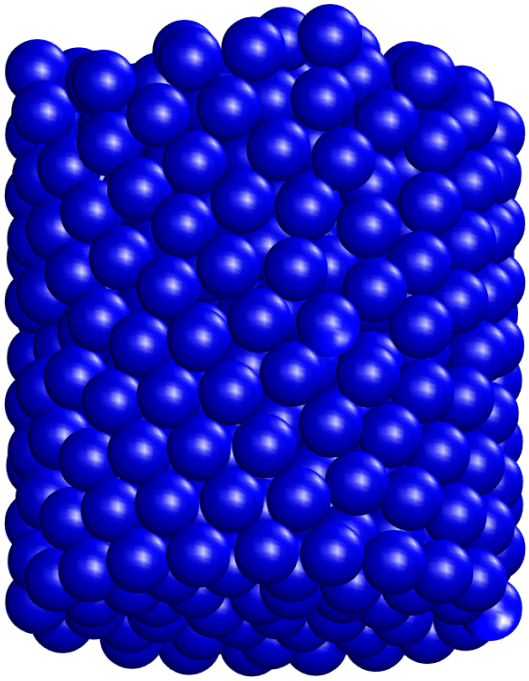

Figure 5.1: *Packed bed of 500, 60 mm diameter spheres.*

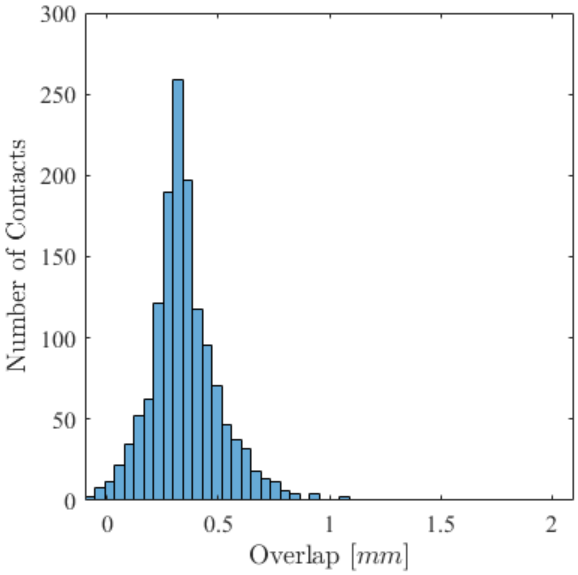

Figure 5.2: *Histogram depicting particle overlap distances.*

5.2.1 3-D Discrete Elements Method

The discrete elements method is widely used for generating packed bed geometries [1, 2] and was used here to create the geometry for the 3–D numerical heat transfer simulation. Although the method cannot easily produce periodic geometries and is not as precise as some overlap removal methods [3], it is far more computationally efficient and thus can be used to create far larger beds. To create the packed bed geometry that would be used by the 3–D FEM package, a discrete elements method code was written in Matlab[1] to determine 500 fuel-pebble centroid locations that would form a stable packing structure within a 240 mm radius cylinder.

Although based on the code used in Section 4.6.1, thanks to several improvements, such as the use of exponential inter-particle potentials and variable time steps, the final code was highly successful at accurately positioning a much larger number of objects in a higher dimensional space. An example of its effectiveness is shown in Figure 5.2. Here, the overlap distance – i.e., the arithmetic difference between the displacement of two particle centroids and the particle's diameter – between all particles in close proximity is plotted with a histogram. The target overlap distance was 0.35 mm. The mean actual overlap distance achieved with

[1]The DEM code used in this work was originally based on an algorithm written by Dr. Mark Shattuck.

the simulation was 0.3976 mm and the standard deviation of the distribution was 0.229 mm . The finalized geometry produced by the DEM code is shown in Figure 5.1.

5.2.2 Bed Porosity

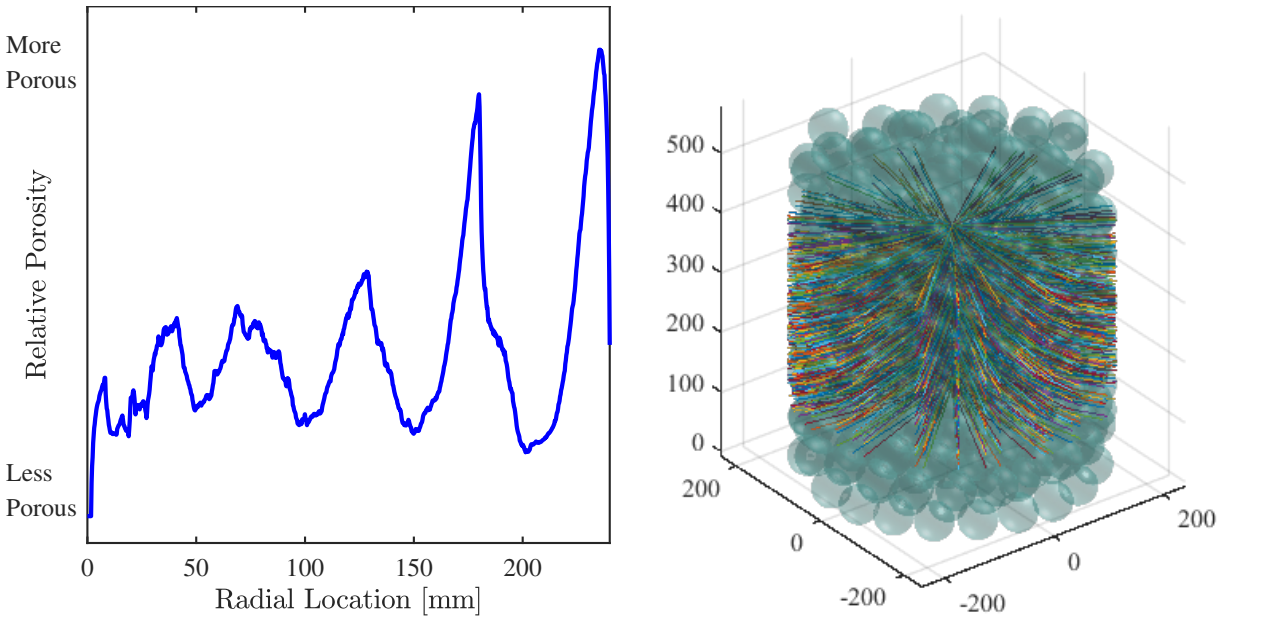

(a) *Relative porosity of 500 sphere geometry; calculated using 500 thousand rays.*

(b) *Graphical depictions of example rays for relative porosity calculation.*

Figure 5.3: *Relative porosity of packed bed*

Overall, the DEM generated packed bed possessed an average porosity of 39%, matching the values achieved by both Pavlidis and Lathouwers [4] using the overlap removal method and Du Toit [5] using a DEM method. This average value was obtained from calculations performed over the middle 80% of the bed's length, where the effects of the top and bottom of the packed bed were minimal.

The relative porosity function plotted in Figure 5.3a was computed using a Monte Carlo method. A large number of rays running radially outward from the center of the packed bed were created. Examples of such test rays can be seen in Figure 5.3b. Numerous locations along each ray were tested to find out whether or not they were located within the domain of a solid particle. The tallys for each ray are then recorded as a function of the radial location of the test points. The continued oscillations in Figure 5.3a even as the bed center

Sphere Radius	25 mm
Shell Thickness	5 mm
Number of Particles	500
Bed Radius	240 mm
Bed Height	582 mm
Mean Contact Area	28.2 mm^2

Table 5.1: *Geometric parameters of individual particles and packed bed.*

is approached confirm that the entire packed bed can be considered in the "near-wall" region. Because of this, many previously developed empirical correlations for packed beds are not valid for this particular geometry.

5.2.3 Geometry and Boundary Conditions

Each spherical particle was modeled as a 25 mm radius sphere surrounded by a 5 mm thick shell. These dimensions match those of the fuel particles produced by NUKEM for the Thorium High-Temperature Reactor. The splitting of the fuel pebbles into the two separate domains was required as only the inner 25 mm regions (the 'Spheres' domains) of the NUKEM fuel pebbles contained fissile material; the outer 5 mm layer of each pebble (the 'Spherical Shells' domains) was made of graphite alone.

These shapes were created in the Solidworks CAD program and placed in an assembly at the centroid locations previously determined by the DEM model. This geometry was then exported into the Ansys Design Modeler program for final processing. Using the Design Modeler software, two additional domains (in addition to the 'Spherical Shells' and 'Spheres' domains imported from the CAD software) were created using Boolean operations. Additionally, the overlapping areas within the 'Spherical Shells' domain were sliced as to implement the "capped" method described by Ferng and Lin [6].

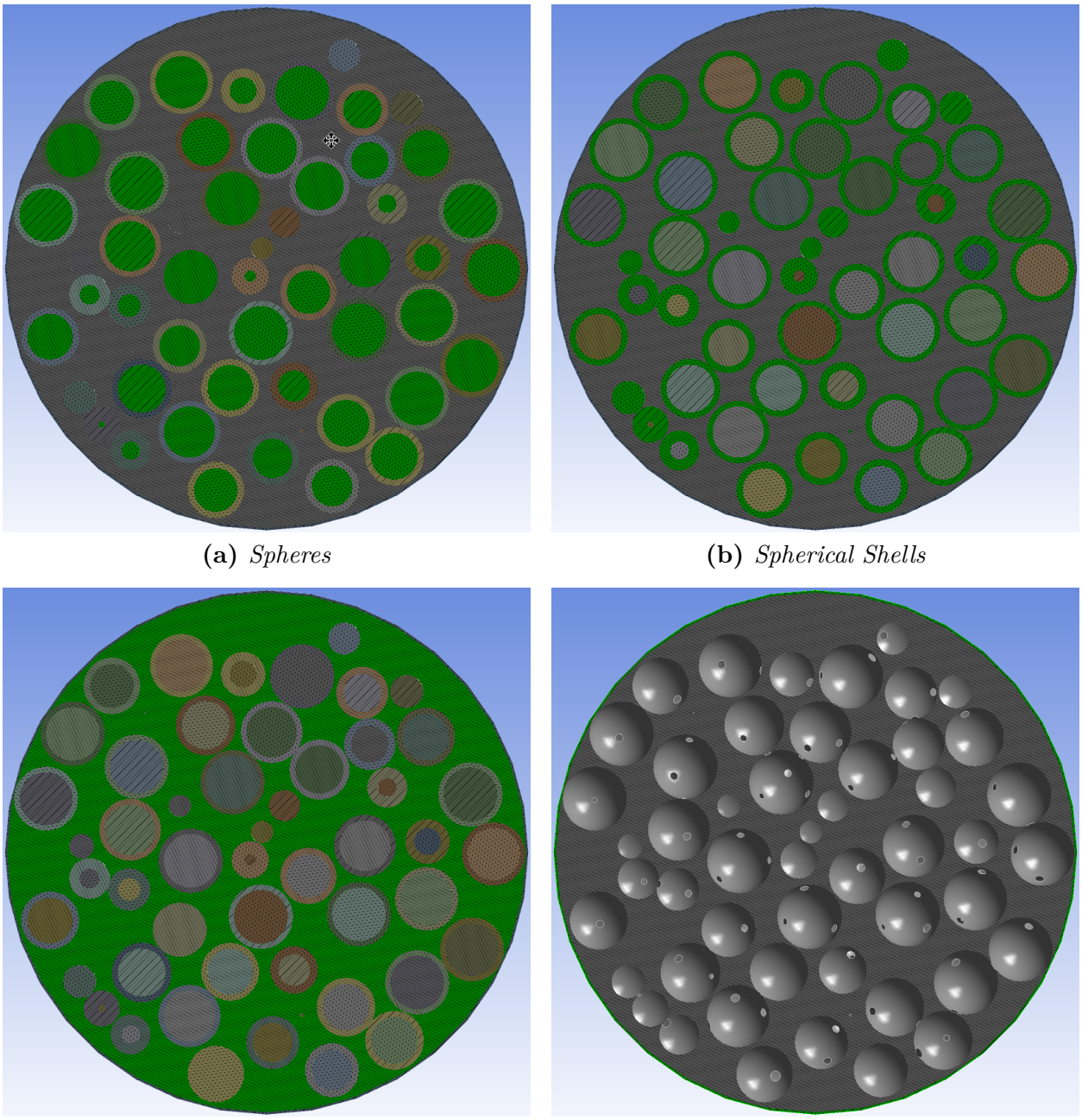

(a) *Spheres*

(b) *Spherical Shells*

(c) *Solid Air*

(d) *Cylindrical Shell*

Figure 5.4: *Cross section of meshed geometry with individual domains identified in green.*

The 'Solid Air' domain was created in the area between the particles within the packed bed and was defined to be a solid domain with the material properties of air. As buoyancy forces, fluid flow, and radiative heat transfer are not considered by this model, modeling this region as a solid material was acceptable.

Surrounding the air, sphere, and shell domains is the 'Cylindrical Shell' domain. This

	Spheres	Sphere Shells	Air	Cylindrical Shell
$\boldsymbol{\rho_{un-oxidized}}$	$1850\,\mathrm{kg\,m^{-3}}$	$1850\,\mathrm{kg\,m^{-3}}$	Ideal Gas	$1850\,\mathrm{kg\,m^{-3}}$
$\boldsymbol{\rho_{oxidized}}$	$1850\,\mathrm{kg\,m^{-3}}$	$1100\,\mathrm{kg\,m^{-3}}$	Ideal Gas	$1850\,\mathrm{kg\,m^{-3}}$
$\boldsymbol{k}$	$75\,\mathrm{W\,m^{-1}\,K^{-1}}$	$75\,\mathrm{W\,m^{-1}\,K^{-1}}$	$0.07\,\mathrm{W\,m^{-1}\,K^{-1}}$	$75\,\mathrm{W\,m^{-1}\,K^{-1}}$
$\boldsymbol{C}$	$1775\,\mathrm{J\,kg^{-1}\,K^{-1}}$	$1775\,\mathrm{J\,kg^{-1}\,K^{-1}}$	$1004\,\mathrm{J\,kg^{-1}\,K^{-1}}$	$1775\,\mathrm{J\,kg^{-1}\,K^{-1}}$

Table 5.2: *Material properties used in 3–D model.*

domain is a 2.5 mm thick cylindrical shell. A cross section of this shell is shown highlighted in green in Figure 5.4d. The top and bottom faces of the cylindrical shell – i.e. the domain's exterior faces that are parallel to the cross section shown in Figure 5.4d – were defined as insulated surfaces while a constant temperature boundary condition of 300 K was applied to the outermost wall of the cylindrical shell.

Perfect thermal contact was assumed to exist between the Spherical Shell domains and the Sphere domains, as well as between the Solid Air domain and the Cylindrical Shell domains. The thermal contacts between individual shells were not assumed to be perfect. This is discussed further in Section 5.2.4. The bottom and top faces of both the Solid Air and Cylindrical Shell domains were defined to be insulated surfaces.

To represent the decay heat generated within each particle following an air-ingress accident, a time-dependent generation function was applied to each of the 'Spheres' domains. The time-dependent decay heat generation rate reported by Teuchert et. al for pebble bed reactors as a function of steady state power was used [7]. For the NUKEM pebbles, the average total generation rate for each pebble under steady state conditions was specified to be 1.4 kW under steady state operation [8].

5.2.4 Oxidation Effects

To simulate some of the potential effects of oxidation discussed in Chapter 3, several simulations were performed using identical geometries, but different material properties and contact resistances. The laser flash analysis of Section 3.2.4.2 showed that the thermal diffusivity of each of the oxidized samples was significantly greater than that of the un-oxidized, control sample. From this analysis, a density of $1100\,\mathrm{kg\,m^{-3}}$ was calculated for the average density

	$\mathbf{R_a}$ [m]	$\mathbf{\Delta}_a$	$\mathbf{R_s}$ [K/W]	$\mathbf{R_L}$ [K/W]
Control	0.0156×10^{-4}	0.0940	0.0127	17.9
Saw Cut	0.1089×10^{-4}	0.2632	0.0316	10.9
Oxidized 1	0.4755×10^{-4}	1.024	0.0355	7.32
Oxidized 2	0.2584×10^{-4}	0.6875	0.0287	8.40

Table 5.3: *Roughness parameters for each of the samples tested.*

	(1)	**(2)**	**(3)**
	Unoxidized, Perfect Contact [5.6a]	**Unoxidized, Contact Resistance** [5.6b]	**Oxidized and Irradiated** [5.6c]
$\boldsymbol{k_{eff}}\left[\frac{\mathrm{W}}{\mathrm{m\,K}}\right]$	6.6665	2.5469	2.1744
Residual Norm	1.58E5	8.00E4	1.44E5
Time Step [s]	100	100	100

Table 5.4: *1–D homogeneous model data*

of the porous layer on the oxidized G-348 test pieces. For this model, it was assumed that the oxidation process would result in a 5 mm thick porous layer on each of the spheres. Thus for the models simulating the packed bed after oxidation, the density 'Sphere Shells' domain was changed to the $1100\,\mathrm{kg\,m^{-3}}$ value extrapolated from the laser flash data. Average values of thermal conductivity and heat capacity were used for each domain.

The roughness measurements presented in Section 3.2.4.3 were used in conjunction with portions of the Multi-sphere Unit Cell model presented by Antwerpen et. al [2] to calculate the macro-contact and micro-contact resistances present between individual particles. Calculated values of micro (R_s) and macro (R_L) roughness are shown in Table 5.3 next to their respective measured roughness parameters. These resistances were applied to the interface boundaries between individual fuel pebbles by assuming a $28.2\,\mathrm{mm^2}$ mean contact area for all inter-pebble contacts. Given the low standard deviation of pebble overlap provided by the employed DEM simulation (see Figure 5.2) using an averaged contact area for all contact resistances is acceptable.

5.3 1–D Model

A 1–D radial model was created to provide a comparison with the results from the 3–D packed bed model. As was previously done in Section 4.4.1, the system was modeled as a homogeneous domain with modified material properties. The density and heat capacity of the representative domain were defined to be porosity-weighted average of that used for the solid particles in the 3–D simulation.

Regarding thermal conductivity, an optimization method was once again used to find an optimal value of k_{eff} for the packed bed. Refer to Section 4.4.1 for details on the optimization algorithm used. For this model, the optimization process performed with the goal of minimizing the error between both the maximum and mean sphere temperature reported by the 1–D and 3–D models. Results obtained from the 1–D model using the optimized k_{eff} are also compared to those given by the value of k_{eff} provided by Teuchert, Haas, and Van Heek [7] for a pebble bed reactor core.

In contrast to Section 4.4, no higher dimensional homogeneous models were created. This decision was made for two reasons. First, Figure 5.5 shows a large amount of axial symmetry in the temperature distribution given by the 3–D model. Secondly, a homogeneous, 2–D axisymmetric model with insulated boundary conditions placed on the boundaries perpendicular to its line of symmetry is, for equal initial conditions, identical to a 1–D radial model. As the initial conditions applied to the 3–D model were spatially constant, no benefit would thus be gained by modeling the system with a higher-dimensional, homogeneous model.

5.4 Results

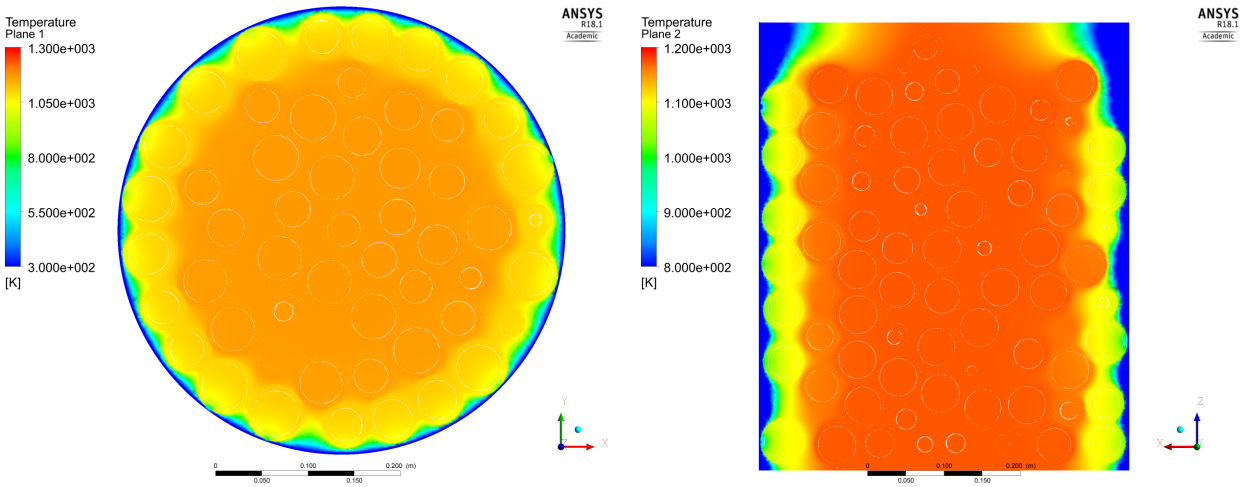

(a) *Cross section of bed 0.3 m above bed base.* **(b)** *Axial slice through mid-plane of packed bed.*

Figure 5.5: *Temperature of unoxidized packed bed with no contact resistance at 100 s.*

Data sets from three different simulations were analyzed: unoxidized graphite spheres in perfect thermal contact with one another (Case 1), unoxidized graphite spheres with contract resistance (Case 2), and oxidized and irradiated graphite spheres with contact resistance (Case 3). Case 1 is used as a limiting case example in which the graphite still possesses it's full density and thermal conductivity and in which any thermal contact resistance between individual spheres is negligible. In case 2, the graphite spheres were assumed to have an unoxidized, smooth surface. Using the roughness values measured for the control graphite sample in Table 5.3, the effects of thermal contact resistance were calculated and added to the model. Finally, in case 3 the effects of oxidation and irradiation were included in the analysis. With irradiation, the thermal conductivity of the NUKEM particles themselves has previously been shown to greatly decrease [8]. As any fuel particles that would be involved in an air ingress accident are almost certain to have undergone significant irradiation, for case 3, in addition to modeling the effects of thermal contact resistance between individual oxidized fuel spheres, the bulk thermal conductivity value of the spheres and shells domains was lowered to the 30 $\frac{\mathrm{W}}{\mathrm{m\,K}}$ value reported by Harms and Trauger.

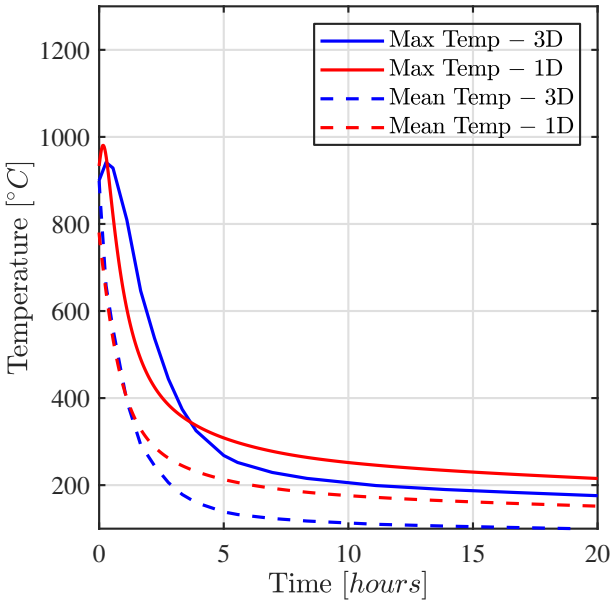

(a) *Unoxidized graphite in perfect thermal contact.*

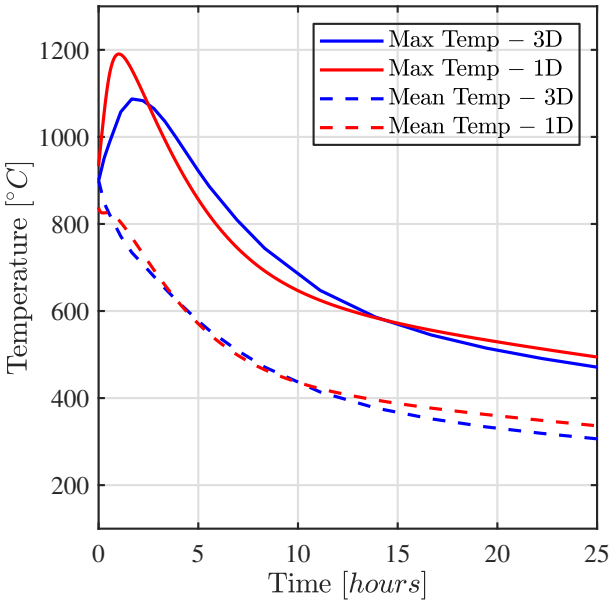

(b) *Unoxidized graphite with contact resistance.*

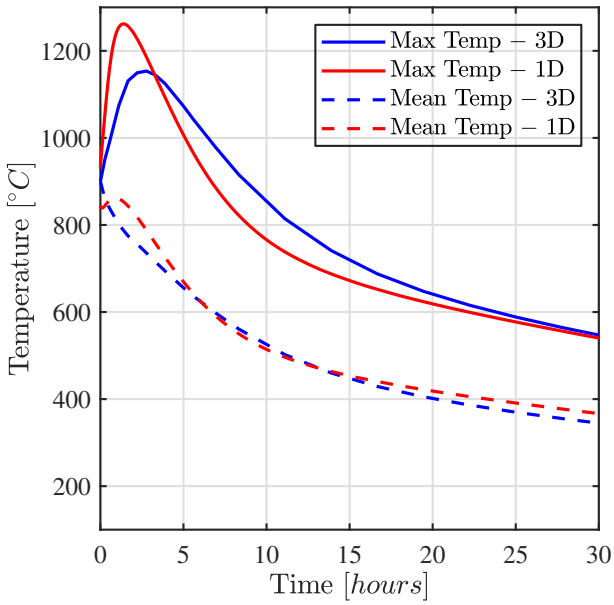

(c) *Irradiated and oxidized graphite with contact resistance.*

Figure 5.6: *Plots of bed maximum and med mean temperatures over time as determined by both 3–D CFD and the 1–D homogeneous code with an optimal* k_{eff}.

In Figure 5.5, pseudo-color temperature plots of two different planes are shown from the Case 1 CFD model, 100 seconds into the run. Table 5.4 presents the results of the effective thermal conductivity optimization algorithm are shown for each case. In each

case, the optimal value of thermal conductivity to best match the 3–D CFD results was significantly lower than that previously suggested by Teuchert, Haas, and Van Heek [7] for an entire pebble bed reactor core. This difference is likely a result of the packed bed geometry simulated in the 3–D CFD model not being large enough for wall effects to become negligible. Although the contact resistance used in case 3 was less than that used in case 2 (due to the effects of increasing roughness on the Multi-Sphere Unit Cell model), the lower bulk thermal conductivity value used in case 3 resulted in lower overall radial heat transfer.

Figure 5.6 plots mean and maximum bed temperatures for each of the three analyzed cases as calculated by both the 3–D CFD and 1–D homogeneous models. The 1–D code over predicted the bed maximum temperature by 39 K, 97 K, and 108 K for cases 1, 2, and 3, respectively. It should be remembered that the 1–D results shown in Figure 5.6 represents the accuracy of the best possible 1–D, homogeneous model. In the real world, the accuracy of any such model is likely to be far worse.

5.5 Conclusions

Previous reported values for effective thermal conductivity of a PBR core should not be taken as gospel in the near-wall region. Additionally, given the temperature under predictions seen even using the optimal k_{eff} values, any 1–D homogeneous model claiming to accurately represent the near-wall region of a PBR bed should be viewed skeptically if precise temperature values are needed in this region. At the very least, any attempt to produce such a model should take into account the irradiation and oxidation history of the graphite fuel particles involved as both effects are seen to greatly impact both the overall heat transfer rate of the bed and a 1–D homogeneous model's ability to predict said rate.

Acknowledgments

The author would like to thank Mark Shattuck for providing the initial code upon which the DEM code used here was built.

Bibliography

[1] W. Van Antwerpen, C. G. Du Toit, and P. G. Rousseau. A review of correlations to model the packing structure and effective thermal conductivity in packed beds of mono-sized spherical particles. *Nuclear Engineering and Design*, 240(7):1803–1818, 2010. ISSN: 00295493. DOI: 10.1016/j.nucengdes.2010.03.009.

[2] W. Van Antwerpen, P. G. Rousseau, and C. G. Du Toit. Multi-sphere Unit Cell model to calculate the effective thermal conductivity in packed pebble beds of mono-sized spheres. *Nuclear Engineering and Design*, 247:183–201, 2012. ISSN: 00295493. DOI: 10.1016/j.nucengdes.2012.03.012.

[3] Alexander Z. Zinchenko. Algorithm for random close packing of spheres with periodic boundary conditions. *Journal of Computational Physics*, 114(2):298–307, 1994. ISSN: 10902716. DOI: 10.1006/jcph.1994.1168.

[4] D. Pavlidis and D. Lathouwers. Realistic packed bed generation using small numbers of spheres. *Nuclear Engineering and Design*, 263:172–178, 2013. ISSN: 00295493. DOI: 10.1016/j.nucengdes.2013.04.024.

[5] Charl G. Du Toit. Radial variation in porosity in annular packed beds. *Nuclear engineering and design*, 238(11):3073–3079, 2008. ISSN: 0029-5493.

[6] Y. M. Ferng and K. Y. Lin. CFD investigation of thermal-hydraulic characteristics in a PBR core using different contact treatments between pebbles. *Annals of Nuclear Energy*, 72:156–165, 2014. ISSN: 18732100. DOI: 10.1016/j.anucene.2014.05.021.

[7] E. Teuchert, K. A. Haas, A. Van Heek, and P. R. Kasten. Distribution of the decay heat in various modul htrs and influence on peak fuel temperatures. In *Decay heat*

removal and heat transfer under normal and accident conditions in gas cooled reactors, number IAEA-TECDOC-757, page 53, 1992.

[8] W. O. Harms and D. B. Trauger. Fabrication variables, performance and cost considerations for htgr coated-particle fuels. In Fuel Cycles of High Temperature Gas-Cooled Reactors. (May 5, 2017), pages 27–49, 1965.

Chapter 6

Conclusions and Future Work

Many of the concepts and experimental techniques discussed in this work can improve safety analysis performed on HTGR designs. The new 'h'-shaped experimental apparatus allowed for the effects of the stagnate mass of helium present within the upper plenum of the modular HTGR designs on ONC to be examined. ONC measurements taken using the thermal imaging method proved highly reliable and consistent. Computational studies modeling the experimental conditions in the 'h'-shaped apparatus were also able to match the experimentally measured ONC times.

The effect of a potential hole in the upper head of a GT-MHR style HTGR should be further studied. In future work, further effort will be made to precisely scale the effects seen in this experimental apparatus to that which would be seen in an actual GT-MHR. Additionally, the effectiveness of proposed methods of delaying ONC, such as the injection of helium into a reactor after an air ingress accident has already occurred, should be examined.

Graph theory a promising approach for modeling individual systems with known geometries. Further work could also be done in this area by using the graph theory technique to analyze assemblies made up of multiple materials, as opposed to the single-material assemblies created in this work.

Additionally, repeating the cooling experiments with oxidized graphite rods could help better understand the effects of oxidation on such packed assemblies beyond what simple computational models are able to provide. Rather than using models within models to apply the effects of surface roughness and density changes, simply performing similar cooling experiments with previously oxidized graphite rods would provide a direct measurement of any differences in the material's heat transfer abilities.

Thermal conductivity changes due to oxidation are likely minor – especially compared to the large drop in thermal conductivity the graphite will experience due to irradiation. In contrast, changes in the density of oxidized graphite are likely to be much larger – especially in regions that are within a few millimeters of an exposed surface.

Regarding the oxidation experiments, several potential avenues of further study exist. First, repeating the axial flow oxidation experiments at different temperatures and flow rates could both help refine the correlation between flow rate over the sample and the rise in

thermal diffusivity later measured, as well as provide information on how the other oxidation regimes might affect graphite's thermal properties. Second, as any graphite in a reactor during an air ingress has likely already been subjected to large amounts of radiation, repeating the oxidation experiments done in this work using previously irradiated graphite test pieces is suggested. Other methods of inhibiting oxidation, such as adding nitrogen to the graphite structure, might also be tried.

The effects of oxidation greatly hinders the accuracy of 1–D homogeneous models in the near wall region. When pre-oxidized properties were used, an ideal homogeneous 1-D model was shown to be capable of predicting the max and mean temperatures of the packed bed to within 40 celsius. However, when oxidation and irradiation were assumed to have occurred, even an ideal homogeneous model using the optimal effective thermal conductivity over predicted the maximum bed temperature by more than 100 celsius. Thus, following an air ingress accident, such models should not be considered reliable within the near wall region of the packed bed. In future work, testing larger packed beds would allow for similar analysis to be performed on the bulk region of the packed bed where the particles are unaffected by the presence of the container wall.